



More information available at:
www.iba.muni.cz/summer-school2014
www.matematickabiologie.cz



Institute of Biostatistics and Analyses
Masaryk University

Proceedings of the 10th Summer School on Computational Biology

Image Data Analysis and Processing in Neuroscience

9-12 September 2014
Ochoz u Brna,
Czech Republic

Proceedings of the 10th Summer
School on Computational Biology

Publication was supported by the ESF project no. CZ.1.07/2.2.00/28.0043
"Interdisciplinary development of Computational Biology study programme"
and national budget of the Czech Republic.

**muni
PRESS**

ISBN 978-80-210-7011-0



OCHOZ U BRNA 2014

Editors:
Eva Janoušová
Daniel Schwarz



euROPEAN
social fund in the
czech republic



MS
MT
MINISTRY OF EDUCATION,
YOUTH AND SPORTS



INVESTMENTS IN EDUCATION DEVELOPMENT

**Institute of Biostatistics and Analyses
Masaryk University**

Proceedings of the 10th Summer School on Computational Biology

Image Data Analysis and Processing in Neuroscience

**9–12 September 2014
Ochoz u Brna, Czech Republic**

**Editors:
Eva Janoušová
Daniel Schwarz**



europa
esf
european
social fund in the
czech republic



EUROPEAN UNION



MINISTRY OF EDUCATION,
YOUTH AND SPORTS



OP Education
for Competitiveness



INVESTMENTS IN EDUCATION DEVELOPMENT

© 2014 Masarykova univerzita
ISBN 978-80-210-7011-0

Contents

Preface Daniel Schwarz, Eva Janoušová	5
LECTURES	7
Significance of the image analysis in contemporary psychiatry Tomáš Kašpárek	9
Image registration and its role in computational neuroanatomy Daniel Schwarz	13
Dynamic contrast-enhanced MRI and ultrasound using blind deconvolution Radovan Jiřík, Karel Souček, Martin Mézl, Michal Bartoš, Eva Dražanová, František Dráfi, Lucie Grossová, Jiří Kratochvíla, Ondřej Macíček, Kim Nylund, Aleš Hampl, Odd Helge Gilja, Torfinn Taxt, Zenon Starčuk jr.	41
Introduction to diffusion-weighted imaging René C.W. Mandl	48
Computing average cortical profiles at 3 tesla René C.W. Mandl, Martijn P. van den Heuvel, Rachel M. Brouwer, Hilleke E. Hulshoff Pol	53
Operative neurosurgical techniques, multimodality image fusion and its application in a neuroscience programme Ivo Ríha	57
Reduction and classification methods for image data analysis Eva Janoušová	66

Machine learning algorithms Jan Kybic	81
Déjà-vu phenomenon from the perspective of computational neuroanatomy Milan Brázdil, Radek Mareček	82
Imaging genetics – a way of studying the link between genes and brain structure and function Giovanni Montana	89
STUDENTS' ABSTRACTS	91
Multiresolution analysis of brain images for schizophrenia recognition Petr Dluhoš, Daniel Schwarz, Tomáš Kašpárek	93
Study of spinal cord in multiple sclerosis by MRI Marek Dostál, Miloš Keřkovský	96
Pattern recognition methods for image data analysis Tereza Dufková, Eva Janoušová, Tomáš Kašpárek	99
Mask_explorer – tool for group fMRI data validation and its application on study of Levodopa effect in patients with Parkinson's disease Martin Gajdoš, Michal Mikl, Radek Mareček	102
SigHunt: The new way of thinking about horizontal gene transfer Kamil S. Jaroň, Jiří C. Moravec, Natália Matínková	105

Welcome word

Dear students and colleagues,

we are pleased to welcome you to the 10th year of the Summer School on Computational Biology, which is expected to encourage the collaboration among professors, young scientists, and students of computational biology and related study programmes.

Institute of Biostatistics and Analyses at Masaryk University (IBA MU) initiated the yearly tradition of summer schools focused on various aspects of computational science in biology and biomedicine in 2005 and since then the participants have been educated and trained in various fields and topics:

2005	Computational Biology
2006	Predictive Modelling and ICT in Environmental Epidemiology
2007	Processing and Analysis of Biodiversity Data: from Genomic Diversity to Ecosystem Structure
2008	Statistical Methods for Genetic and Molecular Data
2009	Analysis of Clinical and Biomedical Data in an Interdisciplinary Approach
2010	Deterministic and Stochastic Modelling in Biology and Medicine
2011	Biodiversity: from genetics to geography, from mathematics to management
2012	From analysis of genomic data to clinical applications – case studies
2013	Stochastic Modelling in Epidemiology
2014	Image Data Analysis and Processing in Neuroscience

The Summer School on Computational Biology celebrates its 10th anniversary this year and its title is ***Image Data Analysis and Processing in Neuroscience***. Besides the standard teaching sessions, the summer school programme also includes several computer practice sessions and motivating lectures. The Summer School 2014 has an extraordinary panel of nine lecturers. Besides the teachers from IBA MU, it features two well-recognized foreign scientists: (i) Giovanni Montana, Ph.D. – Professor of Biostatistics and Bioinformatics at King's College London, and Visiting Professor of Statistics at Imperial College London (UK); (ii) René Mandl, Ph.D. – Assistant Professor at University Medical Center in Utrecht (Netherlands) with his expertise in diffusion weighted imaging, structural MRI, functional MRI, MR spectroscopy and the development of new analysis methods. The panel further involves Jan Kybic, Ph.D. – Associate Professor and head of Department of Cybernetics of Faculty of Electrical Engineering of Czech Technical University (Prague) – and four representatives of the neuroimaging community in Brno: Tomáš Kašpárek, Ph.D. (Head of Psychiatry Department – Faculty of Medicine and Brno University Hospital), Radovan Jiřík, Ph.D. (Institute of Scientific Instruments of the Academy of Sciences of the Czech Republic), Radek Mareček (Central European Institute of Technology) and Ivo Říha (Neurosurgery Department at St. Anne's University Hospital).

Students' active contributions will make a substantial part of the programme. Student competition at the 10th Summer School of Computational Biology is again under the auspices of Assoc. Prof. Ladislav Dusek, the IBA MU's Director, who announced a reward for the best contributions in three categories for the students of bachelor, master and Ph.D. programmes.

We thank all participating lecturers and all authors of the conference proceedings contributions. This Summer School on Computational Biology would not have been possible without the great administrative support from Mrs. Simona Schneiderová – we would like to express sincere thanks. Special thanks go to Prof. Ing. Jiří Holčík, CSc., who has been coordinating teaching activities and related projects at IBA MU since 2009, and Prof. RNDr. Jiří Hřebíček, CSc., who is the founder and guarantor of the Computational Biology study programme at MU.

We believe that this year event will continue in inspiring our teaching and learning activities.

On behalf of the organizers

Daniel Schwarz & Eva Janoušová

Image Data Analysis and Processing in Neuroscience

Lectures



Significance of the image analysis in contemporary psychiatry

Tomáš Kašpárek^{1,2}

¹ *Department of Psychiatry, University Hospital Brno and Faculty of Medicine, Masaryk University, Brno; e-mail: tkasparek@fnbrno.cz*

² *Behavioral and Social Neuroscience group, CEITEC-MU, Masaryk University, Brno*

Abstract

The paper demonstrates the principles that enable the use of imaging methods in the field of cognitive or mental functions and disorders and the use of neuroimaging in clinical practice. The limitations of the approach are discussed with the critical issue of the knowledge of the biological process behind the changes seen in images that enables their correct interpretation. Besides a number of shortcomings neuroimaging brings significant information that enable deeper insight into the pathogenesis of mental disorders and that, hopefully, will enable objective diagnostics and treatment monitoring in the near future.

Key words

quantitative analysis, neuropathology, brain morphometry

1. Introduction

In one issue of his famous novel *Foundation* Isaak Asimov builds a story around a revolutionary technique of EEG data analysis that enables exploration of personality traits and even prediction of subject behaviour in future critical situations. The idea reflects the richness, stability and subject specificity of an electroencephalographic record that we are not able to decode at present. The question is if we can use them for the diagnostic purposes somehow. Another fiction writer and thinker Stanislav Lem dreamt about a tool that can record human memory traces and image them in an audiovisual modality as a movie. The second question that is reflected in his novel is if we can get access to the subjective inner content of mind, if we can devise tools for mindreading. So let us explore these questions from the point of view of clinical psychiatry.

Modern high-resolution technologies, capable of imaging the structure as well as the function of the CNS, have been used for more than 20 years. They have brought considerable progress in neurosciences and related fields. From the perspective of a clinical psychiatrist, the extensive research in the field of imaging methods seems to have brought virtually no relevant information to practice (except for differential diagnoses of symptomatic mental disorders). Mental disorders have not been shown to have a correlate detectable with common methods used in other branches of clinical medicine. Nevertheless, imaging studies have enabled psychiatry to make remarkable progress in understanding mental illnesses.

A great deal of misunderstanding concerning the significance of imaging methods in psychiatry stems from inadequate differentiation between qualitative and quantitative assessment of images. In clinical practice we use “qualitative” assessments, i.e. we look for qualitatively different characteristics in the image that have pathognomonic significance, for instance a shadow on a lung X-ray or the occurrence of specific epileptiform graphoelements in an EEG. Unfortunately, such specific, pathognomonic qualitative changes are not found in mental disorders.

Quantitative assessment, on the contrary, is based on statistical analysis of the parameters of the image used to detect changes and relationships not perceptible by the naked eye; for example bone densitometry used to detect places in the image of the skeleton in which the 2.5 standard deviation intensity is below the population standard. Quantitative assessment can allow us to test specific hypotheses, i.e., using imaging we can ask and answer clinically relevant psychiatric questions.

We need to realize at what level of abstraction imaging methods work. Any psychopathological process manifests itself at numerous levels, from genetic content, expression of genes and their regulation by epigenetic mechanisms, structure and function of proteins, subcellular structures and mechanisms, cells and cellular interactions, neurophysiological systems, mental functions, personality and partnership, to the individual's social environment. A primary pathology can develop at any of these levels. Through feedback mechanisms, adaptations and maladaptations then occur at the next levels, and, with regard to circular causality (effect influences causes and these changes in turn lead to changes in the effects) making it difficult to identify the cause and the effect of the adaptation. Therefore, the relationships between individual levels are sometimes very difficult to establish; nevertheless, the important fact remains that mental disorders can be understood as changes at many levels of abstraction and that it is possible to try to make use of this information in clinical practice, from diagnosis to therapy. The methods of biological psychiatry can capture changes from the genome to the level of neurophysiological systems (imaging methods). In this respect, it is evident that imaging methods cannot constitute a single, universal approach that can fully explain all psychopathological phenomena. On the contrary, only by integrating information gained from different levels can the findings of imaging methods be understood in the context of the complex pathophysiology of a disorder and be correctly interpreted.

2. Lessons from the schizophrenia research

In 1976, the first CT study involving schizophrenia that demonstrated the presence of enlarged lateral ventricles of the brain was published. This was a ground-breaking study and ever since schizophrenia has been regarded as an illness of the brain with a morphological and neuropathological correlate, and is not the functional illness it was once thought to be. These types of studies revived the interest in the neuropathology of schizophrenia, which, until that time, had been considered the “graveyard” of neuropathologists.

The key neuropathological change seems to be reduction in the thickness of the cortex, primarily of layers II and III. At the same time, a higher density of neurons, smaller sized pyramidal neuron cell bodies and a reduction in the dendritic tree size of these neurons, can be found in these layers. The pyramidal neurons of layers II and III integrate and transmit cortico-cortical connections.

It is possible to assess the thickness of the cortex using magnetic resonance - grey matter density and cortex thickness reflect similar parameters of brain morphology in schizophrenia. Thus, in schizophrenia, using voxel-based morphometry (VBM), we can assess the bulk of the neuropil, i.e., connectivity rate. This means that VBM can be used for assessing the neuropathology of schizophrenia in vivo. In different words – in schizophrenia we can interpret the reduction of gray matter volume in the image of VBM as loss of neuropil on pyramidal cortical neurons.

Unfortunately, until today we cannot use brain morphometry as a proxy measure of treatment outcome. Although there are many reports on the effect of treatment on brain morphology, the animal and human post-mortem studies show that antipsychotics induce changes that in other cortical layers than are those affected by the disease process. The changes seen in brain imaging do not reflect recovery of the pathological process.

Besides the above mentioned, the findings of brain dissimilarities in schizophrenia, ascertained using VBM, have major and direct significance for day-to-day clinical practice: it is exactly because the findings underlie the level of subjective experience that it is possible (or rather, let us hope it soon will be) to communicate more easily with the patient about their illness. On a daily basis, at outpatient clinics and in hospital wards, we meet patients who do not accept the fact that they are mentally ill, or, to put it differently, do not regard the proofs of their illness, as acquired by our subjective assessment of their experience, thinking and behavior, as correct or meaningful. The ability, or even the possibility, of assessing the unique features of an individual's psyche is questioned. If we could tell the patients that the diagnosis is supported by dissimilarity in the morphology or function of their brain, existing parallel to our subjective assessment, it might perhaps be easier to work with their anosognosia.

Imaging studies assess a group of subjects. However, the information value, as regards a single patient, is problematic. The reason is the heterogeneity of the groups of subjects as well as the statistical power of the tests. These difficulties in the assessment of individuals lead to a significant gap between what happens in the laboratory and clinical practice.

This distance can be overcome using modern techniques of analysis and classification of patterns (pattern recognition, detection) and mathematical techniques searching for typical features of the studied group/individual. Then by looking for these features in individual subjects it may be possible to classify them according to their presence/absence (one of the known applications is, for instance, recognition and identification of faces, recognition of fingerprints, etc.). These techniques can also be applied to brain images – in this way it is possible to try to recognize functions that the brain performed during the examination, but there is also the potential to classify subjects as patients or healthy individuals, etc. If we succeeded in verifying the applicability of such methods, it could bring imaging methods closer to clinical practice in psychiatry (diagnosis, prognosis, etc). On the basis of brain imaging, this would become possible. Existing experience has so far been encouraging.

3. Conclusion

Imaging methods enable us to study the neurobiology of mental disorders – they have actually shown that mental disorders do have a neurobiology, that they are not only functional or psychogenic conditions. Imaging methods also contribute to the theoretical understanding of mental disease with cognitive neuroscience allowing us to gain insight into the mechanisms of symptom development. Imaging techniques, with the help of animal and histopathological studies, and in the context of clinical diagnosis, allow assessment of the neuropathology as well as the effect of treatment. Imaging methods may enable subject classification, recognize defined pathological conditions, which might be useful for diagnosis and differential diagnosis; such advancements would improve the relevance of imaging methods to clinical practice. Additionally, imaging methods contribute to the understanding of the mechanism of action of psychotropic medication and allow us to search for the targets of biological treatment. They do not, however, enable access to the contents of the “psyche”, i.e. we are not able to find out WHAT the person perceives, WHAT they are thinking about

and WHAT they remember. The findings of imaging methods do show changes at a level below that of subjective experience, which are accessible through introspection or mediated through interviews. The relationships between the findings of imaging methods and the subjective level can be estimated only from information gained using parallel methods, “indirectly”, and they are, to a varying extent, speculative. Notwithstanding, imaging methods, in the hands of a psychiatrist, represent an invaluable tool for studying mental disorders, with numerous clinical overlaps.

Image registration and its role in computational neuroanatomy

Daniel Schwarz

*Institute of Biostatistics and Analyses, Masaryk University, Brno;
e-mail: schwarz@iba.muni.cz*

Abstract

This part of the proceedings is focused on the field of image registration with the use of various spatial transformations. Image registration is introduced here as a general problem which can be broken down into several components: spatial transformation, similarity measure, interpolation and optimization. Image registration plays a crucial role in algorithms for automated whole-brain morphometry, such as voxel-based morphometry, deformation-based morphometry or source-based morphometry. Basics of these methods as well as their use-cases are explained here.

Key words

Image analysis and processing, image registration, spatial transformation, similarity measure, interpolation, optimization, brain morphometry, voxel-based morphometry, deformation-based morphometry, source-based morphometry.

1. Image registration

Image registration is a process of estimating a spatial transformation which maps each point of an image onto its physically corresponding point of another image (Rohr, 2000). One of its main application fields is biomedical imaging, where the major challenges include finding correspondences between image data from different sensors (multimodal images) and from image databases (e.g. digital atlases). The spectrum of geometric differences between images is very broad including nonlinear image distortions caused by different modalities, time-varying processes or anatomical variability among different subjects (Schwarz, 2005). A universal method does not exist due to the diversity of registration tasks. Various approaches to the classification of image registration methods might be found in general surveys, such as (Maintz and Viergever, 1998; Rohr, 2000; Zitová and Flusser, 2003) or in the review of registration approaches applied to the field of computational neuroanatomy (Gholipour et al., 2007). Selected criteria from (Maintz and Viergever, 1998) to particularly classify methods for intrinsic¹ spatial registration without temporal variability and without any user interaction are shown in Table 1.

Segmentation-based methods require feature detection and feature matching. First, salient objects are extracted and then their correspondence in a subject and a reference images are established. Anatomical salient objects such as posterior and anterior commissures (Talairach, 1988) or hippocampus boundary (Shen et al., 2002) are used less commonly than geometrical salient objects – e.g., skin surface (Pelizzari et al., 1989) – because user supervision is often needed for anatomical landmarks identification. The main drawback of

¹ Intrinsic registration methods are image-based, whereas extrinsic methods rely on foreign objects introduced into the imaged scene.

the segmentation-based methods is the dependence of the registration accuracy on the achieved segmentation precision. Although they are used with medical images very often, their main fields of application are computer vision and remote sensing, where the structural information contained in images is much more apparent than in medical imaging applications. The main advantage of these methods is a sparse set of identified points when compared to the original image content, which makes for relatively fast optimization procedures.

Table 1. Classification of image registration approaches (Schwarz, 2005)

Registration basis	Nature of transformation	Domain of transformation	Optimization	Modalities involved	Subject
segmentation based	linear	global	parameters computed	mono-modal	intra-subject
voxel based	nonlinear	local	parameters searched for	multi-modal	inter-subject

Voxel-based methods operate directly on image gray values with no data reduction by segmentation. Coarse preregistration is done by aligning centers of gravity, taking the image intensity as a mass density in (Collins et al., 1994; Ibáñez and Insight Software Consortium, 2003). In addition, alignment of principal orientations computed from image moments is done in (Ding et al., 2001). Methods using full image content are considered in this work mainly. The spatial correspondence between the reference and the object image is evaluated by a similarity measure. Choice of the similarity measure depends mostly on characters of intensities in the reference and the subject image or, in other words, it depends on monomodality or multimodality of data coming into registration. While absolute or squared difference is a suitable measure of similarity for monomodal data, it cannot be used on multimodal registration. Intensity difference is used to drive registration most often in warping methods based on continuum mechanics (Bro-Nielsen and Gramkow, 1996; Christensen et al., 1996; Ferrant et al., 1999; Tang and Jiang, 2004), optical flow (Hata et al., 2000) or diffusion (Thirion, 1998, 1996). Cross correlation is used when a linear relation between reference and subject image intensities is expected, such as in (Collins et al., 1995, 1994). Fourier-based registration techniques proved to be suitable when images corrupted by frequency dependent noise have to be registered (Hoge et al., 2003). Mutual information-based methods (Capek et al., 2001; Ibáñez and Insight Software Consortium, 2003; Kubecka and Jan, 2004; Maes, 1998; Maes et al., 1997; Maintz et al., 1998; Pluim et al., 2001; Schwarz and Provaznik, 2002a, 2002b; Unser and Thevenaz, 2000; Viola and Wells, 1995) represent a leading technique in multimodal registration. It measures statistical dependency between two datasets; details are given further in the text. The multimodal similarity measures can be avoided by applying an intensity transformation on one of the images, so that it matches the intensity properties of the other image. The reason for that is in the following possible use of an already settled monomodal registration algorithm (Ashburner and Friston, 1999; Guimond et al., 2001; Ibáñez and Insight Software Consortium, 2003).

Various transformation types are used for various registration tasks. Rigid body and affine transformations are linear mappings used mostly. A rigid body transformation consists of translations and rotations only. It can be described by six parameters in 3D coordinate system (three parameters for translations and three parameters for rotations). If the voxel size differs in the subject image and the reference image, one or three additional parameters for uniform

or non-uniform scaling are involved. Thus, a seven-parameter or a nine-parameter affine transformation is composed. If shearing has to be covered, twelve parameters for an affine transformation have to be found. Linear transformations are used for global mappings, which get the subject image into the coordinate system of the reference image. The subject image can be aligned with a template image of an anatomical atlas (Collins et al., 1994) or patient repositioning can be corrected in this way (Rohlfing et al., 2003; Rueckert et al., 1999).

Nonlinear transformations are often referred as non-rigid. They are described by far more parameters (degrees of freedom) than the linear ones. They are based on polynomials (Woods et al., 1999), various basis functions such as cosine basis functions (Ashburner and Friston, 1999), radial basis functions (RBF) (Buzug et al., 1997; Fornefett et al., 2001), B-splines (Xie and Farin, 2001) or a physical model such as an elastic model (Ferrant et al., 2001, 1999) or a fluid model (Bro-Nielsen and Gramkow, 1996; Christensen et al., 1996). Nonlinear transformations are used when misalignments remaining after a linear transformation have to be suppressed. The misalignments are caused among others by anatomical variability between various subjects, by different geometrical distortions introduced during acquisition process from various modalities, by a deformation caused by introducing foreign objects into the scene or by tissue changes or a motion. Nonlinear transformations are referred as deformations further in this work. They are computed from local forces estimated with the use of a similarity measure.

Global transformations are applied to the entire image, whereas local transformations are applied to subsections of the image, which can be blocks of an arbitrary size, even individual voxels. Apparently, affine and rigid body transformations are used globally, whereas deformations are used locally.

Parameters which make up the spatial transformation are computed or searched for. Direct computation of a global transformation is usually based on a sparse set of corresponding points in the subject and the reference image. Thus, these methods are restricted to the use of segmentation-based methods. In the case of voxel-based methods, the parameters of a global transformation are searched for. A cost function formed by a similarity measure (or its negative) as a function of transformation parameters is formulated and its minimum is searched. This approach is referred as optimal registration (Modersitzki, 2004) and can be used also for local transformations computed on subsections of original images (Maintz et al., 1998; Schwarz and Provazník, 2002a, 2002b). Various optimization techniques with the use of derivatives, such as Marquardt–Levenberg method (Unser and Thevenaz, 2000) or Gauss–Newton method (Ashburner and Friston, 1999), as well as without derivatives, such as Powell's method (Maintz et al., 1998; Schwarz and Provazník, 2002a, 2002b), Nelder–Mead's method (Collins et al., 1994) or the random search algorithms such as simulated annealing (Capek et al., 2001) or controlled random search (Kubecka and Jan, 2004) are used depending mainly on the behavior of the cost function. Multiresolution techniques are often employed (Capek et al., 2001; Ibáñez and Insight Software Consortium, 2003; Pluim et al., 2001) to avoid local minima and to speed up convergence of the optimization. Local transformations can be besides optimization computed also directly e.g. by optical flow methods (Hata et al., 2000) or by registration methods based on diffusion (Thirion, 1998, 1996).

In monomodal applications, the images to be registered are acquired from the same modality, whereas multimodal registration methods process images from two different modalities. Registration of MRI data with different contrast weightings is regarded as multimodal in this work as the characters of intensities differ in the images obtained with various pulse sequences, see Figure 1a. A checkerboard composite of T1-weighted image of an individual

and a template image constructed as an average of 305 registered T1-weighted images of various subjects is in Figure 1b. The classification of such atlas based registration is not straightforward. Due to various characters of intensities in the images, this kind of registration is also regarded as multimodal in this work.

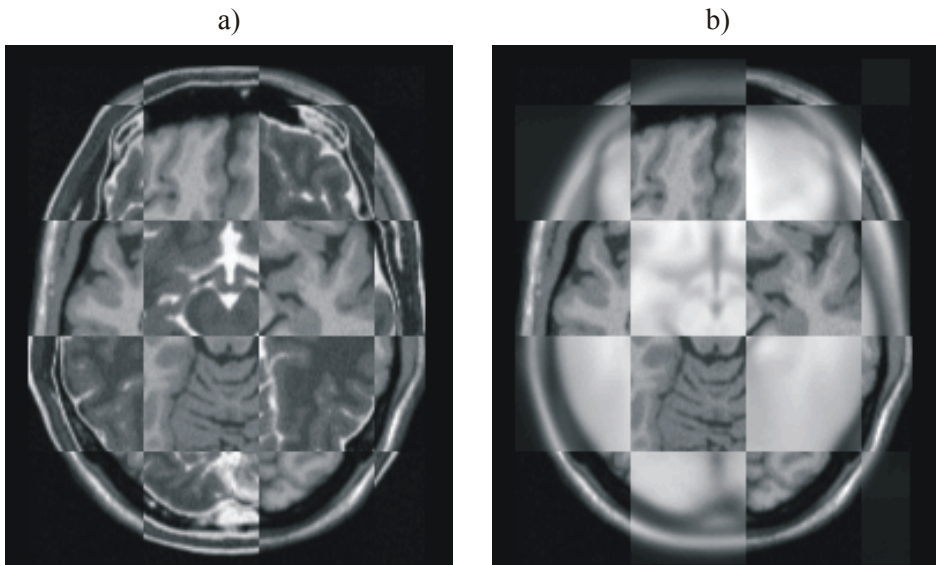


Figure 1. Checkerboard composite of registered images after a) multimodal intrasubject registration (MR-T1/MR-T2), b) multimodal intersubject registration (MR-T1/average of 305 individuals) (Schwarz, 2005).

Registration is referred as intrasubject if image data acquired from a single patient have to be aligned. If image data of different patients come into registration, it is referred as intersubject registration. Atlas-based registration is accomplished with a patient image and an image of a “normal” subject or a template image constructed from a database of images of many subjects representing certain population. Hence, atlas based registration is considered as intersubject registration here.

1.1. Components of registration methods

Image registration can be defined as an optimization problem with the goal of finding the spatial mapping that will bring the floating image N into alignment with the reference image M . Figure 2 shows its basic steps. It is in fact a general framework of any registration where parameters of the spatial mapping cannot be computed directly.

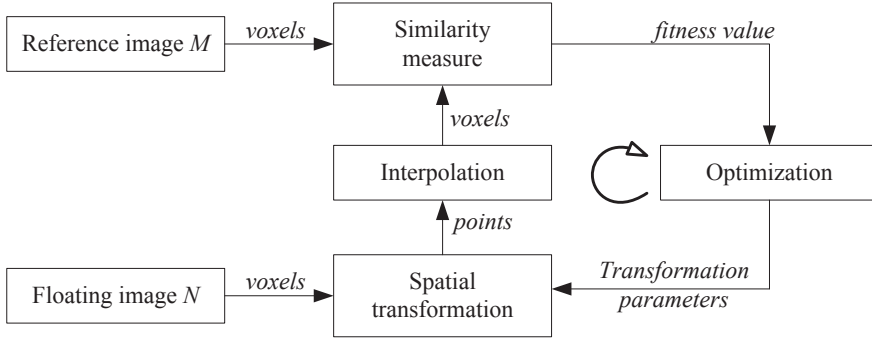


Figure 2. Basic components of an optimal registration framework (Ibáñez and Insight Software Consortium, 2003).

1.1.1. Transformations and spatial deformation models

The spatial transformation φ_a^{-1} maps points from the reference image space to points in the floating image space. It is parameterized by a vector of parameters a . It is in fact an inverse mapping which is preferable as it avoids problems of holes with the forward mapping, see Figure 3.

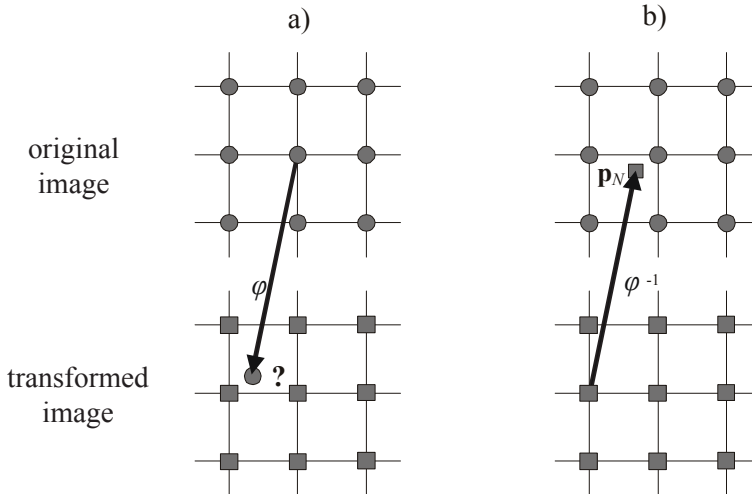


Figure 3. a) Forward and b) inverse mapping. The intensity in the non-grid point \mathbf{p}_N is interpolated from surrounding voxels in the original image (Schwarz, 2005).

Affine transformation in 3-D space can be described by a single 4×4 matrix \mathbf{A} :

$$\mathbf{A} = \mathbf{TSGR}, \quad (1)$$

where \mathbf{R} , \mathbf{G} , \mathbf{S} , \mathbf{T} are 4×4 matrices representing rotation, shearing, scaling, and translation respectively. The matrices are usually notated in homogeneous coordinates which allow

representing translation by a matrix and thus composing it with other transformations. A general affine transformation has 12 parameters: three translation shifts t_x, t_y, t_z along x, y and z -axis; three angles of rotations α_x, α_y and α_z ; three shearing parameters g_x, g_y, g_z ; and three scaling factors s_x, s_y, s_z . By setting all three shearing parameters to $g_x = g_y = g_z = 0$ a reduced nine-parameter affine transform is obtained. By setting all three scaling parameters $s_x = s_y = s_z = k$, where k represents an isotropic scaling factor, a reduced seven-parameter affine transformation, termed as a similarity transformation, is obtained. Setting $k = 1$ yields a rigid body transformation composed only from translations and rotations.

In many medical imaging applications, the global alignment provided by an affine transformation does not provide a sufficient solution. A spatially dependent deformation is then necessary to correct the local differences remaining in the images. The mapping function of a deformation $\varphi(\mathbf{x})$ is usually split into the trivial identity part and a so-called displacement field $\mathbf{u}(\mathbf{x})$ (Modersitzki, 2004):

$$\varphi(\mathbf{x}) = \mathbf{x} + \mathbf{u}(\mathbf{x}). \quad (2)$$

Computation of the displacement field involves local forces together with regularization provided by a spatial deformation model. Regularized mapping function ensures realistic registration results without tearing or folding of the image. The spatial deformation model is more or less physically motivated, depending on the particular application (Schwarz, 2005).

Parametric deformations are given in terms of basis functions ψ_i and corresponding parameters a_i . Once the set of basis functions is chosen, the registration task is limited to determine the parameters of the deformation. Methods based on scattered data interpolation with the use of radial basis functions (RBFs) are used widely. Wendland's functions and thin-plate splines are examples of RBFs used in image registration. In (Kostelec et al., 1998), local forces are represented by translation and rotation parameters obtained from several rigid monomodal registrations performed on 2-D image quadrants. The spatial deformation is modelled by interpolation of the local translation and rotation parameters with the use of thin-plate splines. Similarly in (Buzug et al., 1997), motion vector field between 2D images from digital subtraction angiography is obtained by locally optimizing histogram-based energy measure. Thin-plate splines are then used to interpolate the motion vector field to get the resulting mapping function which serves for correction of the motion artifact. Point landmarks are used in (Pauchard et al., 2004) to identify distortions caused by metallic implants in MR imaging. Ideal interpolation, and therefore an exact alignment of the point pairs, is not expected due to point localization errors. These are compensated by regularization factor which relaxes the interpolation condition in exchange for a smoother mapping function. Thin-plate splines are widely used for their physical interpretation based on minimum bending energy of a thin sheet of metal. Such a physical analogy makes their use conveniently intuitive. On the other hand, the bending energy is measured over the whole image, thus the resulting deformation is not limited to regions where the local forces act. This behavior is advantageous for yielding overall smooth deformations, but it is problematic when rather local deformations limited to image parts are desired (Fornefett et al., 2001). Figure 4 shows the difference between deformations computed with the thin-plate splines and Wendland's functions. Other RBFs, such as inverse multiquadrics (Ruprecht and Müller, 1993) or Wendland's functions with compact support (Wachowiak et al., 2004) are investigated for image deformations. In (Fornefett et al., 2001), Wendland's RBFs are proposed for image registration based on point landmarks. A significant reduction of global

influence together with high computational efficiency compared to other RBFs is reported there.

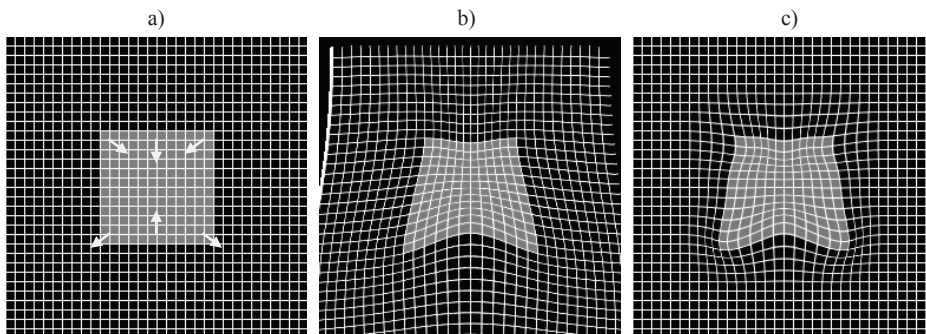


Figure 4. a) A synthetic image under six local forces. The displacement field is computed with the use of b) thin-plate splines, c) Wendland's functions with compact support (Schwarz, 2005).

Other functions with compact support are cubic B-splines. They are used in (Rohlfing et al., 2003; Rueckert et al., 1999; Schnabel et al., 2003) as basis functions for spatial deformation model in registration of breast images from contrast-enhanced MRI to recover a motion artifact. The local forces are represented by moving control points from their initial uniform grid spread over the whole images. Although the forces act locally, they are obtained by optimizing a cost function made up from a global similarity measure, which is normalized mutual information, and various penalty terms. One of them is a smoothness constraint given by minimizing the bending energy of a thin metal plate. Another one is an incompressibility constraint penalizing tissue compression and expansion which are indicated by local deviations of deformation's Jacobian determinant from unity. A trade-off between the deformation smoothness or volume preservation and the required reduction of motion artifact is discussed there. The unconstrained registration produces lower residual artifacts, whereas a lower number of getting stuck in local optima is reported in the case of the constrained registration. Another parametric deformable registration method based on constrained optimization is proposed in (Ashburner and Friston, 1999) for so-called spatial normalization – mapping brain images into a standard space. The nonlinear transformation is parameterized with low-frequency components of discrete cosine transform. The optimization involves minimizing the sum of squared differences between the images together with a constraint based on Bayesian statistics - a maximum a posteriori estimate of the mapping function parameters is searched. Knowledge about a priori parameter distributions is assumed to be known. The final remark to the state of art of parametric deformable registration belongs to a natural extension of the Fourier model: wavelet basis functions are investigated in (Downie and Silverman, 2001) for modeling the displacement field in the floating image without neglecting localized high-frequency features.

Multilevel deformation for a block matching registration algorithm is proposed in (Schwarz and Provazník, 2006; Schwarz, 2005). Smooth deformations with the displacement field $\mathbf{u}(\mathbf{x})$ are computed by scattered data interpolation based on compactly supported Wendland's RBFs:

$$u_k(\mathbf{x}) = \sum_{i=1}^B (\alpha_i \cdot R(\|\mathbf{x} - \mathbf{w}_i\|)), \quad k = 1 \dots D, \quad (3)$$

where $u_k(\mathbf{x})$ is the displacement of a grid point \mathbf{x} in the k^{th} dimension, R is the radial basis function of the distance $\|\mathbf{x} - \mathbf{w}_i\|$ between the grid point \mathbf{x} and the center of the i^{th} block \mathbf{w}_i . The coefficients α_i are computed by putting the displacements of the image blocks, found by regional similarity matching, on the left side of the equation (3) and solving the resulting linear system of B equations separately for each dimension k . Mathematical properties of Wendland's RBFs hold for different spatial support which is important for the multilevel strategy. For each level of subdivision, the image block size is set to the half of the size at the previous level. The displacements are gradually incremented over all levels, refining the resulting deformation in the coarse-to-fine manner. The regions containing poor contour or surface information can be eliminated from the matching process and the algorithm can be accelerated in this way, see Figure 5.

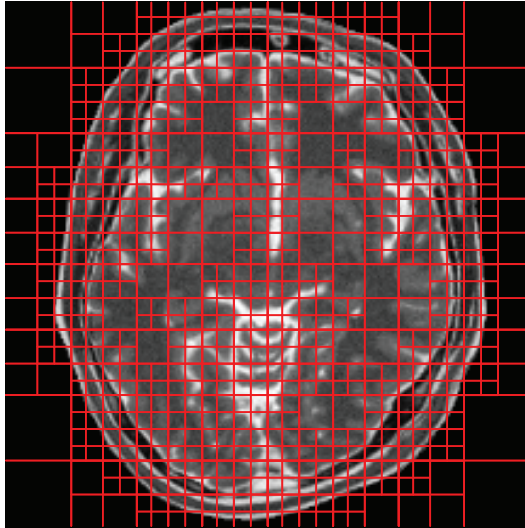


Figure 5. Illustration of five-level adaptive subdivision. The subdivision is performed only if at least one voxel in the current region has its normalized gradient image intensity bigger than a certain threshold (Schwarz and Provazník, 2006).

The support length of Wendland's RBFs cannot be set arbitrary, as there is a fundamental condition of topology preservation, i.e. one-to-one mappings termed as diffeomorphic (Modersitzki, 2004) are required. This requirement is satisfied if the determinant of the Jacobian of the deformation is non-negative (Karaçalı and Davatzikos, 2003):

$$\det \nabla \varphi \geq 0, \quad (4)$$

$$\nabla \varphi = \begin{pmatrix} \frac{\partial \varphi_1}{\partial x} & \frac{\partial \varphi_1}{\partial y} & \frac{\partial \varphi_1}{\partial z} \\ \frac{\partial \varphi_2}{\partial x} & \frac{\partial \varphi_2}{\partial y} & \frac{\partial \varphi_2}{\partial z} \\ \frac{\partial \varphi_3}{\partial x} & \frac{\partial \varphi_3}{\partial y} & \frac{\partial \varphi_3}{\partial z} \end{pmatrix}, \quad (5)$$

where φ_1 , φ_2 and φ_3 are components of the deformation over x , y and z axes respectively. Figure 6 shows values of the determinant of the Jacobian estimated by symmetric finite differences. The image is undesirably folded in the positions, where the determinant of the Jacobian is negative. In such a case, the mapping is not invertible.

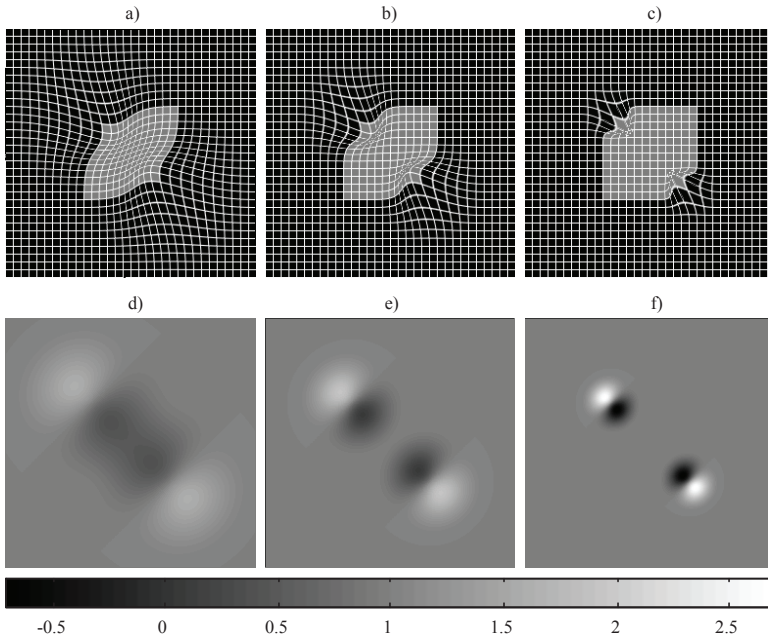


Figure 6. Deformations computed with the use of Wendland's RBFs with various degree of locality (support length) and the same magnitude of local forces (displacements). A stiffer material is modelled with a bigger value of the support parameter of Wendland's RBFs: a), whereas a more flexible material is modelled by a smaller value in the support parameter: c). It is worth to note that this modelling is intuitive only, as there is no validation study that the deformations based on Wendland's RBFs are physically plausible. Preservation of topology is observed by the value of Jacobian determinant: d), e), f). (Schwarz, 2005)

Instead of applying piecewise interpolation to compute a displacement field which maps the control points of one image onto another, non-parametric deformations define a displacement vector in every point most often by imitating real world transformations of deformable materials. The local forces, which drive the registration process, are counterbalanced by constraints defined by the spatial deformation model. The constraints are used to restrict the

transformation to an appropriate class depending on a particular application. Besides various smoothness constraints, stiffness constraints based on continuum mechanics are used typically (Schwarz, 2005).

One of the first proposed methods based on continuum mechanics was elastic matching (Ferrant et al., 2001, 1999; Modersitzki, 2004). Only small deformations are assumed, thus linear elastic model can be used. Elastic matching is interesting method in the area of intrasubject registration and it is still used, mainly for biomechanical image registration (Alterovitz et al., 2004). Unfortunately, it fails in intersubject situations, where large and localized deformations are desired. In (Christensen et al., 1996), a viscous fluid model is used to control the deformation. The floating image is modelled as a thick fluid that flows out to match the reference image under the control of the local forces. Convolution filter methods for solving associated partial differential equations (PDE) are proposed in (Bro-Nielsen and Gramkow, 1996; Gramkow et al., 1997). Various solvers of the PDE are discussed in (Wollny and Kruggel, 2002) with regard to the computational cost. A considerable piece of work is presented in (Rogelj and Kovačič, 2004; Rogelj, 2003), where Gaussian filters are used for modelling the spatial deformation. The Gaussian filters are used to approximate the elastic as well as the fluid model. It is also successfully used for a so-called incremental model, which is used for image registration also in (Peckar et al., 1998). A spatial deformation model made up from the elastic and the incremental model is proposed, in order to combine their advantages and thus improve the registration. Its design follows the concept of solving partial differential equation associated with linearized elasticity or viscosity by convolution filtering, where the filter kernel equals the impulse response of the deformable media. The displacement is computed as a reaction of local forces exerted in an image:

$$\begin{aligned} \mathbf{u}_f &= k\mathbf{f}, \\ \mathbf{u}^i &= (\mathbf{u}^{i-1} + \mathbf{u}_f * \mathbf{G}_I) * \mathbf{G}_E, \end{aligned} \tag{6}$$

see the scheme in Figure 7. The first part follows the Hooke's law to compute unregularized displacements. It says that the points move proportionally to the applied forces \mathbf{f} with a constant k . The second part of (6) regularizes the displacements by convolution filters \mathbf{G}_I and \mathbf{G}_E which define spatial deformation properties of the modeled material. Gaussian kernel as a separable approximation to the elastic kernel is used here. Besides its lower computational cost, the registration results obtained with the Gaussian kernel are reported in (Rogelj and Kovačič, 2004) to be more precise than the results obtained with the elastic kernel in the case when the forces driving the registration differ from the forces which in reality deformed the anatomy, such as in the case of intersubject registration. The separable Gaussian kernel does not provide control over compressibility, due to independence of spatial dimensions. While this property is disadvantageous in particular registration tasks, it is required in the case of intersubject registration.

1.1.2. Similarity measures

The choice of an appropriate similarity measure to be used in a registration algorithm is substantially determined by the character of intensities in the floating and the reference image. Popular choices, which are based on intensity, correlation and mutual information, are clearly derived and defined in (Ibáñez and Insight Software Consortium, 2003).

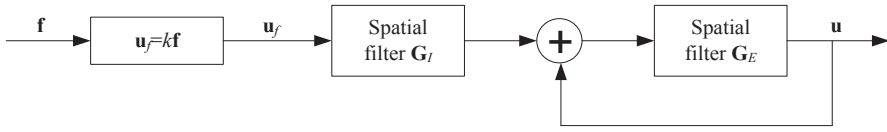


Figure 7. The combined elastic-incremental model (Rogelj and Kovačič, 2004). The first filter G_I regularizes displacement improvements u_f and the second filter G_E regularizes the overall displacement field u .

Intensity-based registration incorporates typically the so-called sum of squared differences (SSD), which relies on the assumption that intensity representing the same homologous point must be the same in both images. Hence, its use is restricted to images of the same modality. It can be used also for multimodal registration, if an intensity transform is applied on one of the images, in order to obtain the same character of intensities in both images.

Voxel-wise cross-correlation normalized by the square root of the autocorrelation of the images is typically used in correlation-based registration. Unlike the SSD measure, it is insensitive to multiplicative factors between the images.

Supposing the image intensities to be discrete random variables, their mutual information (MI) can be defined in terms of entropy known from information theory:

$$\begin{aligned}
 I(M, N) &= H(M) + H(N) - H(M, N) = \\
 &= \sum_{m,n} p_{MN}(m, n) \log_2 \frac{p_{MN}(m, n)}{p_M(m)p_N(n)},
 \end{aligned} \tag{7}$$

where $I(M, N)$ is the mutual information of random variables M and N , $H(M)$ and $H(N)$ are entropies of M and N respectively and $H(M, N)$ is the joint entropy of M and N . The entropy $H(M)$ is known to be a measure of the amount of uncertainty about the random variable M . The entropies are defined in terms of marginal probability density functions (PDF) $p_M(m)$ and $p_N(n)$, and the joint PDF $p_{MN}(m, n)$ of the random variables. If M and N are independent, then their mutual information is zero. In the case of dependency between M and N , their mutual information has a positive value. The major advantage of using MI for measuring the strength of the dependence between random variables is the fact that the actual form of the dependency does not have to be specified. Therefore, MI is well suited as a criterion of multimodal registration.

The marginal and joint PDFs can be estimated from image data by Parzen windowing, such as in (Modersitzki, 2004; Unser and Thevenaz, 2000; Viola and Wells, 1995) or by normalizing the joint histogram and summing over its rows and columns, such as in (Maes, 1998; Maintz et al., 1998). Examples of the joint PDF estimates of misregistered as well as of registered MRI images are shown in Figure 8 – a general, undefined, but certain dependency between the intensities in the images can be observed. Higher peaks in “sharper” density of registered images correspond to true tissue pairs - intensity ranges representing the same tissue in both images. On the other hand, higher number of false tissue pairs in the case of misregistered images “smears out” the density function. The mutual information is larger in the registered than in the misregistered case. The similarity criterion is therefore defined by:

$$S^{MI}(M, N) = - \sum_{m,n} p_{MN}(m, n) \log_2 \frac{p_{MN}(m, n)}{p_M(m)p_N(n)}. \quad (8)$$

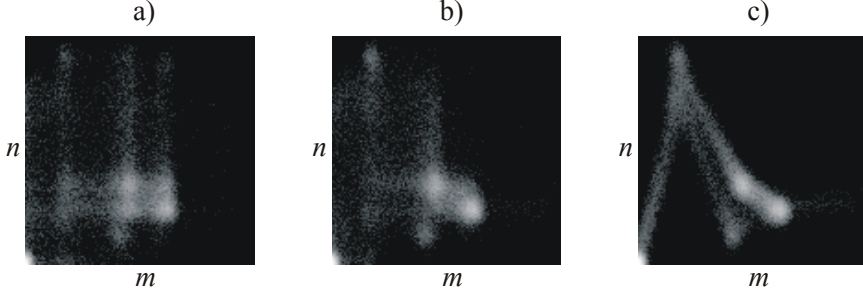


Figure 8. 2-D logarithmic plot of joint PDF $p_{MN}(m,n)$ estimates for T1-weighted and T2-weighted images in: a) misregistered position - translated and rotated, b) misregistered position - translated only, c) registered position. (Schwarz, 2005)

The registration methods which were first to perform high-dimensional warping were typically limited to monomodal data, e.g. (Bro-Nielsen and Gramkow, 1996; Christensen et al., 1996; Thirion, 1998). The continuous efforts of medical imaging community to develop registration algorithms with high-dimensional matching of multimodal data have recently borne fruit.

In (Rogelj et al., (2003), point similarity measures are proposed for high dimensional deformable registration of multimodal data. The point similarity measures are derived from global similarity measures based on the joint PDF estimated from the joint histogram, such as MI. The equation (7) can be rewritten to:

$$\begin{aligned} I(M, N) &= \sum_{m,n} \frac{K_{m,n}}{K} \log_2 \frac{p_{MN}(m, n)}{p_M(m)p_N(n)} = \\ &= \frac{1}{K} \sum_{\mathbf{x}} \log_2 \frac{p_{MN}(m(\mathbf{x}), n(\mathbf{x}))}{p_M(m(\mathbf{x}))p_N(n(\mathbf{x}))} = \\ &= \frac{1}{K} \sum_{\mathbf{x}} S_{MI}(\mathbf{x}). \end{aligned} \quad (9)$$

The global mutual information is thus computed as an average of K point similarities S_{MI} defined for each voxel \mathbf{x} . The final summation is taken over spatial coordinates instead of intensities thanks to the fact that $K_{m,n}$ is the number of occurrences of the intensity pair $[m, n]$ and K is the total number of intensity pairs, which equals to the number of overlapping voxels (Schwarz et al., 2007). The point similarity measure $S_{MI}(\mathbf{x})$ derived from the global mutual information is thus defined as (Rogelj et al., 2003):

$$S_{MI}(\mathbf{x}) = \log_2 \frac{p_{MN}(m(\mathbf{x}), n(\mathbf{x}))}{p_M(m(\mathbf{x}))p_N(n(\mathbf{x}))}. \quad (10)$$

In (Maintz et al., 1998), conditional probability densities are used for a region similarity measure and it is in (Schwarz et al., 2007) rewritten as another point similarity measure:

$$S_{PC}(\mathbf{x}) = p(n(\mathbf{x})|m(\mathbf{x})). \quad (11)$$

Other point similarity measures are proposed in (Rogelj et al., 2003) and further explored and evaluated in a high-dimensional deformable registration used for automated morphometry of MRI brain images (Schwarz et al., 2007):

$$S_U(\mathbf{x}) = \frac{p_{MN}(m(\mathbf{x}), n(\mathbf{x}))^2}{p_M(m(\mathbf{x}))p_N(n(\mathbf{x}))}, \quad (12)$$

$$\begin{aligned} S_{UH}(\mathbf{x}) &= \log_2 p_{MN}(m(\mathbf{x}), n(\mathbf{x})) + \\ &+ \log_2 \frac{p_{MN}(m(\mathbf{x}), n(\mathbf{x}))}{p_M(m(\mathbf{x}))p_N(n(\mathbf{x}))} = \\ &= S_H + S_{MI}. \end{aligned} \quad (13)$$

These are measures expressed in terms of probability (S_{PC} , S_U) and uncertainty (S_{MI} , S_H , S_{UH}). Experiments performed in (Schwarz et al., 2007), based on recovering synthetic deformations, showed better registration quality involving the probability similarity measures. Another point similarity measure dependent on probability is proposed there:

$$S_{PMI}(\mathbf{x}) = \frac{p_{MN}(m(\mathbf{x}), n(\mathbf{x}))}{p_M(m(\mathbf{x}))p_N(n(\mathbf{x}))}. \quad (14)$$

It is derived from S_{MI} such that there is the same relationship between S_{PMI} and S_{MI} as in the case of S_U and S_{UH} . The log function, which may straighten out the differences between similarities of correctly and incorrectly registered tissues, is removed.

Results of the measurement of similarity depend on the registration direction. The resulting deformations obtained from the direct registration of an image N to an image M and the registration in the opposite direction are not inverse to each other. It is caused by similarity measure's inability to uniquely describe the correspondences of regions or points. This asymmetric relation leads to registration inconsistency and reduces the quality of registration. Therefore, various consistent registration methods have been proposed. In (Schwarz et al., 2007), the local forces, which drive the registration process properly, are computed for each voxel independently as the differences between forward forces and

reverse forces, using the symmetric registration approach taken from (Christensen and Johnson, 2001; Rogelj and Kovačič, 2006). The forces are estimated by the gradient of a point similarity measure. The derivatives are approximated by central differences, such that the k^{th} component of a force at a voxel \mathbf{x} is defined as:

$$\begin{aligned}
 f_k(\mathbf{x}) &= f_k^{\text{forward}}(\mathbf{x}) - f_k^{\text{reverse}}(\mathbf{x}) = \\
 &= \frac{S(M(\mathbf{x} + \mathbf{u}(\mathbf{x}) + \varepsilon \varepsilon_k), N(\mathbf{x})) - S(M(\mathbf{x} + \mathbf{u}(\mathbf{x}) - \varepsilon \varepsilon_k), N(\mathbf{x}))}{2\varepsilon_k} \\
 &\quad - \frac{S(M(\mathbf{x}), N(\mathbf{x} - \mathbf{u}(\mathbf{x}) + \varepsilon \varepsilon_k)) - S(M(\mathbf{x}), N(\mathbf{x} - \mathbf{u}(\mathbf{x}) - \varepsilon \varepsilon_k))}{2\varepsilon_k}, \tag{15} \\
 &k = 1 \dots D,
 \end{aligned}$$

where ε_k is a voxel size component, see Figure 9. In the case of the forward forces, the displacement obtained in foregoing iterations $\mathbf{u}(\mathbf{x})$ moves the voxel \mathbf{x} of the floating image N to match it with the voxel $\mathbf{x} + \mathbf{u}(\mathbf{x})$ of the reference image M . In the case of the reverse forces, the voxels of the reference image M are displaced in the opposite direction. In this way, both force fields are computed on the regular grid, assuming the same coordinate space for the images M and N . The point similarity measure is evaluated in nongrid positions due to the displacement field applied on the image grids. Thus, interpolation from neighboring grid points has to be involved.

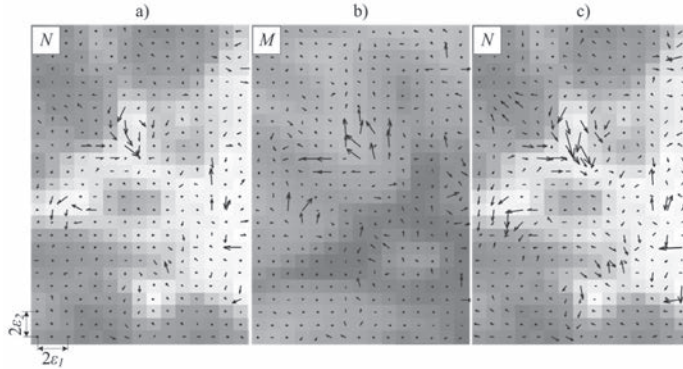


Figure 9. Selected parts of the force fields: a) the forward forces deform the floating image N to match it with the reference image M , b) the reverse forces tend to improve matching of the image M according to the image N , c) the symmetric forces exerted on the image N . (Schwarz et al., 2007)

1.1.3. Optimization techniques

An optimization technique is needed to find the spatial transformation defined by a vector of transformation parameters $\mathbf{a} = [a_1, \dots, a_D]$. The number of parameters D ranges from six, for rigid body transformation, to twelve, for general affine transformation, or to thousands for high-dimensional deformations. Optimization methods with no gradient computation requirement are typical for correlation-based and mutual information based criterions. Powell's directions set method (Maintz et al., 1998; Pluim et al., 2001), downhill simplex

method (Collins et al., 1994) are selected examples in the case of linear optimal registration, see Figure 10. Global optimization techniques, such as evolutionary algorithms and simulated annealing (Capek et al., 2001; Kubecka and Jan, 2004) are characterized by quite slow convergence rates and have been used only rarely in medical image registration (Gholipour et al., 2007)

Most of the widely used optimization algorithms, including gradient descent, quasi-Newton and Levenberg-Marquardt require derivative calculation. Analytical expressions for the gradient of similarity measures have shown to be effective in speeding-up the calculation and achieving smoother and more robust optimization. The gradient expressions for various similarity measures are derived based on a variational formulation in (Hermosillo et al., 2002).

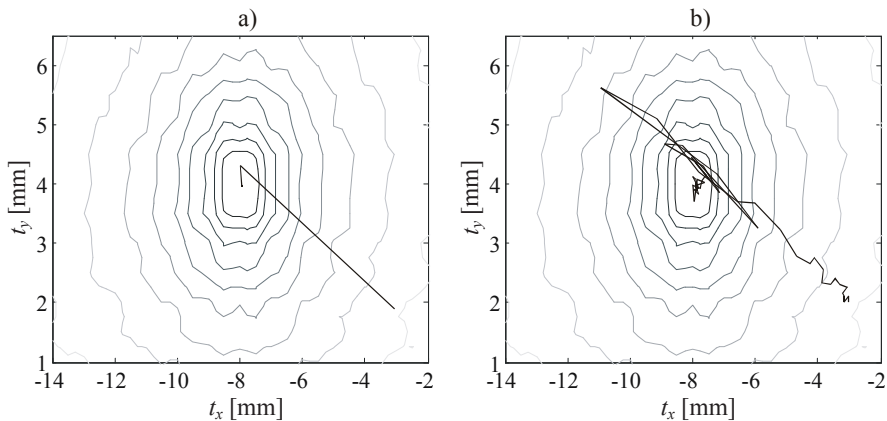


Figure 10. Trajectories of 2-D optimization performed by: a) Powell's direction set method, b) Nelder-Mead's downhill simplex method. Two MRI images with different contrast weightings were put into registration based on MI. They were misregistered before by a translation in the x and y axis. The registration was initialized at a random point near the optimum. There were 3 iterations, i.e. 6 line minimizations requiring 190 calculations of the cost function for Powell's direction set method, whereas 31 iterations requiring 61 calculations of the cost function had to be done with Nelder-Mead's downhill simplex method, reaching the same convergence criterion as in the former case. Running of the line minimizations required by Powell's method are not included (Schwarz, 2005).

A multiresolution approach to image registration is widely used to improve its speed and robustness. The basic idea is that the optimization routines are repeatedly initialized with parameters obtained by previous registration performed at a coarser scale. Besides increasing the speed of the whole registration process, this coarse-to-fine strategy improves robustness by eliminating local optima at coarser scales (Maes et al., 1999; Pluim et al., 2001; Unser and Thevenaz, 2000).

Figure 11 – retrieved from (Schwarz et al., 2007) – shows that deformable registration based on the point similarity measures is less precise for large initial misalignments according to lower values of global similarity measure at the end of the registration process. It is caused by two types of error: (i) incorrect estimation of point similarity function from misaligned images leads to computation of forces which do not drive the registration properly; (ii) the complexity of brain images together with gradient-based computation of forces lead to suboptimal registration solutions. The influence of the second type of the error is reduced in (Schwarz et al., 2007) with the use of the multiresolution strategy. Registration is performed

in multiple resolutions on a prepared sequence of downsampled images. To generate these images, Gaussian smoothing and subsequent sub-sampling are performed. Registration starts at the coarsest resolution level and the resulting deformation initializes registration on the finer resolution level. Each change of resolution requires resampling of the displacement field obtained in the preceding level. The registration convergence with and without the multiresolution strategy is compared in Figure 12.

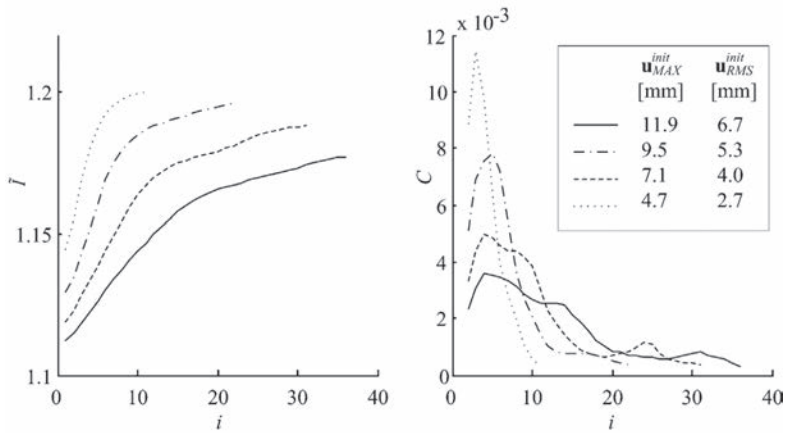


Figure 11. The convergence of the registration for various degrees of initial image misalignment. The initial misalignment is expressed by the maximum displacement \mathbf{u}_{MAX}^{init} and the root-mean-squared displacement \mathbf{u}_{RMS}^{init} . The number of iterations i is the highest when the images are misaligned by the largest deformation and it is lowest in the case of registration of images which are closely aligned. (Schwarz et al., 2007)

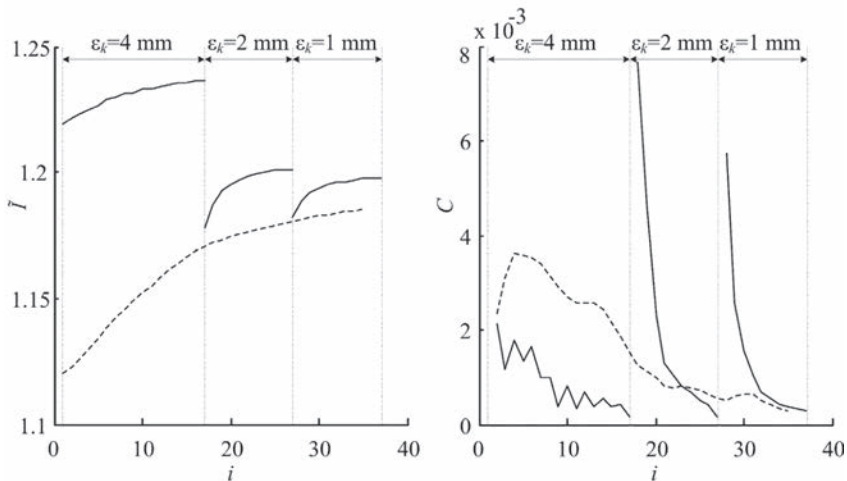


Figure 12. The convergence of the registration with the use of the three-level multiresolution scheme (solid line) and without the multiresolution scheme (dashed line). (Schwarz et al., 2007)

1.1.4. Interpolation

Interpolation is used within each iteration of the registration algorithm, as the points are generally transformed into non-grid position, see Figure 3. Besides the overall computation time, the interpolation method influences also smoothness of the optimization search space and hence the registration accuracy.

Higher-order interpolation methods with larger kernels, such as cubic B-splines, lead to smaller intensity errors in the interpolated image. It has been shown, however, that these interpolators do not always ensure also higher registration accuracy, especially in the case of MI-based registration (Tsao, 2003). The voxel intensities are binned to a finite number of the histogram entries before the similarity measure is calculated. Due to this rounding, much of the additional accuracy obtained by higher-order interpolation is lost. In addition, the interpolation error varies depending on the extent of grid alignment, causing spatial discontinuity of the similarity measure, termed as interpolation artifact. It is different from the conventional sense of the term, which refers to the effect of interpolation on image quality. Here, it refers to the effect of interpolation on the similarity measure (Tsao, 2003).

To alleviate the problems associated with direct intensity interpolation methods, partial volume interpolation (PVI) was proposed in (Maes, 1998) for mutual information based registration. It was further extended to a scheme called generalized partial volume joint histogram estimation (GPVE) (Chen and Varshney, 2003) and used in multimodal registration with the use of low-dimensional deformations and regional similarity measures (Schwarz and Provaznik, 2006) as well as with high-dimensional deformations and point similarity measures (Schwarz et al., 2007).

2. Whole-brain automated morphometric methods

Analysis of brain morphology using neuroimaging data is an important area of research in neuroscience. At first volumetric approaches based on manual delineation of regions of interest (ROI) were used, later followed by several computational approaches. These were designed to overcome limitations of volumetry that is labor intensive, i.e. limits the number of subjects in a study, requires a prior anatomical hypothesis for region selection, is prone to errors that arise from subjectivity of boundaries detection, i.e. limits reliability and inter-center comparability of the results. The methods of computational neuroanatomy are widely used now; the data on their individual strengths and limitations from direct comparisons are, however, scarce (Schwarz and Kasperek, 2011).

The first implementations of computational neuroanatomic approaches are methods for voxel- and deformation-based morphometry (Ashburner and Friston, 2000; Ashburner et al., 1998), see Figure 13 for their basic diagrams.

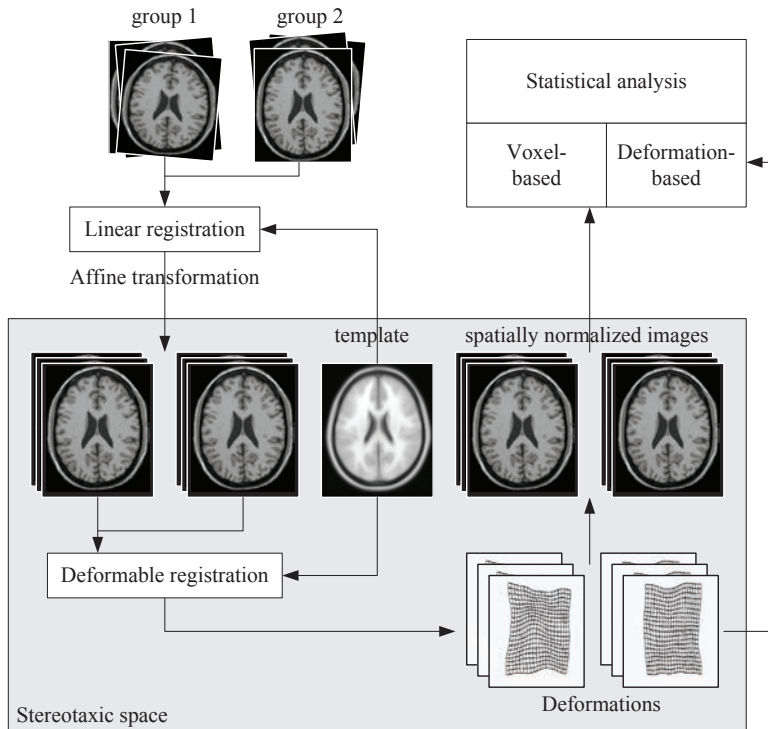


Figure 13. Morphometry methods in computational neuroanatomy involve image registration to match subjects' anatomies with a standard atlas brain. This makes it possible to compare data across different subjects in a standard stereotaxic space. Brain images are aligned by linear transformations and the fit is further improved by subsequent deformable registration. The resulting deformations are used themselves in a following analysis or they are used to spatially normalize the images which are then entered into an analysis of regionally specific differences. (Schwarz, 2005)

Voxel-based morphometry (VBM) is based on the assumption that after the removal of general shape differences during image registration, local misregistrations remain resulting in between-subject differences in local brain tissue content. Usually, the brain intensity image is segmented into different brain tissue compartments which are then analyzed separately. These local differences in tissue content are then explained by a disease effect. Besides tissue segmentation and spatial normalization, VBM algorithms usually contain also a step referred to as modulation, in which normalized tissue maps are scaled by the macroscopic deformations to preserve local volumes. The VBM approach has been validated several times – corresponding findings are obtained using both VBM and ROI-based volume calculations (Giuliani et al., 2005; Gong et al., 2005; Keller et al., 2002), VBM is able to detect focal anatomical lesions (Mehta et al., 2003). However, the idea of VBM is also criticized for its proneness to errors and false positive results due to imprecise and possibly erroneous image registrations (Bookstein, 2001). For example, group differences of cingulate gyrus observed with VBM are not detected using ROI-based volumetry in (Corbo et al., 2005), where false positive findings, which resulted from cingulate gyrus shape differences, are reported. Experimental validation of the modulation step is provided in (Radua et al., 2014) – the effects of modulation on the efficacy to detect cortical thinning are assessed. Surprisingly, the modulation step in the VBM pipeline is shown to be associated to a decrease of the sensitivity to detect abnormalities. Findings from this study suggest the use of unmodulated

VBM to detect mesoscopic (i.e. between microscopic and macroscopic) abnormalities such as cortical thinning.

The magnitude of voxel size changes during the registration process is encoded in the relevant deformations or displacement fields. Their analysis is the core principle of deformation-based morphometry (DBM). It is able to detect changes in brain shape and volume irrespective of the brain compartment in which they occur, in contrast to VBM. The term “deformation-based morphometry” is used for the first time by (Ashburner et al., 1998) to describe a method for detecting global shape changes among the brains of different populations. In general, DBM approaches differ in the registration method used, mainly in terms of the spatial deformation model. In the initial works (Ashburner and Friston, 2000; Ashburner et al., 1998), smooth parametric transforms with low-frequency sine basis functions are used. Therefore it is not possible to encode all anatomical variability, including subtle differences, into the spatial transforms (“low-resolution DBM”). A complex description of brain morphology has been possible since methods for high-resolution deformable registration were introduced (“high-resolution DBM”). These methods include spatial deformation models based on high-dimensional parametric transforms (Xie and Farin, 2001) or models inspired by similarity to continuum mechanics (Csernansky et al., 2002). DBM approach is also compared to traditional ROI-based volume calculations and yields corresponding results (Gaser et al., 2001).

There are several ways of statistical analysis of deformations, among them a univariate analysis applied to Jacobian determinants, which represent the factors by which the deformation expands or shrinks volumes at the respective voxels. The analysis of Jacobian determinants allows for the detection of local volume changes in the brain. In short, DBM analyzes how much the volume of voxels changed during subject image registration to the template image, in contrast to VBM which focuses on the residual image variability after its transformation. The finer the image transformation, the higher resolution of the deformation field, the more anatomical information is encoded in the deformation field, and the smaller the residual differences in tissue content. The high-resolution DBM could, therefore, encode local anatomical changes; moreover, it focuses on changes in spatial arrangement of images, not on the residual misregistrations, and, therefore, high-resolution DBM could overcome VBM limitations.

The application of high-resolution DBM in (Schwarz et al., 2007) is developed with the deformable registration method based on multimodal point similarity measures and the spatial deformation model allowing for large deformations while preserving the topology of the images, see chapter 2.1. It is able to register brain images with submillimeter precision on synthetic deformations. Such precision can provide high spatial resolution to detect local changes of brain morphology, not only overall changes of brain shape. Indeed, indirect comparison of results obtained using VBM² and the high-resolution DBM method shows that DBM is able to detect changes in first-episode schizophrenia (Schwarz et al., 2007) that are analogous to those detected with VBM in (Kasperek et al., 2007). That is, high-resolution DBM can detect changes on the similar spatial scale that VBM can.

The utility of mass-univariate approaches is questioned in the literature – the issues of sensitivity or the ability to correctly characterize inherently multivariate brain morphology

² VBM implemented in Statistical Parametric Mapping (SPM) framework: (<http://www.fil.ion.ucl.ac.uk/spm/>).

are raised in (Davatzikos, 2004; Friston and Ashburner, 2004) and it is proposed that multivariate techniques may provide more valid information about brain morphology.

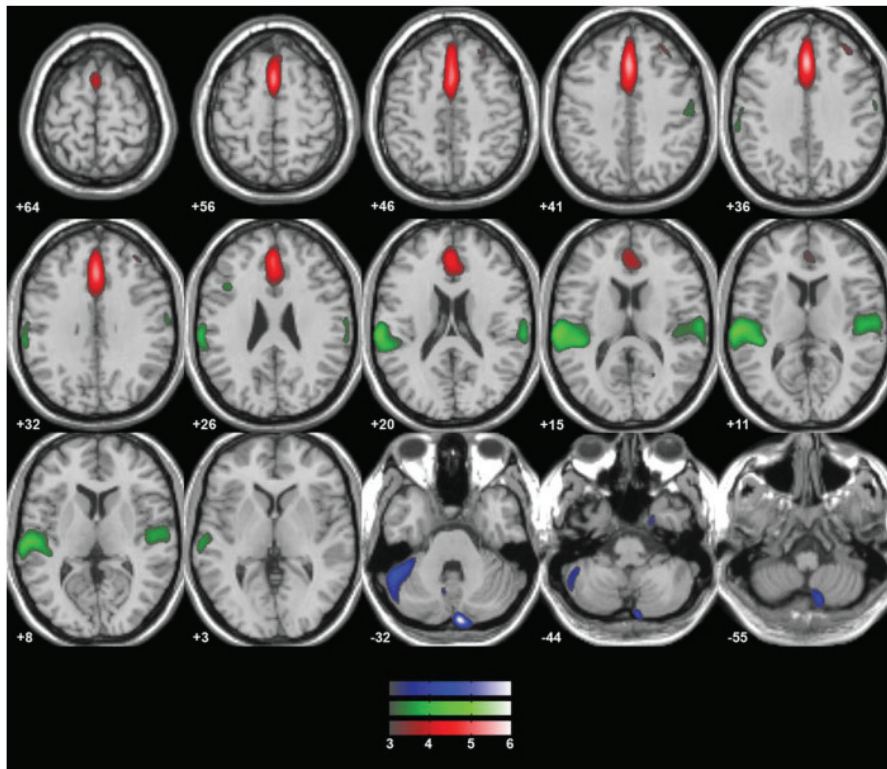


Figure 14. Gray matter volume reduction in first-episode schizophrenia - SBM results. Overlay of the three significantly different components, where first-episode schizophrenia subjects have smaller gray matter volume. Each spatial component was reshaped to the matrix with the same dimension as that of the input images, normalized to unit variance and thresholded by $Z = 3$ to display only those voxels that are maximally linked with a particular component. (Kašpárek et al., 2009)

Independent Component Analysis for morphological brain imaging data is used for the first time in (Xu et al., 2009), as a technique called “Source-based Morphometry” (SBM). In patients with chronic schizophrenia, the technique is more powerful than the VBM univariate approach in the identification of gray matter (GM) changes. The method is based on finding of independent patterns in GM images and consequent statistical analysis based on the comparison of the expression of the patterns in individual groups. Although SBM is also dealing with the groups of voxels, the nature of the method is quite different from the cluster-level analysis in VBM. SBM groups voxels with similar pattern of variance – resulting in several “components”. Then, the magnitude of expression of individual components in every subject is given (component value) and the statistical analysis is performed based on the comparisons of component values for all components extracted. This approach leads to significant reduction of the severity of multiple comparisons correction, and, more importantly, uses information about the whole patterns of brain morphology, not only about individual voxels. In contrast, cluster-level VBM deals with spatially interconnected groups

of voxels that survived an arbitrary “cluster-defining” threshold. The significance value of individual voxels in VBM is dependent on the general linear model, therefore, it is noise-dependent and high variability may lead to the failure of a voxel to reach significance. This is not the case of SBM, which is based on ICA that deals only with the structure of variance in the data. Taken together, multivariate techniques, such as SBM, may be superior to mass-univariate methods using either voxel or cluster level of inference. The improved performance of SBM over mass-univariate voxel-wise analysis of GM volume is replicated in (Kašpárek et al., 2009) with a dataset containing first-episode schizophrenia patients and healthy controls. The authors detect gray matter reduction in the medial prefrontal, neocortical temporal and cerebellar areas using SBM, see Figure 14, whereas no changes are detected with the use of VBM. Thus, SBM is reported as a suitable method for characterization of the patterns of change at the beginning of the illness in schizophrenia subjects.

2.1. Quantitative comparison of DBM and VBM

The aim of the simulation study (Schwarz and Kaspárek, 2011) was direct comparison of high-resolution DBM with widely used VBM analysis. Two sets of spatial deformations were generated: (i) simulations of normal anatomical variability and (ii) simulations of local volume changes at particular stereotactic coordinates. The nonlinear spatial transformations, which represent normal anatomical variability, were computed in the model by natural neighbor scattered data interpolation from random forces pointed in 294 locations in the volume delimited by a binary head mask. Randomness of the simulator consisted in directions of the forces, magnitudes of the forces, locations of the forces and in leaving out a portion of the forces. A single subject MRI anatomical template from Simulated Brain Database³ was then warped using those deformations to generate 50 3-D MR brain images. In addition, 20 images contained three volume expansions of different extent in three exactly defined locations, together with the simulated normal anatomical variability. The extent and shape of the volume expansions in each image were randomized to simulate the variability of volume changes in pathological processes. Quantitative parameters of simulated expansions are given in Table 2. The other 30 images were generated with the use of deformations which contain only the simulated normal anatomical variability. Displacement vectors in all 50 deformations reached maximum absolute values of about 5 mm.

The simulation results reported in (Schwarz and Kaspárek, 2011) showed superior performance of DBM that was able to detect all simulated local tissue expansions with very high precision – with the smallest simulated volume expansion at the scale of 600 mm³. VBM was not able to detect any of the three expansions - it was able to uncover tissue density change in near vicinity of the largest expansion – at the scale of 4000 mm³. This displacement, see Figure 15, was not affected by the amount of smoothing performed during VBM – similar displacement was found for both 6 and 12 mm FWHM Gaussian kernels. Moreover, one would rather expect large clusters that cover the simulated abnormality, together with many false positive voxels in the neighborhood, but not displacement of the results away from the simulation, if this shift is due to the smoothing of images. On the other hand, the smoothing is essential for VBM method, both conceptually and practically: it is necessary for intersubject comparisons; zero smoothing prevented detection of changes even at non-significant thresholds.

³ The data from the Simulated Brain Database (SBD) are used by the neuroimaging community to evaluate the performance of various image analysis methods: <http://brainweb.bic.mni.mcgill.ca/brainweb/>

Table 2. Quantitative parameters of simulated expansions. Volume of the simulated expansions was computed from the results of the statistical analysis performed on simulated deformations. Due to the variability introduced into these deformations, different statistical thresholds defined by T, p and FDR provide different volume sizes (based on the power to detect certain effect size given the variability of the data). Exp1-3: Expansion 1-3; det(J): mean; max are the mean and maximal relative volume enlargement in significant voxels. (Schwarz and Kasperek, 2011)

	$T < -4.8263$ (FDR 1%)		$T < -4.2414$ (FDR 5%)		$T < -3.5051$ ($p < 0.1\%$)	
	[mm ³]	det(J): mean; max	[mm ³]	det(J): mean; max	[mm ³]	det(J): mean; max
Exp1	3656	1.7202; 8.3393	4339	1.6663; 8.3393	5538	1.5282; 8.3393
Exp2	883	1.5767; 8.0928	1028	1.5239; 8.0928	1284	1.4557; 8.0928
Exp3	620	1.4227; 7.6176	801	1.3672; 7.6176	1192	1.2939; 7.6176

This displacement of the results obtained using VBM is of critical importance for the validity of evidence for neuroanatomical changes in neuropsychiatric disorders. For example, in schizophrenia research there is high variability of the spatial localization of gray matter changes reported in individual VBM studies (Honea et al., 2005), with relatively small overlap of the spatial maps (Ellison-Wright et al., 2008). Usually, this is interpreted in the light of neurobiological heterogeneity of the disorder. It seems likely that at least a part of this variability is due to the VBM imprecision. The power of VBM is another issue – even a study with large sample size (400 subjects) failed to find any changes in local gray matter volume in schizophrenia – due to large variability in the data (Meda et al., 2008).

The simulated volume changes were not uniform in every subject. They differed in size and shape, which we think is more similar to real volume changes, where the pathological process affects every individual differently. Although DBM results overlapped very well with the simulated tissue changes, they tended to cover larger area of brain outside the simulation. This might be due to the smoothing effect during the registration step that was necessary in some cases to assure diffeomorphicity of resulting deformations.

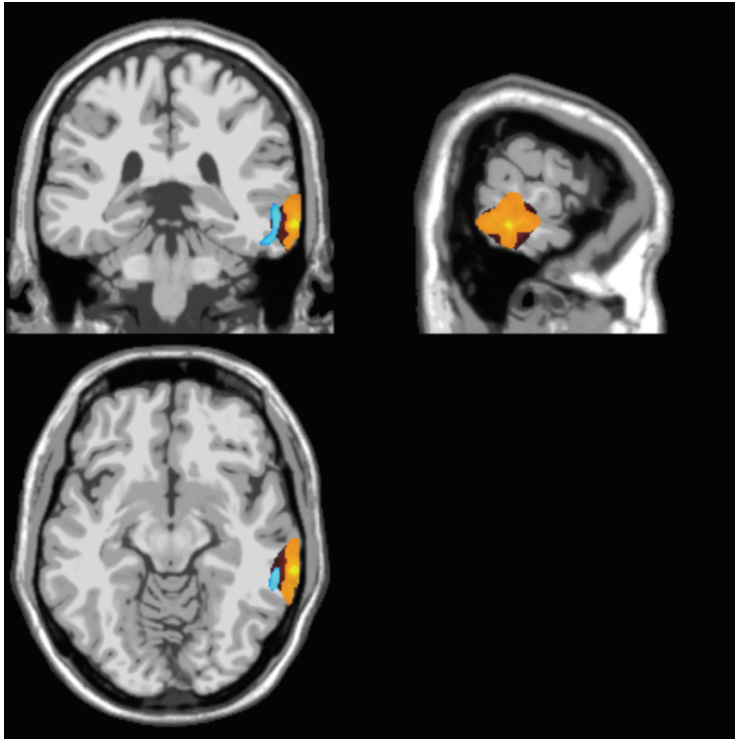


Figure 15. Spatial relationship between the region of the largest simulated local volume expansion and the regions detected by VBM and DBM. Simulated expansion region (orange) and the regions detected using DBM (red) and VBM (blue).

The poor performance of VBM, especially in the case of detection of subtle local changes, may be caused by the preprocessing steps: a substantial portion of variability is removed with nonlinear registration of the images to the template as well as with Gaussian smoothing of the binary tissue segments. In contrast, when using DBM, one tries to make all variability encoded in the deformation fields. Thus, no trade-off between removing variability with registration and detecting variability itself is necessary.

Several advantages of DBM are reported in (Schwarz and Kasperek, 2011): (i) the analyzed parameter (change of local volume) has a clear biological meaning. On the other hand, in VBM the meaning of tissue density multiplied by local volume change (determinant of Jacobian modulated tissue images), usually interpreted as “tissue volume” or “tissue density” is much less evident; (ii) the changes are always detected in the context of whole brain morphology described by high-resolution deformation fields; (iii) the localization of the changes is evident from their position within the brain. There is no risk of mirror changes or the question of what tissue is affected. Today, most VBM studies analyze only one tissue - usually gray matter (GM). However, when no information is provided about the corresponding changes in white matter (WM) and cerebrospinal fluid (CSF), it is not possible to draw clear conclusions; (iv) as suggested by the simulation, it seems that DBM could have higher spatial precision and higher sensitivity to detect subtle local volume changes.

References

- Alterovitz R, Goldberg K, Kurhanewicz J, Pouliot J, Hsu IC. 2004. Image registration for prostate MR spectroscopy using modeling and optimization of force and stiffness parameters. *Conf. Proc. Annu. Int. Conf. IEEE Eng. Med. Biol. Soc. IEEE Eng. Med. Biol. Soc. Conf.* 3, 1722–1725. doi:10.1109/IEMBS.2004.1403517
- Ashburner J, Friston KJ. 1999. Nonlinear spatial normalization using basis functions. *Hum. Brain Mapp.* 7, 254–266.
- Ashburner J, Friston KJ. 2000. Voxel-Based Morphometry—The Methods. *NeuroImage* 11, 805 – 821. doi:DOI: 10.1006/nimg.2000.0582
- Ashburner J, Hutton C, Frackowiak R, Johnsrude I, Price C, Friston K. 1998. Identifying global anatomical differences: Deformation-based morphometry. *Hum. Brain Mapp.* 6, 348–357. doi:10.1002/(SICI)1097-0193(1998)6:5/6<348::AID-HBM4>3.0.CO;2-P
- Bookstein FL. 2001. “Voxel-based morphometry” should not be used with imperfectly registered images. *NeuroImage* 14, 1454–1462. doi:10.1006/nimg.2001.0770
- Bro-Nielsen M, Gramkow C. 1996. Fast Fluid Registration of medical images, in: Höhne, K., Kikinis, R. (Eds.), *Visualization in Biomedical Computing, Lecture Notes in Computer Science*. Springer Berlin Heidelberg, pp. 265–276.
- Buzug TM, Weese J, Fassnacht C, Lorenz C. 1997. Elastic matching based on motion vector fields obtained with a histogram based similarity measure for DSA-image correction, in: *Computer Assisted Radiology and Surgery*. pp. 139–144.
- Capek M, Mroz L, Wegenkittl R. 2001. Robust and fast medical registration of 3D-multi-modality data sets.
- Chen H, Varshney PK. 2003. Mutual information-based CT-MR brain image registration using generalized partial volume joint histogram estimation. *Med. Imaging IEEE Trans. On* 22, 1111–1119.
- Christensen GE, Johnson HJ. 2001. Consistent image registration. *Med. Imaging IEEE Trans. On* 20, 568–582.
- Christensen GE, Rabbitt RD, Miller MI. 1996. Deformable templates using large deformation kinematics. *IEEE Trans. Image Process.* 5, 1435–1447. doi:10.1109/83.536892
- Collins DL, Holmes CJ, Peters TM, Evans AC. 1995. Automatic 3-D model-based neuroanatomical segmentation. *Hum. Brain Mapp.* 3, 190–208. doi:10.1002/hbm.460030304
- Collins DL, Neelin P, Peters TM, Evans AC. 1994. Automatic 3D intersubject registration of MR volumetric data in standardized Talairach space. *J. Comput. Assist. Tomogr.* 18, 192–205.
- Corbo V, Clément MH, Armony JL, Pruessner JC, Brunet A. 2005. Size versus shape differences: contrasting voxel-based and volumetric analyses of the anterior cingulate cortex in individuals with acute posttraumatic stress disorder. *Biol. Psychiatry* 58, 119–124. doi:10.1016/j.biopsych.2005.02.032
- Csernansky JG, Wang L, Jones D, Rastogi-Cruz D, Posener JA, Heydebrand G, Miller JP, Miller MI. 2002. Hippocampal deformities in schizophrenia characterized by high dimensional brain mapping. *Am. J. Psychiatry* 159, 2000–2006.
- Davatzikos C. 2004. Why voxel-based morphometric analysis should be used with great caution when characterizing group differences. *NeuroImage* 23, 17–20. doi:10.1016/j.neuroimage.2004.05.010
- Ding L, Goshtasby A, Satter M. 2001. Volume image registration by template matching. *Image Vis. Comput.* 19, 821–832. doi:10.1016/S0262-8856(00)00101-3

- Downie TR, Silverman BW. 2001. A wavelet mixture approach to the estimation of image deformation functions. *Sankhya Ser. B* 63, 181 – 198.
- Ellison-Wright I, Glahn DC, Laird AR, Thelen SM, Bullmore E. 2008. The Anatomy of First-Episode and Chronic Schizophrenia: An Anatomical Likelihood Estimation Meta-Analysis. *Am. J. Psychiatry* 165, 1015–1023. doi:10.1176/appi.ajp.2008.07101562
- Ferrant M, Nabavi A, Macq B, Jolesz FA, Kikinis R, Warfield SK. 2001. Registration of 3-D intraoperative MR images of the brain using a finite-element biomechanical model. *IEEE Trans. Med. Imaging* 20, 1384–1397. doi:10.1109/42.974933
- Ferrant M, Warfield S, Guttman CG, Mulkern R, Jolesz F, Kikinis R. 1999. 3D Image Matching Using a Finite Element Based Elastic Deformation Model, in: Taylor, C., Colchester, A. (Eds.), *Medical Image Computing and Computer-Assisted Intervention – MICCAI’99, Lecture Notes in Computer Science*. Springer Berlin Heidelberg, pp. 202–209.
- Fornefett M, Rohr K, Stiehl HS. 2001. Radial basis functions with compact support for elastic registration of medical images. *Image Vis. Comput.* 19, 87–96. doi:10.1016/S0262-8856(00)00057-3
- Friston KJ, Ashburner J. 2004. Generative and recognition models for neuroanatomy. *NeuroImage* 23, 21–24. doi:10.1016/j.neuroimage.2004.04.021
- Gaser C, Nenadic I, Buchsbaum BR, Hazlett EA, Buchsbaum MS. 2001. Deformation-based morphometry and its relation to conventional volumetry of brain lateral ventricles in MRI. *NeuroImage* 13, 1140–1145. doi:10.1006/nimg.2001.0771
- Gholipour A, Kehtarnavaz N, Briggs R, Devous M, Gopinath K. 2007. Brain Functional Localization: A Survey of Image Registration Techniques. *Med. Imaging IEEE Trans.* On 26, 427 –451. doi:10.1109/TMI.2007.892508
- Giuliani NR, Calhoun VD, Pearlson GD, Francis A, Buchanan RW. 2005. Voxel-based morphometry versus region of interest: a comparison of two methods for analyzing gray matter differences in schizophrenia. *Schizophr. Res.* 74, 135–147. doi:10.1016/j.schres.2004.08.019
- Gong QY, Sluming V, Mayes A, Keller S, Barrick T, Cezayirli E, Roberts N. 2005. Voxel-based morphometry and stereology provide convergent evidence of the importance of medial prefrontal cortex for fluid intelligence in healthy adults. *NeuroImage* 25, 1175–1186. doi:10.1016/j.neuroimage.2004.12.044
- Gramkow C, Bro-Nielsen M, Frydrych M, Parkkinen J, Visa A. 1997. Comparison of three filters in the solution of the Navier-Stokes equation in registration, in: *10th Scandinavian Conference on Image Analysis (SCIA)*. pp. 785–802.
- Guimond A, Roche A, Ayache N, Meunier J. 2001. Three-dimensional multimodal brain warping using the demons algorithm and adaptive intensity corrections. *Med. Imaging IEEE Trans.* On 20, 58–69.
- Hata N, Nabavi A, Wells WM, Warfield SK, Kikinis R, Black PM, Jolesz FA. 2000. Three-dimensional optical flow method for measurement of volumetric brain deformation from intraoperative MR images. *J. Comput. Assist. Tomogr.* 24, 531–538.
- Hermosillo G, Chefid’Hotel C, Faugeras O. 2002. Variational Methods for Multimodal Image Matching. *Int. J. Comput. Vis.* 50, 329–343. doi:10.1023/A:1020830525823
- Hoge WS, Mitsouras D, Rybicki FJ, Mulkern RV, Westin C. 2003. Registration of Multi-Dimensional Image Data via Sub-Pixel Resolution Phase Correlation, in: *In: Proceedings of IEEE International Conference on Image Processing (ICIP-03)*. pp. 707–710.
- Honea R, Crow TJ, Passingham D, Mackay CE. 2005. Regional deficits in brain volume in schizophrenia: a meta-analysis of voxel-based morphometry studies. *Am. J. Psychiatry* 162, 2233–2245.
- Ibáñez L. Insight Software Consortium, 2003. The ITK software guide. Kitware, [Clifton Park, N.Y.].

- Karaçalı B, Davatzikos C. 2003. Topology Preservation and Regularity in Estimated Deformation Fields, in: Taylor, C., Noble, J.A. (Eds.), *Information Processing in Medical Imaging*, Lecture Notes in Computer Science. Springer Berlin Heidelberg, pp. 426–437.
- Kašpárek T, Mareček R, Schwarz D, Prikryl R, Vaníček J, Mikl M, Češková E. 2009. Source-based morphometry of gray matter volume in men with first-episode schizophrenia. *Hum. Brain Mapp.* NA–NA. doi:10.1002/hbm.20865
- Kaspárek T, Prikryl R, Mikl M, Schwarz D, Ceskova E, Krupa P. 2007. Prefrontal but not temporal grey matter changes in males with first-episode schizophrenia. *Prog. Neuropsychopharmacol. Biol. Psychiatry* 31, 151 – 157. doi:DOI: 10.1016/j.pnpbp.2006.08.011
- Keller SS, Mackay CE, Barrick TR, Wieshmann UC, Howard MA, Roberts N. 2002. Voxel-based morphometric comparison of hippocampal and extrahippocampal abnormalities in patients with left and right hippocampal atrophy. *NeuroImage* 16, 23–31. doi:10.1006/nimg.2001.1072
- Kostelec PJ, Weaver JB, Healy DM. 1998. Multiresolution elastic image registration. *Med. Phys.* 25, 1593–1604.
- Kubecka L, Jan J. 2004. Registration of bimodal retinal images - improving modifications. *Conf. Proc. Annu. Int. Conf. IEEE Eng. Med. Biol. Soc. IEEE Eng. Med. Biol. Soc. Conf.* 3, 1695–1698. doi:10.1109/IEMBS.2004.1403510
- Maes F. 1998. Segmentation and registration of multimodal medical images: from theory, implementation and validation to a useful tool in clinical practice, Ph.D. thesis. ed. Catholic University of Lueven, Lueven, Belgium.
- Maes F, Collignon A, Vandermeulen D, Marchal G, Suetens P. 1997. Multimodality image registration by maximization of mutual information. *Med. Imaging IEEE Trans. On* 16, 187–198.
- Maes F, Vandermeulen D, Suetens P. 1999. Comparative evaluation of multiresolution optimization strategies for multimodality image registration by maximization of mutual information. *Med. Image Anal.* 3, 373–386.
- Maintz JA, Meijering EH, Viergever MA. 1998. General multimodal elastic registration based on mutual information, in: *Medical Imaging'98. International Society for Optics and Photonics*, pp. 144–154.
- Maintz JBA, Viergever MA. 1998. A survey of medical image registration. *Med. Image Anal.* 2, 1–36. doi:10.1016/S1361-8415(01)80026-8
- Meda SA, Giuliani NR, Calhoun VD, Jagannathan K, Schretlen DJ, Pulver A, Cascella N, Keshavan M, Kates W, Buchanan R, Sharma T, Pearlson GD. 2008. A large scale (N=400) investigation of gray matter differences in schizophrenia using optimized voxel-based morphometry. *Schizophr. Res.* 101, 95–105. doi:10.1016/j.schres.2008.02.007
- Mehta S, Grabowski TJ, Trivedi Y, Damasio H. 2003. Evaluation of voxel-based morphometry for focal lesion detection in individuals. *NeuroImage* 20, 1438–1454.
- Modersitzki J. 2004. *Numerical methods for image registration, Numerical mathematics and scientific computation.* Oxford University Press, Oxford ; New York.
- Pauchard Y, Smith M, Mintchev M. 2004. Modeling susceptibility difference artifacts produced by metallic implants in magnetic resonance imaging with point-based thin-plate spline image registration. *Conf. Proc. Annu. Int. Conf. IEEE Eng. Med. Biol. Soc. IEEE Eng. Med. Biol. Soc. Conf.* 3, 1766–1769. doi:10.1109/IEMBS.2004.1403529
- Peckar W, Schnörr C, Rohr K, Stiehl HS, Spetzger U. 1998. Linear and Incremental Estimation of Elastic Deformations in Medical Registration Using Prescribed Displacements. *Mach. Graph. Vis.* 7, 807–829.

- Pelizzari CA, Chen GT, Spelbring DR, Weichselbaum RR, Chen CT. 1989. Accurate three-dimensional registration of CT, PET, and/or MR images of the brain. *J. Comput. Assist. Tomogr.* 13, 20–26.
- Pluim JP, Maintz JB, Viergever M. 2001. Mutual information matching in multiresolution contexts. *Image Vis. Comput.* 19, 45–52. doi:10.1016/S0262-8856(00)00054-8
- Radua J, Canales-Rodríguez EJ, Pomarol-Clotet E, Salvador R. 2014. Validity of modulation and optimal settings for advanced voxel-based morphometry. *NeuroImage* 86, 81–90. doi:10.1016/j.neuroimage.2013.07.084
- Rogelj P. 2003. Non-rigid registration of multi-modality images, Ph.D. thesis. ed. University of Ljubljana, Ljubljana, Slovenia.
- Rogelj P, Kovačič S. 2004. Spatial deformation models for non-rigid image registration, in: *Proceedings of 9th Computer Vision Winter Workshop. Presented at the CVWW'04*, pp. 79–88.
- Rogelj P, Kovačič S. 2006. Symmetric image registration. *Med. Image Anal.* 10, 484–493.
- Rogelj P, Kovačič S, Gee JC. 2003. Point similarity measures for non-rigid registration of multi-modal data. *Comput Vis Image Underst* 92, 112–140. doi:10.1016/S1077-3142(03)00116-4
- Rohlfing T, Maurer Jr CR, Bluemke DA, Jacobs MA. 2003. Volume-preserving nonrigid registration of MR breast images using free-form deformation with an incompressibility constraint. *Med. Imaging IEEE Trans. On* 22, 730–741.
- Rohr K. 2000. Elastic Registration of Multimodal Medical Images: A Survey. *Künstl. Intell.* 2000, 11–17.
- Rueckert D, Sonoda LI, Hayes C, Hill DL, Leach MO, Hawkes DJ. 1999. Nonrigid registration using free-form deformations: application to breast MR images. *Med. Imaging IEEE Trans. On* 18, 712–721.
- Ruprecht D, Müller H. 1993. Free Form Deformation with Scattered Data Interpolation Methods, in: Farin, G., Noltemeier, H., Hagen, H., Knödel, W. (Eds.), *Geometric Modelling, Computing Supplementum*. Springer Vienna, pp. 267–281.
- Schnabel JA, Tanner C, Castellano-Smith AD, Degenhard A, Leach MO, Hose DR, Hill DL, Hawkes DJ. 2003. Validation of nonrigid image registration using finite-element methods: application to breast MR images. *Med. Imaging IEEE Trans. On* 22, 238–247.
- Schwarz D. 2005. Automated morphometry of MRI brain images with the use of deformable registration, PhD thesis. ed. Brno University of Technology, Brno.
- Schwarz D, Kasperek T. 2011. Comparison of two methods for automatic brain morphometry analysis. *Radioengineering* 20, 996–1001.
- Schwarz D, Kasperek T, Provazník I, Jarkovsky J. 2007. A Deformable Registration Method for Automated Morphometry of MRI Brain Images in Neuropsychiatric Research. *Med. Imaging IEEE Trans. On* 26, 452–461. doi:10.1109/TMI.2007.892512
- Schwarz D, Provazník I. 2002a. Segmentation and visualization of medical images with the use of multimodal registration, in: *Analysis of Biomedical Signals and Images. Presented at the 16th International EURASIP Conference BIOSIGNAL 2002*, Brno, pp. 362–364.
- Schwarz D, Provazník I. 2002b. Rigid and elastic registration of multimodal volume images in medicine, in: *IFMBE Proceedings. Presented at the 2nd European Medical and Biological Engineering Conference EMBE'02*, Vienna, pp. 604–605.
- Schwarz D, Provazník I. 2006. Low-dimensional Multimodal Deformable Registration of MRI Brain Images in Stereotaxic Space. *Eur. J. Biomed. Inform.* 2006, n.pag.

- Shen D, Moffat S, Resnick SM, Davatzikos C. 2002. Measuring Size and Shape of the Hippocampus in MR Images Using a Deformable Shape Model. *NeuroImage* 15, 422–434. doi:10.1006/nimg.2001.0987
- Talairach J. 1988. Co-planar stereotaxic atlas of the human brain: 3-dimensional proportional system: an approach to cerebral imaging. Georg Thieme, Stuttgart ; New York.
- Tang S, Jiang T. 2004. Fast nonrigid medical image registration by fluid model, in: *Proceedings of 6th Asian Conference on Computer Vision*. Presented at the ACCV 2004, Jeju, Korea, pp. 914–919.
- Thirion JP. 1996. Non-rigid matching using demons. *IEEE Comput. Soc. Press*, pp. 245–251. doi:10.1109/CVPR.1996.517081
- Thirion JP. 1998. Image matching as a diffusion process: an analogy with Maxwell’s demons. *Med. Image Anal.* 2, 243–260. doi:10.1016/S1361-8415(98)80022-4
- Tsao J. 2003. Interpolation artifacts in multimodality image registration based on maximization of mutual information. *IEEE Trans. Med. Imaging* 22, 854–864. doi:10.1109/TMI.2003.815077
- Unser M, Thevenaz P. 2000. Optimization of mutual information for multiresolution image registration. *IEEE Trans. Image Process.* 9, 2083–2099. doi:10.1109/83.887976
- Viola P, Wells WM. 1995. Alignment by maximization of mutual information. *IEEE Comput. Soc. Press*, pp. 16–23. doi:10.1109/ICCV.1995.466930
- Wachowiak MP, Wang X, Fenster A, Peters TM. 2004. Compact support radial basis functions for soft tissue deformation, in: *Biomedical Imaging: Nano to Macro, 2004. IEEE International Symposium on. IEEE*, pp. 1259–1262.
- Wollny G, Kruggel F. 2002. Computational cost of nonrigid registration algorithms based on fluid dynamics [mri time series application]. *Med. Imaging IEEE Trans. On* 21, 946–952.
- Woods RP, Dapretto M, Sicotte NL, Toga AW, Mazziotta JC. 1999. Creation and use of a Talairach-compatible atlas for accurate, automated, nonlinear intersubject registration, and analysis of functional imaging data. *Hum. Brain Mapp.* 8, 73–79.
- Xie Z, Farin G. 2001. Deformation with hierarchical b-splines. *Math. Methods Curves Surf. Oslo 2000* 545–554.
- Xu L, Groth KM, Pearlson G, Schretlen DJ, Calhoun VD. 2009. Source-based morphometry: The use of independent component analysis to identify gray matter differences with application to schizophrenia. *Hum. Brain Mapp.* 30, 711–724. doi:10.1002/hbm.20540
- Zitová B, Flusser J. 2003. Image registration methods: a survey. *Image Vis. Comput.* 21, 977–1000.

Dynamic contrast-enhanced MRI and ultrasound using blind deconvolution

Radovan Jiřík¹, Karel Souček^{2,3}, Martin Mézl^{4,5}, Michal Bartoš^{4,6}, Eva Dražanová¹,
František Dráň⁹, Lucie Grossová^{1,4}, Jiří Kratochvíla⁴, Ondřej Macíček⁴, Kim Nylund⁷,
Aleš Hampl^{3,9}, Odd Helge Gilja^{7,10}, Torfinn Taxt⁸, Zenon Starčuk jr.¹

¹*Institute of Scientific Instruments, AS CR, Brno; e-mail: jirik@isibrno.cz*

²*Dept. of Cytokinetics, Institute of Biophysics, AS CR, Brno*

³*Center of Biomolecular and Cellular Engineering, ICRC, Brno*

⁴*Dept. of Biomedical Engineering, Brno Univ. of Technology, Brno*

⁵*Center of Biomedical Engineering, ICRC, Brno*

⁶*Institute of Information Theory and Automation of the ASCR, Praha*

⁷*Haukeland University Hospital, Bergen, Norway*

⁸*Dept. of Biomedicine, University of Bergen, Norway*

⁹*Faculty of Medicine, Masaryk Univ., Brno*

¹⁰*Dept. of Clinical Medicine, University of Bergen, Bergen, Norway*

Abstract

This paper is focused on quantitative perfusion analysis using MRI and ultrasound. In both MRI and ultrasound, most approaches allow estimation of rate constants (K^{trans} , k_{ep} for MRI) and indices (AUC, TTP) that are only related to the physiological perfusion parameters of a tissue (e.g. blood flow, vessel permeability) but do not allow their absolute quantification. Recent methods for quantification of these physiological perfusion parameters are shortly reviewed. The main problem of these methods is estimation of the arterial input function (AIF). This paper summarizes and extends the current blind-deconvolution approaches to AIF estimation. The feasibility of these methods is shown on a small preclinical study using both MRI and ultrasound.

Key words

Perfusion, pharmacokinetic modeling, blind deconvolution, MRI, ultrasonography

1. Introduction

Perfusion imaging is an important diagnostic tool used mostly in oncology, neurology and cardiology, to assess the perfusion status of the tissue on a capillary level, e.g. assessment of angiogenesis, ischemic regions and inflammation. This work is focused on clinical and preclinical dynamic contrast-enhanced magnetic resonance and ultrasound imaging (DCE-MRI and DCE-US). In these methods, contrast-agent concentration time curves are derived from the acquired image sequences for each tissue region of interest (ROI, e.g. the whole tumor or each pixel/voxel). In quantitative DCE-MRI, these tissue curves are approximated by a pharmacokinetic model. The ultimate goal is to estimate the physiological perfusion parameters, such as blood flow, F_b , blood volume, v_b , vessel permeability-surface product, PS , and extravascular-extracellular space volume, v_e .

In DCE-MRI, the usual pharmacokinetic models are the Tofts and extended Tofts models (Sourbron and Buckley, 2012). The estimated perfusion parameters included in these models are the forward transfer constant between blood plasma and the extravascular extracellular (interstitial) space, K^{trans} , the efflux rate constant from the extravascular extracellular space to

blood, k_{ep} , and v_e (and also v_b for extended Tofts model). To estimate the complete perfusion-parameter set, including F_b and PS , advanced pharmacokinetic models (Sourbron and Buckley, 2012) need to be applied, such as the adiabatic approximation to the tissue homogeneity model (ATH), the distributed-capillary adiabatic tissue homogeneity model (DCATH) or the two-compartment exchange model (2CXM). However, the parameter estimation of these advanced pharmacokinetic models requires a high signal-to-noise ratio (SNR) in order not to be ill-conditioned. Furthermore, application of these models assumes a high temporal resolution of the acquisition to capture the vascular-distribution phase of the bolus. These are the main reasons why most quantitative DCE-MRI studies are based on the Tofts or extended Tofts models. This is especially the case for preclinical DCE-MRI, where, to our knowledge, the only use of such models have been (Keunen et al., 2011, Taxt et al., 2012).

The pharmacokinetic models of quantitative DCE-MRI include the arterial input function (AIF). It is the contrast-agent concentration curve in the arterial input of the tissue ROI. It is one of the major factors causing poor reproducibility of DCE-MRI. There are several approaches to determination of the AIF. The first approach is to derive it from the acquired image sequence as the contrast-agent concentration curve in a large artery (Pike et al., 2009). However, such measurement is distorted by flow artifacts, partial volume effect, saturation and T2* effect. The second approach is to use a population-based AIF (Loveless et al., 2012). This ignores the differences in the vascular tree between different subjects and depends on the AIF acquisition methods used for creation of these population-based "standards". The third (preclinical) approach is based on analysis of arterial blood samples taken during the bolus application (Verhoye et al., 2002) which is a fairly invasive method and suffers from the AIF-shape dispersion (blood samples are taken far from the arterial input of the tissue ROI). The fourth approach is based on a reference tissue (e.g. muscle) (Heisen et al., 2010). The AIF is estimated from the tissue curve in this reference tissue and the presumably known perfusion parameters. This approach has been shown for the Tofts model. For the advanced pharmacokinetic model, the complete set of perfusion parameters would have to be known which is not very realistic. Another approach to estimation of the AIF is based on blind deconvolution. Imposing prior knowledge (e.g. the pharmacokinetic model, positivity of the contrast-agent concentration curves, model of the AIF) and a suitable initial estimation scheme, it is possible to estimate simultaneously the perfusion parameters and the AIF from the measured tissue ROI contrast-agent concentration curves. This allows estimation a unique AIF for each DCE-MRI acquisition. This approach has been introduced in clinical DCE-MRI as multi-channel deconvolution (multiple tissue ROI signals processed simultaneously) in (Riabkov and Di Bella, 2002, Fluckiger et al., 2009) for the Tofts model and extended to an advanced pharmacokinetic model (ATH) and to the preclinical application group (Keunen et al., 2011, Taxt et al., 2012).

In DCE-US, quantitative perfusion analysis using a similar concept of pharmacokinetic modeling including the AIF has been introduced recently in (Mezl et al., 2010, Gauthier et al., 2012). The AIF is measured in a big artery feeding the analyzed tissue. The pharmacokinetic model is simplified by the intravascular character of ultrasound contrast agents. It allows estimation of v_b and F_b . However, measurement of the AIF in a blood pool is difficult due to contrast-agent-related attenuation, blood-velocity dependence of the backscattered signal and low spatial resolution of ultrasound images. To avoid this, we have recently proposed a blind-deconvolution approach called bolus & burst (Jirik et al., 2013, Jirik et al., 2012). It is based on the following acquisition protocol. Following a contrast-agent bolus application, low-energy imaging pulses are used to record the "bolus-phase" sequence. In the later wash-out phase of the bolus, when the tracer concentration decays

rather slowly, a burst pulse sequence is applied to destroy the contrast agent in the imaging plane. The following "replenishment phase" is recorded using low-energy imaging pulses. The assumption of slow decay of the AIF and of zero initial contrast-agent concentration in this replenishment phase are important prior information for blind deconvolution.

This paper presents new extensions to the blind-deconvolution methods of AIF estimation and shows their feasibility on a small preclinical study (group of 4 mice, subcutaneous tumor) for both DCE-MRI and DCE-US. In the DCE-MRI part, our previous blind-deconvolution AIF estimation method (Keunen et al., 2011, Tact et al., 2012), based on the ATH pharmacokinetic model and a nonparametric AIF, is extended to a model-based AIF. A new AIF model for preclinical DCE-MRI is introduced. In the DCE-US part, our blind-deconvolution AIF estimation method bolus & burst (Jirik et al., 2013, Jirik et al., 2012) is extended from clinical to preclinical application by using the same new AIF model as in the MRI part. Another extension of the DCE-US algorithm is generation of perfusion-parameter maps instead of estimation of perfusion-parameters for single large ROIs.

2. Blind deconvolution in DCE-MRI

The tissue contrast-agent concentration time curve is modeled using a pharmacokinetic model as a convolution of the AIF and the tissue residue function (TRF), multiplied by blood flow. The TRF is modeled using the ATH model (Sourbron and Buckley, 2012). For AIF, the standard model is a bi-exponential function (Heilmann et al., 2007). While it is probably sufficient for the Tofts and extended Tofts pharmacokinetic models, it is not suitable for advanced pharmacokinetic models, such as the ATH. The need for finer time-domain sampling and more perfusion parameters included in these advanced models require a more flexible AIF model. The new AIF model is a sum of three gamma variate functions:

$$AIF(t) = t^\beta \sum_{n=1}^3 \alpha_n e^{-\tau_n t}, \quad (1)$$

where t is time, β , α_n and τ_n are model parameters. Approximation of the contrast-agent concentration time curves by the pharmacokinetic model is formulated as a minimization problem. The criterion function is a sum of the least-squares differences between the contrast-agent concentration time curve and its convolutional model for all channels. The channels represent the tissue regions from which the contrast-agent concentration time curves are extracted (10 channels are used here). Hence, the blind-deconvolution algorithm results in estimates of the TRF parameters (perfusion parameters) of each channel and of the AIF parameters (common for all channels). An alternating optimization scheme is applied where each iteration (10 iterations are used here) consists of two steps: 1. update of the TRF while the AIF is fixed to the actual estimate, 2. update of the AIF while the TRF is fixed to the actual estimate. The substeps are realized using the Active-Set optimization algorithm as implemented in the Matlab Optimization toolbox (MathWorks, USA), function `fmincon`.

The resulting AIF estimate is scaled so that perfusion analysis of the contrast-agent concentration curve of a reference tissue (here spinal muscle) results in a known literature-based value of v_e+v_p (here 0.13 ml/g tissue). The sum v_e+v_p corresponds to the area under the curve of the TRF (Keunen et al., 2011). The estimated AIF is then subsequently used in the pixel-by-pixel non-blind deconvolution of the whole image sequence to calculate the perfusion-parameter maps.

3. Blind deconvolution in DCE-US

The pharmacokinetic model used in DCE-US is the same as for DCE-MRI, except for the TRF, which is an exponential function with the time constant being F_b / v_b (Jirik et al., 2013). The blind-deconvolution algorithm is formulated as minimization of the least-mean-square difference between the measured and modeled signals. One channel (i.e. signal from one ROI) is used. The criterion function is a sum of the bolus and replenishment terms. In the replenishment part, the application of burst is modeled as zero initial condition at the time instant of the replenishment-phase start. Scaling of the AIF estimate is done with respect to a region of the highest area under the curve. The AIF is scaled so that v_b of this region is 1 ml/g, assuming it represents an intravascular region. The estimated AIF is then subsequently used in the region-by-region (each region is 20x20 pixels) non-blind deconvolution of the whole image sequence to calculate the perfusion-parameter maps.

4. Experimental data and results

4.1. Experimental Data

Animals: The proposed AIF estimation method is evaluated on preclinical data. The test recordings (approved by the National Animal Research Authority) was done on a BALB/c mouse with murine colon tumor cells CT26.WT (ATCC, CRL-2638) subcutaneously implanted into the left flank (1×10^6 cells in HC Matrigel). Four mice were examined in the following way. Each mouse underwent three DCE-MRI examinations, two with a standard low-molecular-weight contrast agent (Magnevist, Bayer HealthCare Pharmaceuticals, Berlin, Germany) and one with a high-molecular-weight contrast agent (GadoSpin P, Miltenyi Biotec, Bergisch Gladbach, Germany). In addition, two of these mice underwent a DCE-US examination (contrast agent: Vevo MicroMarker, Visualsonics, Toronto, Canada).

MRI acquisition: One axial slice through the tumor middle was imaged. The mice were anesthetized with Isofluran, O_2 and monitored continuously for respiratory rate and body temperature. A 9.4T BioSpin (Bruker Biospin MRI, Ettlingen, Germany) scanner was used with the following acquisition parameters: 2D FLASH sequence with TR/TE 14/2.5 ms, flip angle 25 deg., image matrix 128x96 pixels, slice thickness 1~mm, sampling interval 1.05~s, acquisition time 13 min. Before the bolus administration, 15 images were recorded with TR = 14, 30, 50, 100, 250, 500 ms to convert the dynamic image sequence to the contrast-agent concentration. Anatomical images were recorded using the RARE sequence (T2-weighted and T1-weighted pre- and post-contrast).

US acquisition: A Vevo 2100 (Visualsonics, Toronto, Canada) scanner was used with the MS250 probe, nonlinear contrast imaging mode, acquisition time 2~min 40~s. To convert image intensity within the ROI to the concentration of the contrast agent, standard preprocessing is applied, including linearization of video data (conversion to envelope data) and square operation, see e.g. (Rognin et al., 2008).

4.2. Results

The resulting DCE-MRI perfusion-parameter maps were spatially consistent and in the expected range. They showed the expected characteristics according to assumed histological composition. There was a clear distinction between the tumor rim and the fibro-necrotic centre. On the PS map the permeability decreased towards the centre. The F_b map was also with a good correlation with the expected malignant lesion features and other parametric images (not shown), the highest values on the outer lesion margin corresponded to the presence of the feeding and draining vessels.

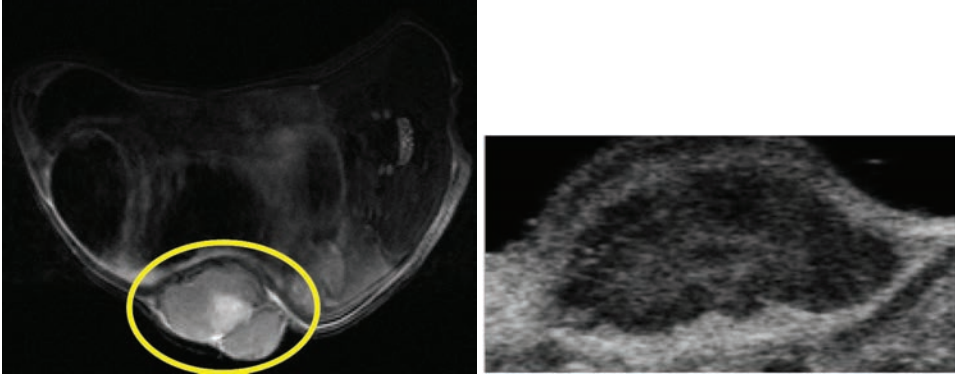


Figure 1. Left: Example of T2-weighted anatomical image of the tumor, mouse 1, examination 2. Ellipse denotes the tumor cross-section. Upper region is a cross-section of spine and spinal muscles. Right: Example of B-mode ultrasound image of tumor, mouse 1.

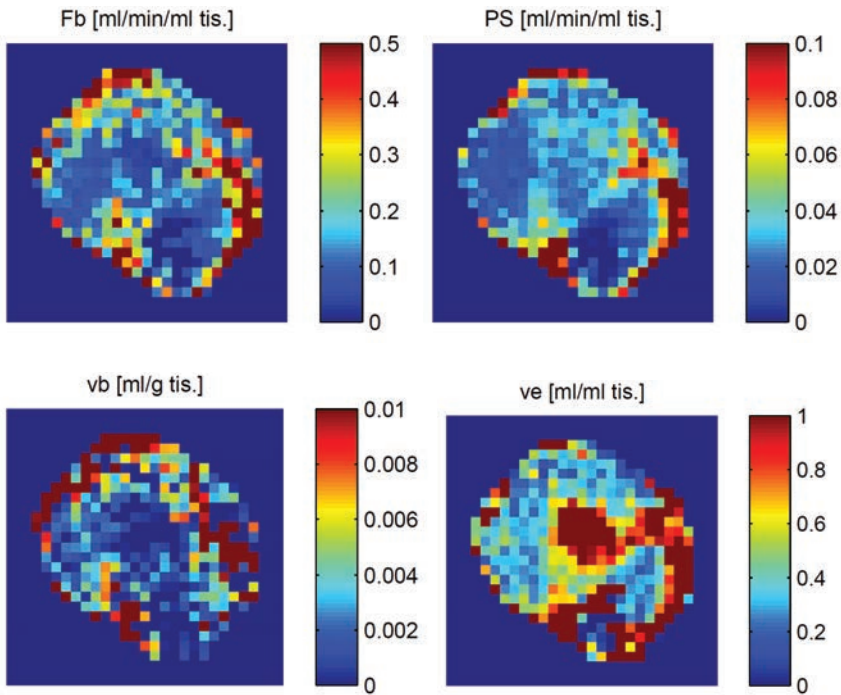


Figure 2. Examples of estimated DCE-MRI perfusion-parameter maps within the tumor, mouse 1, examination 2.

The box plots in Figure 3 show the perfusion-parameter estimates in manually drawn tumor ROIs. The central mark is the median, the edges of the box are the 25th and 75th percentiles, the whiskers extend to the most extreme data points not considered outliers. In line with theoretical expectations the estimates of F_b were independent of the contrast agent's molecular weight, while the estimates of PS showed lower values for the high-molecular-weight contrast agent. Reproducibility of the perfusion-parameter estimates (deduced from the comparison of the two Magnevist examinations) was fairly

good (except for PS , mouse M04). Intersubject comparison indicates a fairly homogeneous animal group, except for mouse M04 with a clearly more perfused tumor giving consistently higher F_b and PS than for other animals.

The perfusion-parameter maps from DCE-US (Figure 4) corresponded well with the DCE-MRI maps. Also the scale of blood flow was the same (box plots in Figure 3).

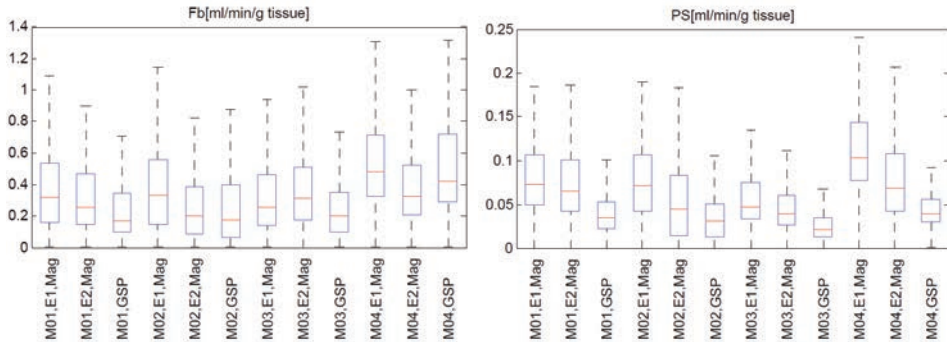


Figure 3. Box plots of F_b and PS within a the tumor region. M0X – animal number, EX – examination number, Mag – Magnevist, GSP – GadoSpin P

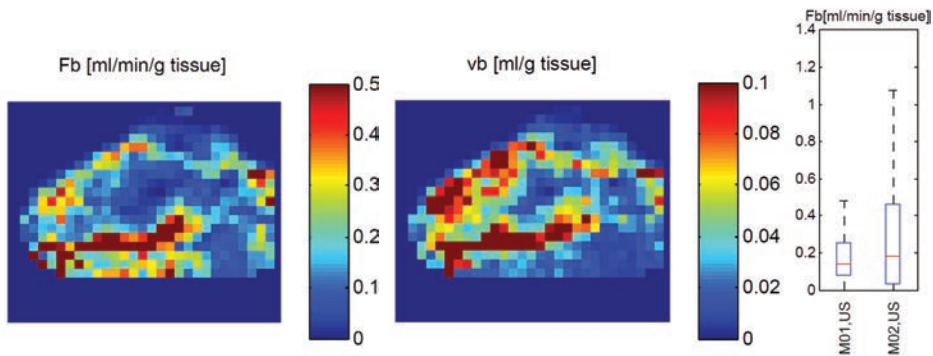


Figure 4. Example of estimated DCE-US perfusion-parameter maps within the tumor, mouse and box plots of F_b within the tumor region. M0X denotes animal number.

5. Conclusions

Estimation of AIF using blind deconvolution is feasible, as was shown for DCE-MRI on clinical (Riabkov and Di Bella, 2002, Fluckiger et al., 2009) and preclinical data (Keunen et al., 2011, Taxt et al., 2012). The presented extension of blind-deconvolution DCE-MRI introduces the combination of an advanced pharmacokinetic model (ATH) and a new small-animal AIF model. This allows robust estimation of F_b and PS in addition to the Tofts-model's perfusion parameters. To evaluate the DCE-MRI method we have proposed a new way of indirect validation by using two contrast agents of different molecular weight. The presented extension of our DCE-US method towards pixel-wise perfusion analysis and combination with the new AIF model seems to give consistent results, when compared to

DCE-MRI estimates of F_b . A thorough validation will be needed to assess the achievable accuracy and reproducibility of the methods.

References

- Fluckiger J U, Schabel M C, DiBella EVR. 2009. Model-Based Blind Estimation of Kinetic Parameters in Dynamic Contrast Enhanced (DCE)-MRI. *Magnetic Resonance in Medicine* 62(6): 1477-1486.
- Gauthier M, Tabarout F, Leguenerny I, et al. 2012. Assessment of quantitative perfusion parameters by dynamic contrast-enhanced sonography using a deconvolution method: an in vitro and in vivo study. *Journal of Ultrasound in Medicine* 31(4): 595-608.
- Heilmann M, Walczak C, Vautier J, et al. 2007. Simultaneous dynamic T1 and T2* measurement for AIF assessment combined with DCE MRI in a mouse tumor model. *Magma* 20(4): 193-203.
- Heisen M, Fan X, Buurman J, Romeny, BTH. 2010. Effects of reference tissue AIF derived from low temporal resolution DCE-MRI data on pharmacokinetic parameter estimation. In: ISMRM-ESMRMB Joint Annual Meeting 2010. Sweden, Stockholm, p. 4802.
- Jirik R, Nylund K, Gilja OH, et al. 2013. Ultrasound perfusion analysis combining bolus-tracking and burst-replenishment. *IEEE Transactions on Ultrasonics, Ferroelectrics, and Frequency Control* 60(2): 310-319.
- Jirik R, Nylund K, Taxt T, et al. 2012. Parametric Ultrasound Perfusion Analysis Combining Bolus Tracking and Replenishment. In *Proceedings of the IEEE International Ultrasonics Symposium 2012*, p. 1323-1326.
- Keunen O, Johansson M, Oudin A, et al. 2011. Anti-VEGF treatment reduces blood supply and increases tumor cell invasion in glioblastoma. *Proceedings of the National Academy of Sciences of the United States of America* 108(9): 3749-3754.
- Loveless ME, Halliday J, Liess C, et al. 2012. A quantitative comparison of the influence of individual versus population-derived vascular input functions on dynamic contrast enhanced-MRI in small animals. *Magnetic Resonance in Medicine* 67(1): 226-236.
- Mezl M, Jirik R, Harabis V, Kolar R. 2010. Quantitative ultrasound perfusion analysis in vitro. In *Proceedings of Biosignal 2010: Analysis of Biomedical Signals and Images* 20: 279-283.
- Pike MM, Stoops CN, Langford CP, et al. 2009. High-resolution longitudinal assessment of flow and permeability in mouse glioma vasculature: Sequential small molecule and SPIO dynamic contrast agent MRI. *Magnetic Resonance in Medicine*, 61(3): 615-625.
- Riabkov DY, Di Bella EVR. 2002. Estimation of kinetic parameters without input functions: Analysis of three methods for multichannel blind identification. *IEEE Transactions on Biomedical Engineering* 49(11): 1318-1327.
- Rognin NG, Frinking P, Costa M, Arditi M. 2008. In-vivo perfusion quantification by contrast ultrasound: Validation of the use of linearized video data vs. raw RF data. In *IEEE Proceedings of Ultrasonics Symposium*.
- Sourbron SP, Buckley DL. 2012. Tracer kinetic modelling in MRI: estimating perfusion and capillary permeability. *Physics in Medicine and Biology* 57(2): R1-R33.
- Taxt T, Jirik R, Rygh CB, et al. 2012. Single-Channel Blind Estimation of Arterial Input Function and Tissue Impulse Response in DCE-MRI. *IEEE Transactions on Biomedical Engineering* 59(4):1012-1021.
- Verhoye M, van der Sanden BPJ, Rijken PFJW, et al. 2002. Assessment of the neovascular permeability in glioma xenografts by dynamic T1 MRI with Gadomer-17. *Magnetic Resonance in Medicine* 47(2):305-313.

Introduction to diffusion-weighted imaging

René C.W. Mandl

*Brain Center Rudolf Magnus, Department of Psychiatry, University Medical Center Utrecht,
Utrecht, The Netherlands
Center for Neuropsychiatric Schizophrenia Research (CNSR), Copenhagen University
Hospital, Psychiatric Center Glostrup, Denmark
e-mail: rmandl@umcutrecht.nl*

Abstract

Diffusion-weighted imaging (DWI) is a magnetic resonance imaging technique that allows us to non-invasively probe the microstructure of brain tissue. Using DWI we can obtain directional information of the fiber bundles in the brain that form the brain's white matter. It is believed that these white matter fiber bundles are implicated in various neurological and psychiatric diseases and nowadays DWI is extensively used to study the human brain *in vivo* at different levels ranging from local (at a voxel level) microstructural properties of brain tissue to the level of complete networks (network analysis). In this lecture the basics of diffusion-weighted imaging will be presented as well as various applications and future directions.

Key words

Magnetic resonance imaging, diffusion-weighted human brain, fiber tracking, white matter, networks

1. Introduction

Complex brain functions do not reside in only one particular gray matter brain region but they rather emerge from the dynamic flow of information between different (spatially distinct) gray matter regions (Catani and Ffytche, 2005; Mesulam, 2005). These regions are interconnected over long distances by white matter fiber bundles (Figure 1a) forming large-scale neural networks for which normal inter-regional communication is a prerequisite for proper functioning. Therefore these white matter fiber bundles are considered to be the information highways of the brain. These white matter fiber bundles consist of large numbers of axons running in parallel, each surrounded by a myelin sheath. An axon is the part of a neuron that transports the outgoing signals from the cell body to other neurons (see Figure 1b). Myelin is a fatty insulating substance (responsible for the tissue's white color) and the presence of the myelin sheath increases signal transport efficiency over the axon in terms of the energy needed as well as in speed. Magnetic resonance imaging (MRI) methods such as diffusion-weighted MRI (DWI) in combination with fiber tracking algorithms allow us to reconstruct these white matter fiber bundles and to study several aspects of these bundles *in vivo*.

Diffusion-weighted magnetic resonance imaging (DWI) (Le Bihan and Breton, 1985; Le Bihan et al., 2001) has become a standard tool that allows us to probe the diffusion profile of water molecules at the level of voxels (volume elements). Diffusion (also known as Brownian motion) is the process of thermally driven displacement of the water molecules due to collisions with their surrounding molecules. From the diffusion profile of the water molecules we can infer characteristics of the microstructure of the underlying tissue that cannot be measured in a direct way. DWI has proven to be particularly useful to study the

human brain's white matter because in white matter the diffusion profile of the water molecules provides directional information of the underlying white matter fiber bundles (Chenevert et al., 1990; Doran et al., 1990). In white matter fiber bundles water molecules diffuse more easily in the direction parallel to the fiber bundle than in the perpendicular direction (Figure 2b). As a consequence the diffusion profile of the water molecules is anisotropic (i.e. not the same in each direction). Information about the shape of the diffusion profile can be obtained by measuring the level of diffusion in different directions (Basser, 1995).

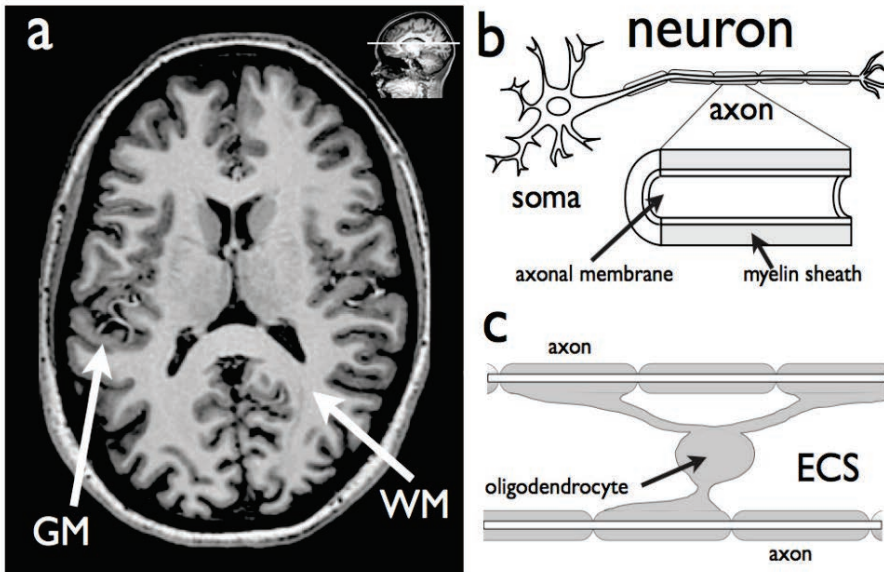


Figure 1. a) A T1-weighted MRI scan of the human brain showing locations of gray matter (GM) and white matter (WM). b) The gray matter mostly consists of the soma of the neurons (b) while the white matter is formed by the myelinated axons. c) In the central nervous system, the insulating myelin sheath is created by a type of glial cells called oligodendrocytes. One oligodendrocyte may produce more than one myelin sheath segment serving several different axons. Water molecules are present in both the intracellular space (that is the space within the neurons and glial cells) and the extracellular space (ECS).

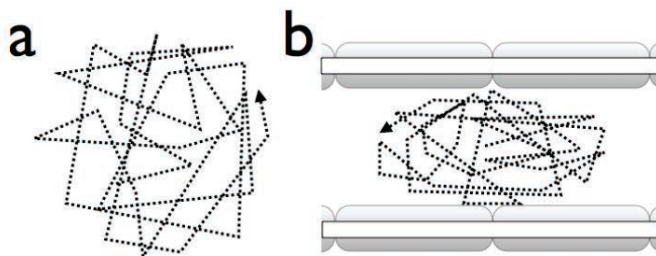


Figure 2. a) The diffusion path of a single water molecule in case of unrestricted diffusion. The diffusion profile of all the water molecules combined will be isotropic as there are no structuring elements to shape the diffusion profile. b) The diffusion path of a single water molecule in white matter. The hindering of the diffusion of the water molecules by the axons results in an anisotropic diffusion profile, pointing in the direction of the fiber bundle.

DWI “only” provides local information (in a voxel) on the directionality of the underlying white matter fiber bundle. This may be more than sufficient if, for example, one wants to compare groups (patients versus healthy persons) to search for focal aberrations. A popular method for this type of studies is tract-based spatial statistics (TBSS) (Smith et al., 2006), which utilizes so-called skeletons for white matter to perform a group comparison of diffusion profiles per skeleton voxel.

For other types of analysis, however, it is necessary to reconstruct whole fiber bundles.

Various fiber tracking algorithms exist that can be used to integrate this local directionality information to reconstruct whole white matter fiber bundles. Fiber tracking algorithms combine the directional information of the fiber bundles provided by DWI at voxel level in order to reconstruct entire white matter fiber tracts. One should bear in mind that with DWI information is obtained at the level of voxels (typically $2.0 \times 2.0 \times 2.0$ mm), which contains millions of axons (with diameters ranging from 0.2 - 20 μ m) (Kandel, 2000) and therefore only information of large fiber bundles and not of individual axons is obtained.

Fiber tracking algorithms can roughly be divided into two classes, namely deterministic fiber tracking algorithms and probabilistic fiber tracking algorithms. The former provide the actual paths between regions (if they are connected) while the latter merely provide the probability for two given regions of being connected. See (Jones, 2008) for a discussion on the possibilities and limitations of both types of algorithms.

Figure 3 shows an example of whole brain fiber tract reconstruction with the original (and still widely used) deterministic fiber assignment by continuous tracking (FACT) algorithm (Mori et al., 1999).

One could define a starting region and an end region and then try to use deterministic fiber tracking to reconstruct fiber tracts between these regions. However, it turns out that (due to measurement noise inherent to DWI) a better way is to combine an exhaustive search approach with a number of selection regions of interest (ROIs). Here, first all possible tracts in the brain are reconstructed after which only those tracts are considered that actually penetrate the selection ROIs. Depending on its purpose, the selection ROIs can be defined in the deep white matter or in gray matter. The former is typically used if one wants to delineate one of the well-known large white matter bundles (for example the arcuate fasciculus, uncinate fasciculus or genu of the corpus callosum).

The latter is often used in network analyses where automatically segmented gray matter regions are used as nodes to compute the connectivity matrix. Note however that using gray matter selection ROIs is more complicated because information on fiber directionality is typically low in the vicinity of gray matter.

DWI is widely used to study various neurological and psychiatric diseases. For example in schizophrenia, where Bleuler – when defining schizophrenia more than a century ago – already hypothesized that the integration of information was implicated (Bleuler, 1911).

Indeed, based on a large body of research a general picture emerges that the white matter is implicated in schizophrenia, predominantly the fiber bundles connecting the prefrontal and temporal brain regions (Shenton et al., 2010). However, linking these frequently reported disease-related differences in the diffusion profile to mechanisms responsible for the disease is not straightforward because various different tissue characteristics (e.g. axonal diameter, axonal density, level of myelination) influence the size and shape of the diffusion profile (Norris, 2001; Beaulieu, 2002).

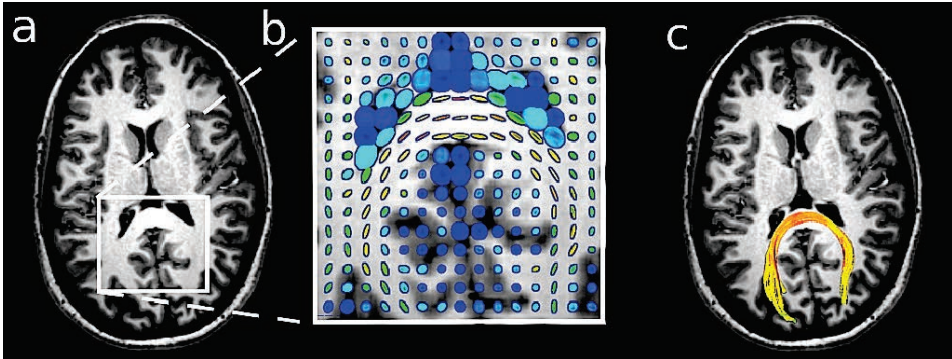


Figure 3. Fiber tracking example using the deterministic FACT algorithm. a) Region for which the diffusion profiles – here modeled with tensors -- are shown in b). The tensors in white matter point in the direction of the fiber bundle (in this case the splenium of the corpus callosum). c) Using the directional information from the tensors b) the tracts from the splenium of the corpus callosum were reconstructed.

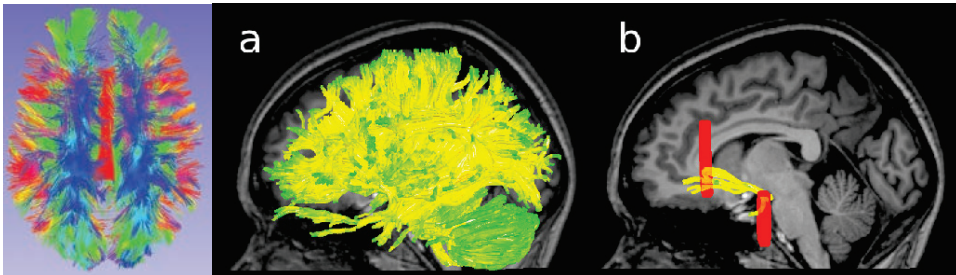


Figure 4: Left: Example of exhaustive search (transverse view). The algorithm starts to tracing in each white matter voxel in the white matter of the brain. Here the reconstructed fibers are color-coded based on their general direction (red: left-right, green: posterior-anterior, blue: inferior-superior). Note that because diffusion is symmetric no distinction can be made between for instance left-to-right and right-to-left. Right: example of usage of selection ROIs to select the left uncinate fasciculus.

a) shows again all reconstructed fibers (sagittal view). Two selection ROIs are shown in red in b) to select the all the reconstructed fiber tracts that penetrate both ROIs. Together these selected tracts form the reconstructed left uncinate fasciculus.

Although DWI provides us with unique directional information on the microstructure of brain tissue it cannot be used to extract information from the different tissue compartments (e.g. intracellular, extracellular space). The main reason is that with conventional DWI the diffusion of water molecules is measured and water is present in all tissue compartments. An interesting technique – especially using ultra high field MRI (Ronen et al., 2013) – that can be used to differentiate between the different compartments is diffusion-weighted spectroscopy (DWS). With DWS the diffusion profile of different metabolites (instead of water molecules) is measured. In contrast to water, different metabolites are confined to different tissue compartments. Thus, DWS can help us, for example, to determine if differences in the microstructure frequently reported in schizophrenia (measured with conventional DWI) reflect differences in the intracellular and/or extracellular compartment. Such information is crucial to better understand the etiology of the disease.

In sum, diffusion weighted imaging, together with fiber tracking and network analysis, proved itself as an indispensable technique in today's neuroscience that provides us with a unique view on the brain's white matter fiber tracts. Moreover, it is a research field in full motion where new exciting techniques are developed that will help us to better understand the structure and functioning of the human brain.

References

- Basser PJ. 1995. Inferring microstructural features and the physiological state of tissues from diffusion-weighted images. *NMR in Biomedicine* 8(7-8): 333-344.
- Beaulieu C. 2002. The basis of anisotropic water diffusion in the nervous system – a technical review. *NMR in Biomedicine* 15(7-8): 435-455.
- Bleuler E. *Dementia Praecox or the Group of Schizophrenias*. New York: International Universities Press, 1911.
- Catani M, Ffytche DH. 2005. The rises and falls of disconnection syndromes. *Brain* 128(Pt 10):2224-2239.
- Chenevert TL, Brunberg JA, Pipe JG. 1990. Anisotropic diffusion in human white matter: demonstration with MR techniques in vivo. *Radiology* 177(2): 401-405.
- Doran M, Hajnal JV, Van Bruggen N, King MD, Young IR, Bydder GM. 1990. Normal and abnormal white matter tracts shown by MR imaging using directional diffusion weighted sequences. *Journal of Computer Assisted Tomography* 14(6): 865-873.
- Jones DK. 2008. Studying connections in the living human brain with diffusion MRI. *Cortex* 44(8): 936-952.
- Kandel ER, Schwartz JH, Jessell TM. *Principles of Neural Science* New York: McGraw-Hill, 2000. ISBN 0-8385-7701-6.
- Le Bihan D, Breton E. Imagerie de diffusion in vivo par résonance magnétique nucléaire. *Compte Rendus de l'Académie de Sciences Paris* 301: 1109-1112.
- Le Bihan D, Mangin JF, Poupon C, Clark CA, Pappata S, Molko N, Chabriat H. 2001. Diffusion tensor imaging: concepts and applications. *Journal of Magnetic Resonance Imaging* 13(4): 534-546.
- Mesulam M. 2005. Imaging connectivity in the human cerebral cortex: the next frontier? *Annals of Neurology* 57(1): 5-7.
- Mori S, Crain BJ, Chacko VP, van Zijl PC. 1999. Three-dimensional tracking of axonal projections in the brain by magnetic resonance imaging. *Annals of Neurology* 45(2): 265-269.
- Norris DG. 2001. The effects of microscopic tissue parameters on the diffusion weighted magnetic resonance imaging experiment. *NMR in Biomedicine* 14(2): 77-93.
- Ronen I, Ercan E, Webb A. 2013. Axonal and glial microstructural information obtained with diffusion-weighted magnetic resonance spectroscopy at 7T. *Frontiers in Integrative Neuroscience* 7: 13.
- Shenton ME, Whitford TJ, Kubicki M. 2010. Structural neuroimaging in schizophrenia: from methods to insights to treatments. *Dialogues in Clinical Neuroscience* 12(3): 317-332.
- Ciccarelli O, Cader MZ, Matthews PM, Behrens TE. 2006. Tract-based spatial statistics: voxelwise analysis of multi-subject diffusion data. *NeuroImage* 31(4): 1487-1505.

Computing average cortical profiles at 3 tesla

René C.W. Mandl^{1,2}, Martijn P. van den Heuvel¹, Rachel M. Brouwer¹,
Hilleke E. Hulshoff Pol¹

¹*Brain Center Rudolf Magnus, Department of Psychiatry, University Medical Center
Utrecht, Utrecht, The Netherlands*

²*Center for Neuropsychiatric Schizophrenia Research (CNSR), Copenhagen University
Hospital, Psychiatric Center Glostrup, Denmark
e-mail: rmandl@umcutrecht.nl*

Abstract

The cortex of the human brain can be divided into different layers (or lamina) based on differences in architecture/function. Extensive research conducted over the last decades showed that in particular the frontotemporal part of the cortex is implicated in psychiatric diseases, especially in schizophrenia. Numerous MRI studies using MRI scanners operating at conventional field strengths (e.g. 1.5, 3 tesla) consistently showed a disease-related thinning of the cortex in these regions but these studies could not provide any information on which of the different layers were implicated. The main reason is that at conventional field strengths SNR limitations result in an image resolution that is simply too coarse to detect the individual layers. One solution is to acquire data using ultra-high field (e.g. 7 tesla) MRI because the SNR is directly related to the main magnetic field strength. However, acquiring large datasets at ultra-high field MRI scanners is often more complex than at conventional MRI scanners. Currently we are working on new ways to combine information extracted from 3 tesla and 7 tesla data. Using a series of post-processing steps we are able to extract certain cortical information for existing large sets acquired at 3 tesla containing both patients with schizophrenia and healthy controls. A smaller dataset acquired at 7 tesla will then be used to validate/interpret apparent disease-related laminar differences found at 3 tesla.

Key words

Cortical layers, schizophrenia, human brain, MRI

1. Introduction

Many psychiatric diseases such as schizophrenia are characterized by non-focal cortical thinning of several brain regions (Garey, 2010). Analysis methods like Freesurfer (<http://surfer.nmr.mgh.harvard.edu>) can be used to study cortical thickness but they do not provide any information on which cortical layers are implicated. The main reason is that the resolution of images acquired routinely using conventional MRI field strengths (e.g., 3 tesla) is considered to be too low. One solution is to increase imaging resolution by using ultra-high field MRI (for example 7 tesla) (Zwanenburg et al., 2012; Waehnert et al., 2013). But ultra-high field MRI is usually not readily available and performing large cohort studies (needed because the effect sizes for psychiatric diseases like schizophrenia are typically very small) at 7 tesla is complicated. In this lecture I will discuss a new automatic analysis method that we recently proposed (Mandl et al., 2014), which extracts detailed cortical profile information from conventional whole brain T1-weighted scans acquired at 3 tesla and which are part of a standard scan protocol. This method exploits the fact that aberrations found in psychiatric diseases are typically non-focal in nature.

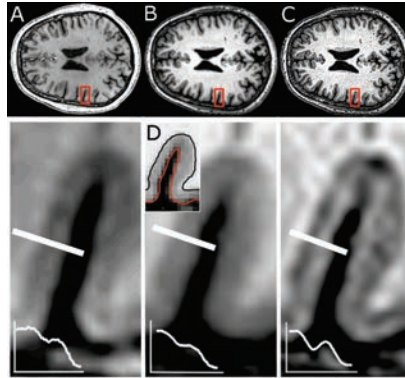


Figure 1. T1-weighted image acquired at 7T (A). T1-weighted image of same subject acquired at 3T (B). Image B after 3D deconvolution (C). White bars denote cross-sections and corresponding profiles shown in lower row. Automatic cortical delineation computed on original 3T (B) image shown in D.

2. Methods

To assess its feasibility we used the 3D FFE T1-weighted images (acquired on a 3 Tesla Philips Achieva; TR/TE 10 ms/4.6 ms; flip-angle=8°; FOV= 240x240 mm; 200 slices, 0.75 isotropic voxel size; total scan duration 602 s) from 5 healthy subjects who participated in a previous study and for which written informed consent was obtained prior to scanning.

In the first step, Freesurfer was used to automatically delineate the inner (white matter), the outer (pial) boundaries and the curvature of the cerebral cortex allowing us to measure cortical profiles at every cortex position. Next, the resolution of the original T1-weighted image was upsampled by a factor of 2 (in all 3 directions) after which parallel iterative 3D deconvolution (http://fiji.sc/Parallel_Iterative_Deconvolution) (Wiener filter preconditioned landweber method; 3 iterations; normalize PSF; anti-ringing step; divergence detection; gamma = 0) was applied. This step enhances image details but also substantially reduces signal-to-noise ratio. Then for each subject and each cortical region (assuming the same cytoarchitecture within a single region, e.g. Brodmann areas (BA)) the deconvoluted data was sampled along all cortical profiles. Next, to increase homogeneity, only profiles were selected for which the absolute curvature of the cortex was < 0.1 and the length (before normalization) deviated $< 10\%$ from the median profile length for the specific area. Finally, these selected profiles were aligned (scaling and translation) and averaged (increasing SNR again) yielding one average cortical profile per region (per subject).

3. Results

Figure 2 (left panel) shows the mean cortical profiles computed for 4 different Brodmann areas. The right panel shows the profiles (averaged over all 5 subjects) created without the application of the additional selection step (that is, all profiles found for one Brodmann area).

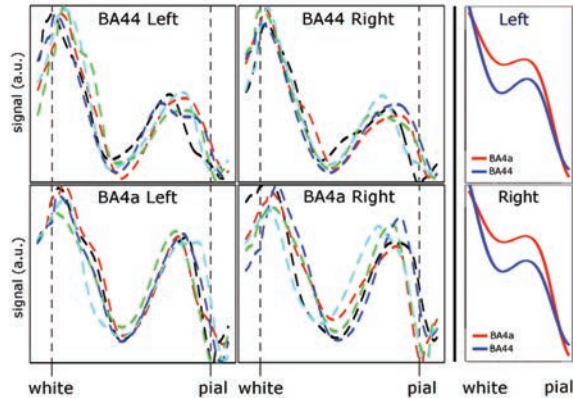


Figure 2. The average cortical profiles computed for four different Brodmann areas from five healthy subjects are shown in the left panel. Average profiles (averaged over all subjects) computed without additional selection on curvature and length are shown in the right panel.

4. Discussion

Our initial results show (left panel) that for each of the four Brodmann areas the average cortical profiles of the five subjects are in good agreement. Moreover, our results clearly show that the average profiles are more similar between homologue Brodmann areas than between different Brodmann areas (for instance, the height of the maximum near the pial surface), which indicate that this method is sensitive enough to detect interregional differences. Additional selection using curvature and profile length (left panel) results in more pronounced profiles compared to no selection (right panel) and may allow for a better detection of subtle group differences. We note that this method is not limited to T1-weighted images (as used in this example) but can be used with any type of contrast provided that accurate cortical delineation is possible. Future work includes relating the differences found between average cortical profiles of different Brodmann areas to known differences in cyto/myelo-architecture for these areas.

5. Conclusion

The results of our initial experiments suggest that this novel automatic analysis method can be used to extract detailed information on cortical configuration from existing large datasets acquired with MRI scanners operating on conventional field strengths. The application of this method is not limited to psychiatric diseases but it can also be used to study for instance cortical changes during brain development.

References

Garey L. 2010. When cortical development goes wrong: schizophrenia as a neurodevelopmental disease of microcircuits. *Journal of Anatomy* 217(4): 324-333.

Mandl RCW, van den Heuvel MP, et al. 2014. Computing average cortical profiles at 3T. *Proceedings of the International Society for Magnetic Resonance in Medicine, Milan, Italy, 10-16 May 2014.*

Wähnert M, Dinse J, Tardif C, Schäfer A, Geyer S, Bazin PL, et al. 2013. How much resolution is needed for in-vivo analysis of cortical myeloarchitecture? Proceedings of the International Society for Magnetic Resonance in Medicine. Salt Lake City, UT, USA, 20–26 April 2013.

Zwanenburg JJ, Hendrikse J, Luijten PR. 2012. Generalized multiple-layer appearance of the cerebral cortex with 3D FLAIR 7.0-T MR imaging. *Radiology* 262(3): 995-1001.

Operative neurosurgical techniques, multimodality image fusion and its application in a neuroscience programme

Ivo Říha

*Department of Neurosurgery, St. Anne's University Hospital in Brno
e-mail: ivo.riha@fnusa.cz*

Abstract

In the early 1990s, practical neurosurgery completely changed due to development and routine application of computer technology, particularly due to the boom of revolutionary development of imaging methods such as MRI, CT and digital radiographic systems. Through further processing of these acquired data, neurosurgeons are nowadays able to plan trajectories, namely for minimally invasive surgeries with tissue sampling, electrostimulation, or local destruction of defined structures as well as for open brain surgeries from craniotomy approach. Apart from functional surgeries stereotactic methods are also applied in a wide range of various pathologies. The main indications for neuroendoscopy are hydrocephalus, cysts, intraventricular tumors, and haematomas. Other non-functional surgeries are biopsies, haematoma evacuations or resection of CNS lesions. Planning of surgical interventions is performed on reconstructed slices obtained from primary axial layers using interpolation from both MRI and CT scans. Lately, imaging using both of these modalities, their subsequent registration and superposition has been applied with benefit which has brought great advantage with regard to the character of these imaging methods. Two systems have been used at Dept. of Neurosurgery, St. Anne's University Hospital in Brno for targeted interventions: Zamorano Dujovny stereotactic system with Leibinger MRI compatible open ceramic frame and BrainLab navigation system. Procedures performed with these systems cover the whole range of routine brain surgeries. A stereotactic frame system features enhanced accuracy and is intended for procedures requiring accurate targeting such as intracerebral electrode implantation (SEEG), Deep Brain Stimulation (DBS) or targeted biopsy sampling. The navigation system covers all afunctional procedures then.

Key words:

Stereotaxy, neurosurgical navigation, CNS, MRI, CT

1. Neurosurgical techniques

Decades ago, neurosurgeons tried to influence the clinical course of functional disorders, mainly Parkinson's disease or epilepsy, by inserting electrodes into various brain structures. Both destruction and stimulation techniques has been used. For the purpose of targeting X-ray ventriculography employing teleradiographic technique with positive or negative contrast administration combined with stereotactic atlases presenting brain slices in three mutually perpendicular planes (transverse, sagittal and coronal) were used. The atlases were created by means of a statistical analysis of interindividual variations. One of the first widely used atlases was the stereotactic atlas by Spiegel and Wycis (1952), Talairach – Tournoux and last but not least the most recently constructed Schaltenbrand Bailey atlas. Connective pathways bundles e.g. anterior and posterior commissures were used as reference points for the coordinate system. The calculation was laborious and protracted, and miscellaneous aids had to be used (Alexander and Maciunas, 1999).

Recently, more sophisticated methods have been elaborated that involve modern imaging modalities such as CT, MRI and digital radiographic systems. With the onset of computing techniques, the calculation has been automatized. Planning of operational interventions has been carried out on reconstructed slices obtained from primary axial slices, whether from MRI or CT (the tendency is to acquire the largest possible number of slices as thin as possible) by interpolation. Lately, imaging using both these modalities has preferably been used, followed by their registration (matching) and superposition which has brought a great advantage considering the character of both of these imaging methods. Neurosurgeons are now able to plan surgical trajectories through further processing of acquired data, namely either for minimally invasive procedures connected with tissue sampling, electrostimulation or local destruction of the defined brain structures or for open surgeries from craniotomy approach.

1.1. Frame-based stereotaxy

Before the stereotactic surgery, a stereotactic frame base is applied to the patient's head and firmly fixed to his/her cranial vault using screws with titanium tips. Figure 1 shows complete Zamorano-Dujovny frame assembly with Leibinger MRI-compatible open ceramic frame (Figure 1a) with various attachment options of the navigation system, MRI/CT contrast markers (Figure 1b), and their 3D virtual reality (Figure 1c) as a result of using stereotactic navigation software environment. The detail of a DBS microelectrode implantation system is presented in Figure 1d.

Transformation into stereotactic space, i.e., defining the zero point and directions of the individual axes of the Cartesian coordinate system corresponding to the 3D arrangement of the stereotactic frame, is carried out through MRI/CT contrast markers which are firmly attached to the navigation frame during image acquisition. Apart from the Zamorano-Dujovny stereotactic frame currently used in the author's department, other frames are also routinely used, e.g., Riechert-Munding, Brown-Roberts-Wells (BRW), Leksell and Zeppelin (Alexander and Maciunas, 1999).

Special MRI/CT contrast markers are designed to be detectable in basic T1WI MRI images as well as during CT scanning. The registration of image data acquired during the same time with markers attached is simple and is a part of the basic equipment of all types of navigation software used. A registration is a problem when the navigation data (MRI T1WI) are to be merged with CT or MRI image data acquired during another session without the use of markers, or in a non-equidistant image, an MRI image in other than axial planes, or an MRI image with no localization markers displayed (MRI T2WIs) should be used.

Registration and the subsequent MRI image correlation with Talairach–Tournoux or Schaltenbrand–Bailey atlas respectively, is also a part of the presurgical planning. It is necessary to bear in mind that any atlas is solely a statistic model and in the case of anomalous brain the registration is only an approximation.

The reason why we try to facilitate the accuracy of the navigation process together with precise target definition is the avoidance of any interference with brain vasculature. Vascular injury can result in grave surgical complication. Stereotactic planning techniques are used both in functional as well as in non functional surgeries covering wide range of pathologies. Stereotactic frame system properties facilitate system accuracy and are designed for use in surgeries requiring accurate delineation and targeting of structures, such as intracerebral electrode implantation (SEEG), Deep Brain Stimulation (DBS) or targeted biopsy sampling.

1.2. Frameless navigation

The “frameless” navigation systems became widely known in the past few years. In these navigation systems, the transformation of the coordinate system of the patient's brain or whole head, respectively, presented by MRI or CT slices is performed through a registration system, either using contrast markers, so called “fiducials”, attached to the soft tissues of the patient's head or using natural external landmarks (auricle, eye, nasal root; the so called “landmarkers”) registration. Since such registrations are relatively inaccurate, it is necessary to eliminate errors through superficial registration of randomly chosen points on the skin cover of the patient's skull. Such registration is performed on a patient whose head has already been fixed in a three-point head holder. Contemporary systems employing these principles are designed and manufactured, e.g., by Medtronic (Stealth station) and BrainLAB (Vector Vision Sky) (Figures 2a,b). Their major disadvantage is the presence of the so called “dead zones” in which registration cameras working in infrared band do not “see” the contrast points of a surgical instrument. The software supplied with all these systems is capable of planning several access trajectories and displaying axial, sagittal, coronal, perpendicular and parallel views (as related to the trajectory) based on the selected imaging modality. It is possible to apply basic segmentation algorithms and hence to obtain object contours for subsequent 3D planning. The main indication field are non functional surgeries – endoscopic surgeries for hydrocephalus, cysts, intraventricular tumors, haematomas or others like tumor biopsy, haematoma evacuation or resections of CNS lesions (Novák et al., 2004).

2. Image data acquisition

The process of neuronavigation or stereotactic surgery consists of image data acquisition from appropriate imaging modalities. In case of functional procedure MRI scan is always preferred (if not contraindicated). An additional data acquisition using a CT scanner might be performed. A facility LAN network and PACS using a standard DICOMv3 protocol is used for data transfer to the planning stations.

2.1. Image data used by default

The data sources for these systems are MRI and CT scanners. In patients primarily examined at the Imaging Modalities Department, St. Anne's University Hospital in Brno before navigated surgery or frame-based surgery a couple of image sets is acquired. Basic MRI image data, particularly 3D T1WI – with a slice thickness of 1.2 mm, 2D T2WI (FatSat) – with directly subsequent slice thickness of 2 mm, 3D TOF (arterial phase) – depending on the ROI size, mostly with a slice thickness of 0.8 mm, 2D TOF (venous phase) with directly subsequent slice thickness of 1 mm are obtained. The data set is supplemented with CT scans (directly subsequent layers thickness of 1.2 mm or 0.6 mm, respectively).

With the exception of the basic MRI data sets, i.e., T1WI and T2WI, study of brain vasculature (Time of Flight method – TOF sequence) is used as well. The TOF MRA method (MR angiography) uses spinning current transport in relation to a selectively specified layer.

2.2. Additional imaging methods

Functional magnetic resonance imaging (fMRI) is a modern imaging technique used for functional mapping of brain areas activated during specific task or stimulation. The fMRI began to evolve mainly in the last decade of the 20th century and considerably enriched the understanding of cognitive neuroscience and clinical neurophysiology. Mapping is

performed either on the basis of perfusion changes in a defined area or on the basis of blood oxygenation changes (the BOLD effect). Based on the blood oxygenation and local blood perfusion changes this method enables indirect detection of cortical regions involved in cognitive, motor or other task performed by an examined subject. This method is considered to be an additional examination prior to a neurosurgical intervention. Suitable clinical applications include speech or motor center localization, but is not limited to only (Mikl et al., 2008).

DTI (Diffusion Tensor Imaging) tractography – is an MRI scanner mapping with postprocessing application the result of which is a map of neural pathways (tracts) in the cerebral white matter. A map of the corticospinal tract during intraaxial brain tumor surgeries, when the tumor is located close to the corticospinal tract, is incorporated into the navigation system (Neuman et al., 2011).

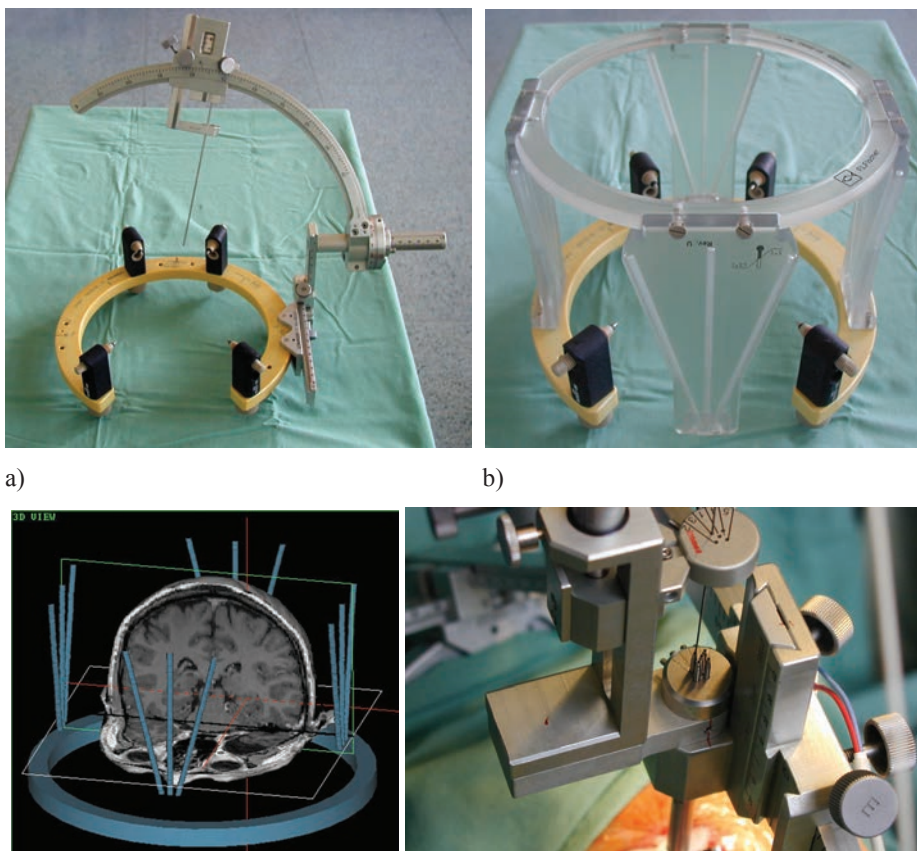


Figure 1. a) Zamrano-Dujovny stereotaxy frame setting with Leibinger MRI-compatible open ceramic frame; b) MRI/CT-contrast marker; c) the 3D virtual reality; d) the detail of a DBS microelectrode introducer.

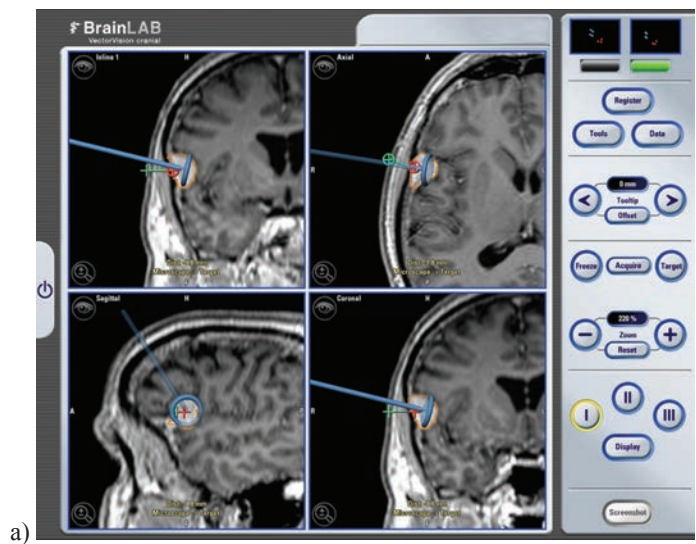


Figure 2. a) Screenshot of the BrainLAB Vector Vision Sky navigation system display; b) intraoperative use of the mentioned navigation system.

Positron emission tomography (PET) and single photon emission computed tomography (SPECT) are used for localization of intracranial targets. The use of these methods is most frequently described for stereotactic tumor biopsies. In most cases, these methods are used in conjunction with CT or MRI. PET and SPECT modalities report on the functioning of a pathological process which makes the difference from CT and MRI recording a morphological image. The disadvantage for the application of these methods in stereotaxy is their small spatial resolution.

Ultrasonography (US) has a different role in stereotactic neurosurgery as compared with other imaging methods. It is used intraoperatively as a supplementary method whereas basic information serving for target localization is usually obtained using CT or MRI. US is routinely used for position specification of tumor edges and vessels in the access pathway to them. Lately, navigated 3D ultrasound has been used.

3. Multimodal registration and subsequent image series fusions

Generally spoken image fusion is a process making possible image merging from different modalities in order to create a more comprehensive image or eventually to detect the ROI in detail. Multimodal image fusion is of particular importance because the different modalities use different physical properties of the displayed object as a primary parameter field. A computer tomograph uses a linear attenuation coefficient as a primary parameter; it is hence a single parameter field. On the contrary, magnetic resonance may work as a multiparameter field. Basic primary MRI parameters, the selection of which can be affected by the choice of RF excitation sequences and the scanning method, include proton density (PD), T1 and T2 relaxation times (T1WI and T2WI imaging – influenced by chemical bonds of water molecules), and last but not least the time of flight (TOF). Since both of these modalities work on different principles, images produced by them also have completely different predictive values regarding morphology. While CT image displays precisely bone structures or pathologies such as haematomas or tumors with affinity to vasculature, that are depicted in the CT image after contrast administration, MRI image also involves chemical changes that might precede pathology formation. Moreover, the fact that pathology is not visible in one of the images, which uses one primary parameter, does not imply that it won't be visible in the other image. Even in the case pathology is displayed in both image sets acquired from these modalities, a fusion helps to optimize the extent of an intervention with regard to the fact that countours of the pathology may differ in asdefined by different image modalities. On the contrary, some pathologies act as a diffusion process and the contours are principally unclear. Anyway, a fusion of individual image sets must be, however, preceded by exact registration, i.e., a process enabling the identification of corresponding landmarks in both acquired image data sets.

A precise registration of CT and MRI image data is also very important in the field of radiosurgery and nuclear medicine. Here, a CT image is necessary because of the calculation of therapeutic dose distribution and a MRI image is essential for exact specification of the lesion borders. For such procedures stereotactic navigation procedure accuracy with an error less than 1 mm is required.

3.1. Registration methods

A fusion of CT and MRI images must be preceded by registration of acquired image data. Currently, several algorithms based either on an image segmentation into particular objects – registration based on landmarks or contours – or on a global image similarity based on a

mutual information (MI method) are used for registration (Čapek and Krekule, 1999). Such registrations can be rigid, affinitive or flexible, according to geometric transformation used. Rigid registration preserves the geometric layout of both images; the transformation includes Euclidean operations (translation, rotation). In affinitive registrations, it is furthermore possible to perform a change in the scale or skew. General deformations in shape are performed using non-linear registrations; the use of these methods for neurosurgical interventions is currently not recognized as “lege artis”.

Image data registration methods are generally distinguished based on the following:

- a) the correspondence of landmarks
 - contrast markers, the so called fiducials, located on the skin cover of patient's calva
 - anatomical landmarks, or patient's external anatomy “landmarks” (auricle, eye, nasal root)
- b) the correspondence of countours of the particular region – image segmentation – thresholding, countour detection, techniques based on region accretion (binary erosion and dilation), active countour models (countours), and the combination thereof
- c) maximum global similarity of the image/volume – intensity methods with the use of optimization procedures (Powell, Marquardt-Levenberg, ...)

3.2. Artifacts arising from acquisition

The large amount of image artifacts influencing more or less the diagnostic information arises from the MRI and CT process physical properties. It is not always possible to eliminate it completely or at least reduce to an acceptable degree using simple methods. When performing MRI scans acquisition in the presence of conductive objects, an artifact occurs with the character resembling the absence of a signal in the location of the object and causes a non-linear shift of structures in a more distant neighbourhood. Example of such an artifact – see Figure 3: an artifact in an MRI image caused by the presence of a metal object, wironite (dental implant) in a T1W1-3D sequence – Gradient Echo (GE) due to susceptibility (Drastich, 2004). Such artifacts also influence more distant brain structures therefore causing non-linearity of position information (Říha et al., 2006).

4. Perspectives in neurosurgery

Considering the system accuracy, then in case of a frame system, only evaluation of mechanical accuracy is concerned; in case of navigation, evaluation of accuracy of the patient's head registration and the virtual 3D model of the patient's head reconstructed from tomographic MRI or CT slices are concerned. This kind of error does not include mapping errors. With the knowledge of principles of tomographic slices reconstruction of both mentioned modalities, it is possible to achieve optimum accuracy using a combination or a fusion of both images, respectively, and therefore to avoid position error which is caused by a simultaneous presence of a conductive metal object in the displayed scene during an acquisition using an MRI scanner. After the surgery, patients are observed and continuously examined, generally using an MRI scanner, on a long-term basis. This fact also enables us to apply algorithms on image data which might be morphologically changed, and we are therefore able to track the development of the pathology and/or the development after pathology removal, respectively.

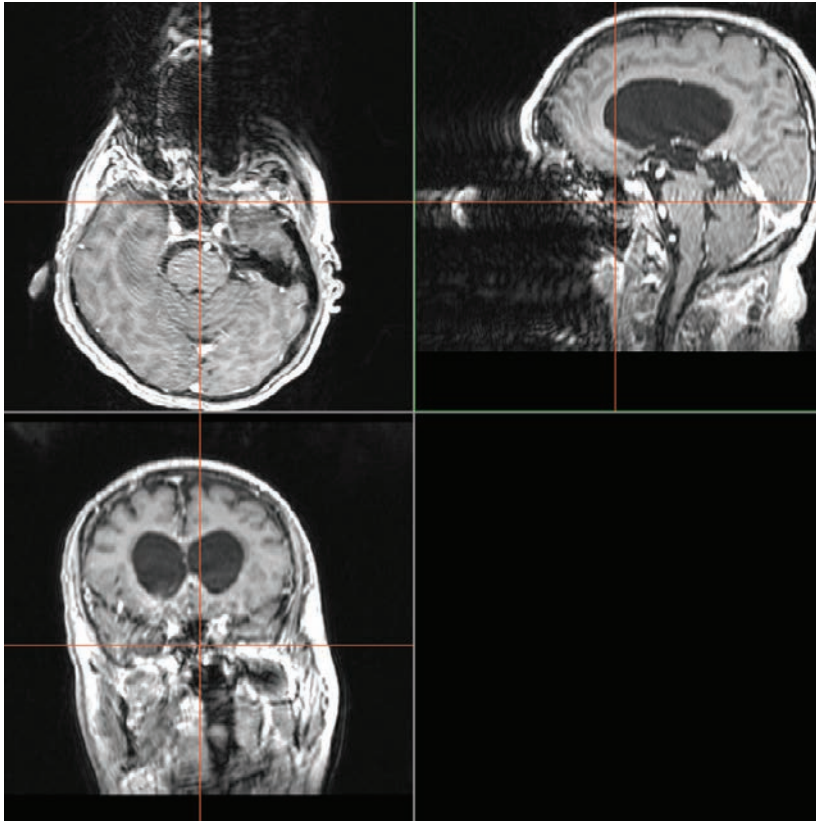


Figure 3. Example of an MRI image artifact caused by the presence of a metal object – wironite (dental implant).

In the last years, the use of a perioperative MRI scanner became very popular. Open systems have been used enabling a neurosurgeon to operate directly inside the acquisition region of the MRI scanner. This method faces a very promising future. It is being proved that a mechanical inaccuracy of the stereotactic assembly or an inaccuracy of an imaging method used is less significant than a brain tissue movement which occurs after breaching the integrity of the skull and the outflow of a part of the CSF or partial tumor resection. MRI is the most advantageous imaging modality for intraoperative control of neurosurgical procedures.

References

- Alexander E, Maciunas RJ. Advanced neurosurgical navigation. New York: Thieme, 1999. 624 p. ISBN 978-08-657-7767-5.
- Čapek M, Krekule I. 1999. Stručný přehled metod registrace biomedicínských dat. *Lékař a technika* 30(5): 99-106.
- Drastich A. Tomografické zobrazovací systémy. Brno: FEI VUT, 2004. 207 p. ISBN 80-214-1974-1.

- Grimson WEL, Ettinger GJ, White SJ, Lozano-Pérez T, Wells WM, Kikinis R. 1996. An Automatic Registration Method for Frameless Stereotaxy, Image Guided Surgery, and Enhanced Reality Visualization. *IEEE Transactions on Medical Imaging* 15(2): 129-140.
- Mikl M, Mareček R, Hlušík P, Pavlicová M, Drastich A, Chlebus P, Brázdil M, Krupa P. 2008. Effects of spatial smoothing on fMRI group inferences. *Magnetic Resonance Imaging* 26(4): 490-503.
- Neuman E, Svoboda T, Fadrus P, Keřkovský M, Šprláková-Puková A. 2011. Využití traktografie začleněné do neuronavigace při operacích intraaxiálních tumorů mozku uložených v těsné blízkosti kortikospinální dráhy. *Česká a slovenská neurologie a neurochirurgie*; 74(6): 675-680.
- Novák Z, Krupa P, Chrastina J, Říha I. Endoscopic surgeries of the ventricular system - presurgical planning, image transmission and virtual reality. In: *Proceedings of 18th International Congress and Exhibition CARS 2004*. Chicago: Elsevier science, 2004, p. 836-841. ISBN 0444517316.
- Říha I, Drastich A, Novák Z, Schwarz D, Chrastina J. Contribution of MRI and CT image fusion to brain surgery planning. In: *Edukační sborník konference XXX. Brněnské onkologické dny, Brno: Masarykův onkologický ústav, 11.–13. května 2006*.

Reduction and classification methods for image data analysis

Eva Janoušová

*Institute of Biostatistics and Analyses, Faculty of Medicine, Masaryk University, Brno;
e-mail: janousova@iba.muni.cz*

Abstract

Advances in medical imaging techniques, such as magnetic resonance imaging, computed tomography and positron emission tomography, have enabled identification of brain regions affected by various neurodegenerative and neuropsychiatric disorders, such as Alzheimer's disease or schizophrenia. Recent efforts are to use medical images also to aid diagnostics of these disabling diseases, as early and accurate diagnostics can significantly improve patient recovery rates and the overall prognosis (Perkins et al., 2005). Algorithms proposed for diagnostics are based on classification of brain images of patients and healthy controls. Due to large amount of imaging features, classification is often preceded by data reduction which enables detection of brain areas influenced by the disease as well. The aim of this part of proceedings is to introduce methods for image data reduction and classification.

Key words

Reduction, classification, principal component analysis, linear discriminant analysis, classification performance.

1. Introduction to image data reduction and classification

The process of image data reduction and classification can be depicted in a scheme (Figure 1). Prior to data reduction, preprocessing of the brain images is often performed to ensure comparability of the images from different subjects. The data preprocessing step depends on the type of input image data. Usually, the images are spatially normalized to the same stereotactic space using registering each of the images to the same template image (image registration is described in more detail in Dr. Daniel Schwarz's extended abstract). The registered images can be also further segmented into gray matter, white matter and cerebrospinal fluid (image segmentation is covered in lecture by Assoc. Prof. Jan Kybic) and smoothed.

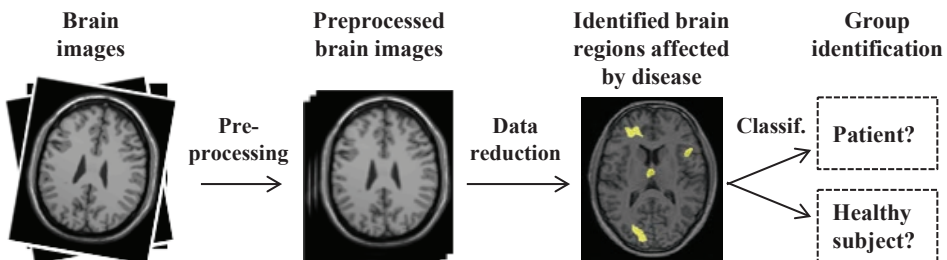


Figure 1. Illustrative scheme of image data analysis. The input images are preprocessed, reduced and classified into one of the groups.

After image preprocessing, data reduction and classification are performed. In contrast with data preprocessing techniques, the reduction and classification methods are applicable for various input image data, for example two-dimensional (2-D) image data of human faces (Xu et al., 2008), 2-D cell images (Orlov et al., 2010), three-dimensional (3-D) or four-dimensional (4-D) medical images of brain, heart, etc. Meyer-Lindenberg et al. (2001) classified brain images acquired with positron emission tomography; Demirci et al. (2008a) used functional magnetic resonance images and Wang & Verma (2008) used diffusion tensor brain images in recognition of schizophrenia patients. Fan et al. (2005), Kawasaki et al. (2007) or Sun et al. (2009) classified patients with schizophrenia and healthy controls on the basis of 3-D anatomical magnetic resonance image data.

The image data reduction and classification methods are described in following chapters. The last chapter is dedicated to evaluation of classification performance.

2. Image data reduction

In neuroscience, brain image data are 3-D or 4-D datasets with hundreds of thousands or millions of voxels. Such large image datasets leads to the so-called “small sample size problem” (Lemm et al., 2011). It means that the number of classified subjects is considerably smaller than the number of features. Here, the features correspond to image voxel values. Demirci et al. (2008b) declare that the small sample size can lead to overtraining of classification algorithms and thus to instable classification results. The small sample size problem is also connected with the “curse of dimensionality” – every subject image can be depicted as a dot in a high dimensional space, where axes correspond to image voxels. The space is mostly empty due to a lower number of dots compared to the space dimensionality. The curse of dimensionality can also cause problems during subsequent image analyses (Bishop, 2006).

For that reason it seems reasonable to reduce the image data before their classification. Images can be reduced using results of voxel-by-voxel statistical tests. It means that the voxels which statistically significantly differ among the groups are selected as the features entering into classification algorithms. These voxels can discriminate the groups quite successfully. However, Guyon & Elisseeff (2003) warn against selection of features separately with no regard to other features. According to Guyon & Elisseeff, a feature that is completely useless by itself can provide a significant improvement of classifier performance when taken with others. Demirci et al. (2008b) point out that the use of separate voxels instead of brain regions can lead to overtraining of a classifier and classification results can be extremely dependent on the real data.

Fan et al. (2005) choose voxels not only according to their own discrimination power but also according to a discrimination power of the neighbouring ones. They reduce brain images into compact clusters of voxels with similar discrimination power. However, neither this approach allows using information included in all voxels during reduction and subsequent classification. Multivariate data reduction techniques, such as principal component analysis (PCA), can be used instead to overcome all the mentioned problems.

2.1. Principal component analysis

The principal component analysis is the most familiar multivariate data reduction method. It is based on an assumption that there are correlations among variables in large datasets. It

means that a part of data is redundant (Wallisch et al., 2009). The goal of PCA is to decrease data dimensionality while keeping as much original data variability as possible. Input variables are transformed into new uncorrelated variables and are sorted according to decreasing variance. The new variables or features are called principal components and they are linear combinations of the original ones (Figure 2). If original variables are correlated, it is sufficient to choose a certain portion of the principal components to preserve the most of the original variability (Jolliffe, 2002).

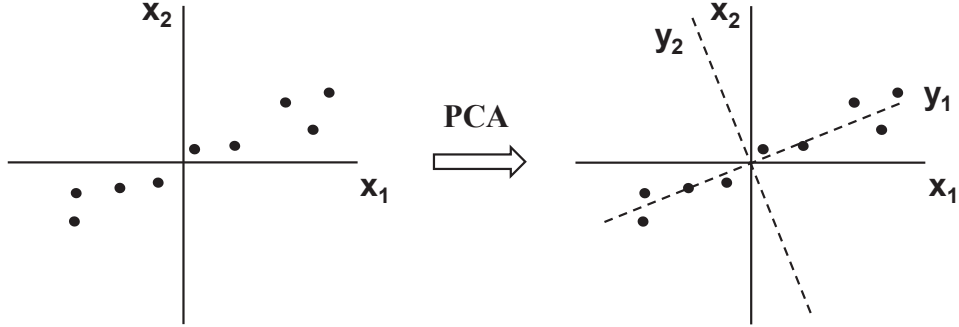


Figure 2. Illustrative example of original variables (x_1 , x_2) and principal components (y_1 , y_2) obtained using PCA.

The PCA algorithm is described in detail for example in (Jolliffe, 2002; Shawe-Taylor & Cristianini, 2006). Briefly, the algorithm comprises computation of a covariance matrix of voxels and its eigenvalues and eigenvectors. Original data are then reduced by using only a selected number of eigenvectors. The steps of the PCA algorithm can be described in more detail as follows:

1. Calculate $n \times n$ covariance matrix of voxels $\mathbf{C} = \frac{1}{N-1}(\mathbf{X} - \bar{\mathbf{X}})^T(\mathbf{X} - \bar{\mathbf{X}})$, where \mathbf{X} is $N \times n$ data matrix composed of N input images with n voxels (rows of the matrix \mathbf{X} are original 3-D images transformed into one-dimensional (1-D) vectors) and $\bar{\mathbf{X}}$ is matrix with all rows equal to a mean image $\bar{\mathbf{x}}$ which is defined by $\bar{\mathbf{x}} = \frac{1}{N} \sum_{i=1}^N \mathbf{x}_i$, where \mathbf{x}_i , $i = 1, \dots, N$, are rows of the matrix \mathbf{X} .
2. Find λ_j eigenvalues and \mathbf{v}_j eigenvectors of the covariance matrix \mathbf{C} , $j = 1, \dots, n$, where n is the number of voxels.
3. Select d eigenvectors that correspond to d eigenvalues which explain most of the original data variability.
4. Construct $n \times d$ projection matrix \mathbf{V} with column-wise computed eigenvectors \mathbf{v}_j .
5. Compute a reduced data matrix \mathbf{Y} with the size of $N \times d$ by $\mathbf{Y} = (\mathbf{X} - \bar{\mathbf{X}}) \cdot \mathbf{V}$.

One of the most important steps in PCA is the selection of the number of principal components. The most common way how to choose the number of principal components is to select the number according to the cumulative percentage of an explained variability – a number around 70% to 90% is usually selected from a scree plot, which shows the portion of the variance in the data explained by each principal component. It is also possible to heighten the threshold above 90% in the case when only one or two components explain most of the variability or to lower the threshold under 70% in the case when too many components are required to explain the variability (Jolliffe, 2002).

Even though the PCA algorithm seems easy to use, its application in neuroscience is not so simple. The brain images are so huge that they lead to large covariance matrices of voxels, which are difficult to evaluate because of high computational and memory requirements. During last decades, modifications of PCA were developed to overcome these problems. Two-dimensional principal component analysis (2DPCA) was proposed by Yang et al. (2004) in the face recognition field. 2DPCA is based on computation of a covariance matrix of rows or columns of an input 2-D image instead of the covariance matrix of voxels. Zhang & Zhou (2005) designed two-directional two-dimensional PCA ((2D)²PCA) which is a modification of 2DPCA. In (2D)²PCA, an input image is reduced using eigenvectors of 2DPCA working in the row direction of images and eigenvectors of 2DPCA working in the column direction. Another improvement of 2DPCA was drafted by Xu et al. (2008) and Kim et al. (2008), who called it bidirectional 2DPCA. The principle of bidirectional 2DPCA is combining features obtained by row-wise 2DPCA and column-wise 2DPCA.

Another approach how to avoid computation of the covariance matrix of voxels was used by Wang et al. (2006) and Demirci et al. (2008b) in analyses of functional magnetic resonance images. Eigenvectors of the covariance matrix of voxels are computed using transformation of eigenvectors of the covariance matrix of persons. The PCA based on the covariance matrix of persons was also applied in the reduction of MRI images of preterm infants and term controls by Thomaz et al. (2007).

Wang et al. (2006) proposed a PCA technique based on a cascade recursive least squared network. This modification of PCA enables computation of principal components from the input image data directly. Therefore it requires neither computation of the covariance matrix of voxels nor allocation of all images into memory simultaneously. However, a disadvantage of the modification of PCA lies in impossibility of using criteria described by Jolliffe (2002) for choosing the most appropriate number of principal components.

The large image datasets are not the only problem in PCA. Principal components that are nonlinear combinations of input variables are demanded in selected cases and such computations are not possible with the original PCA. Therefore nonlinear PCA was designed by Friston et al. (2000). Moreover, there are other modifications of PCA in the literature; for example functional PCA (Viviani et al., 2005), kernel PCA (Shawe-Taylor & Cristianini, 2006) or generalized PCA (Ye et al., 2004).

3. Image data classification

The preprocessing and the reduction steps are followed by classification of image data. There are lots of classification methods in the literature. This subchapter is not dedicated to complete overview of all classification methods. Its goal is to describe methods which are used in classification of patients with neurodegenerative and neuropsychiatric disorders, briefly.

Previously, it was not possible to use information from the whole brain images in classification, due to high computational demands. So, Leonard et al. (1999) classified subjects into a group of patients with schizophrenia and a group of healthy controls according to ten selected anatomical measures which were mean volumes of the left and right hemispheres, volumes of the left and right parts of third ventricle and six sulcal landmarks in Talairach space. In total, 76.0% of patients and 79.0% of healthy controls were classified correctly using these ten anatomical variables. Nakamura et al. (2004) performed linear discriminant analysis using fourteen brain anatomical measures (volumes of fourteen selected regions of interest). The analysis showed correct classification of 77.8% of the female and 80.0% of the male patients with schizophrenia and 86.4% of the female and 80.0% of the male controls.

Even though classification efficiency of algorithms used by Leonard et al. (1999) and Nakamura et al. (2004) was quite high, classification performance can be further improved using information from whole brain images. Kawasaki et al. (2007) discriminated 3-D magnetic resonance (MR) brain images which were segmented into the grey matter, white matter and cerebrospinal fluid with the use of multivariate linear model based on canonical variates analysis. An accuracy of their classifier was 84.4%. Meyer-Lindenberg et al. (2001) also used canonical variates analysis for classification. In comparison with Kawasaki et al. (2007), they classified positron emission tomography imaging data instead of segmented MR images and reached the accuracy of 94.0%. Sun et al. (2009) achieved classification efficiency of 86.1% with the use of sparse multinomial logistic regression. Shi et al. (2007) classified functional MRI data using pseudo-Fisher linear discriminative analysis. Their classifier enabled correct classification of 83.0% of patients with schizophrenia and 74.0% of control subjects.

Support vector machines (SVM) technique is also often used for brain image classification. The goal of SVM is to construct a hyperplane which is capable of separating images from different groups (Figure 3). Especially, the main effort is the best possible division of margin images called support vectors (Bishop, 2006; Shawe Taylor & Cristianini, 2006). The efficiency of linear SVM was about 90% in classification of brain images of patients with Alzheimer disease (Klöppel et al., 2008) and up to 90% in classification of patients with schizophrenia based on structure-specific 9-parameter affine transformations of MRI images (Pohl & Sabuncu, 2009). Nonlinear SVM was used by Fan et al. (2005) with the accuracy of 91.8% in the schizophrenia research. Fan et al. (2005) proposed a complex algorithm comprising data preprocessing, selection of features and classification methods. Later the algorithm was called COMPARE (Classification of Morphological Patterns Using Adaptive Regional Elements) by Fan et al. (2007). The algorithm was also used in classification of relatives of schizophrenia patients (Fan et al., 2008).

Beside discriminant analysis methods and support vector machines, clustering methods can be also used for data classification. Clustering methods are for example the centroid method, the average linkage method or the k -nearest neighbor (k -NN) algorithm. The principle of clustering methods is computation of distances among images in the high dimensional space. The images are dots in the space and voxels are axes (Figure 4). In the centroid method, distances of a new image from centroids of both the image groups (for example patients and healthy controls) are computed. The image is then classified into the group represented by the closer centroid (Legendre & Legendre, 1998). In the average linkage method, the shorter one of the average distances of the new image from all images of the first group and from all second group ones indicates classification of the new image into the group (Legendre & Legendre, 1998). In k -NN algorithm, a new image is classified into the group which is most common among its k nearest neighbors (Bishop, 2006). 1-nearest neighbor is often used in

the face recognition. It means the algorithm is based on looking for one image which is the most resembling to a new image (Yang et al., 2004; Delac et al., 2005; Kim et al., 2008). Wang & Verma (2008) used k -NN in classification of diffusion tensor images of patients with schizophrenia. They compared results of classification using k -NN to the results obtained using support vector machines.

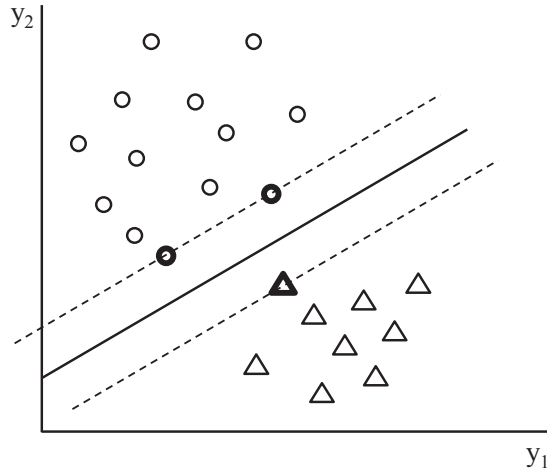


Figure 3. Classification of image data using support vector machines. The triangles represent patients, the circles depict healthy controls. The bold symbols are the support vectors which lie in the margins (denoted as dashed lines). The solid line represents the separating hyperplane. The axes y_1 and y_2 correspond to principal components.

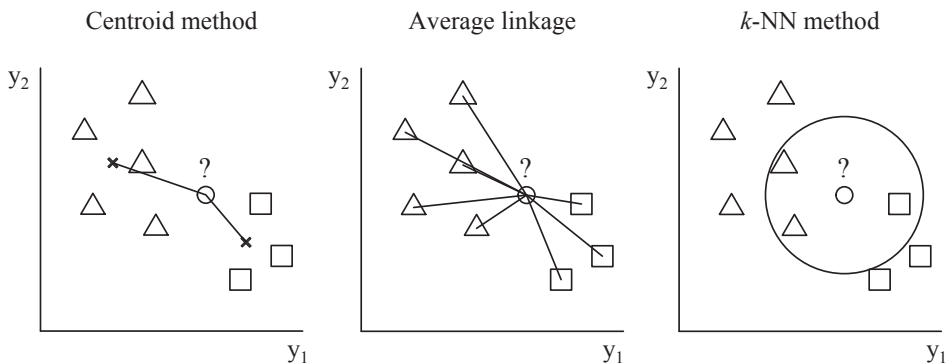


Figure 4. Classification of image data using clustering methods. The triangles represent patients, the squares depict healthy controls. The crosses are group centroids. The new image which is supposed to be classified is denoted with the circle. The axes y_1 and y_2 correspond to principal components.

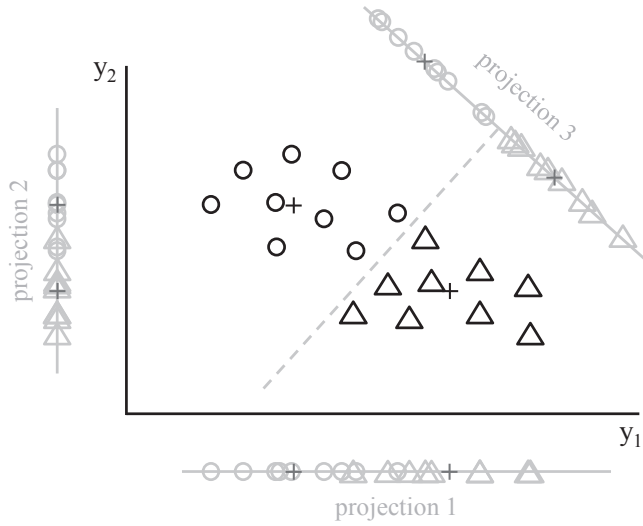


Figure 5. Classification of image data using Fisher's linear discriminant analysis. The triangles represent patients, the circles depict healthy controls. The crosses are group centroids. The axes y_1 and y_2 correspond to principal components. The projection 1 shows large distance between the groups but there is an overlap of the groups. The projection 2 shows small variability between the groups but there is also an overlap of the groups. The projection 3 maximizes the distance between the groups and minimizes variability within the groups and there is no overlap of the groups. The dashed line represents a discriminant hyperplane which is perpendicular to the projection hyperplane.

Other data classification techniques, such as neuronal networks, decision trees and random forests, have not been used in brain image data classification extensively yet. So, linear discriminant analysis, which has been used widely in classification of images of patients with neurodegenerative and neuropsychiatric disorders, is described in more detail here. Specifically, the following subchapter is dedicated to Fisher's linear discriminant analysis.

3.1. Fisher's linear discriminant analysis

The principle of the Fisher's linear discriminant analysis is based on transformation of the data in original multidimensional space into 1-D space while maximizing the distance between the groups and minimizing variability within the groups (Figure 5). Thus, the Fisher's linear discriminant is defined as:

$$J(\mathbf{w}) = \frac{(\bar{z}_D - \bar{z}_H)^2}{s_D^2 + s_H^2}, \quad (1)$$

where \bar{z}_D is a projection of the centroid of patients $\bar{\mathbf{y}}_D$ (D..diseased) into 1-D space, \bar{z}_H is a projection of the centroid of controls $\bar{\mathbf{y}}_H$ (H..healthy), s_D^2 is a variance in a group of patients after projection into 1-D space and s_H^2 is a variance in a group of controls after the projection.

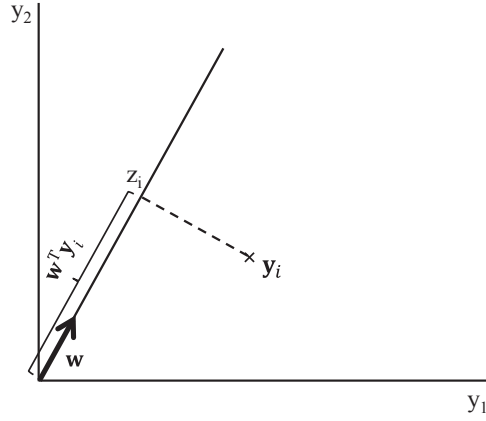


Figure 6. Illustration of projection of a point into 1-D space. The axes y_1 and y_2 correspond to principal components. The point y_i represents the i th subject and z_i is the projection of the point y_i to the 1-D hyperplane given by the direction vector \mathbf{w} .

The centroids are the mean vectors of patients and controls:

$$\bar{y}_D = \left[\frac{1}{n_D} \sum_{i=1}^{n_D} y_{i1} \quad \frac{1}{n_D} \sum_{i=1}^{n_D} y_{i2} \quad \cdots \quad \frac{1}{n_D} \sum_{i=1}^{n_D} y_{id} \right], \quad (2a)$$

$$\bar{y}_H = \left[\frac{1}{n_H} \sum_{i=1}^{n_H} y_{i1} \quad \frac{1}{n_H} \sum_{i=1}^{n_H} y_{i2} \quad \cdots \quad \frac{1}{n_H} \sum_{i=1}^{n_H} y_{id} \right], \quad (2b)$$

where y_{i1} is a value of the first principal component (i.e. a value of the first variable in a data set reduced by PCA) in an i th subject, n_D and n_H are a number of patients and controls, respectively, and d is a number of variables after PCA reduction. The projections of the centroids in 1-D space can be calculated as $\bar{z}_D = \mathbf{w}^T \bar{y}_D$ and $\bar{z}_H = \mathbf{w}^T \bar{y}_H$, where \mathbf{w} is a direction of the discriminant hyperplane. In general, projection of any point (i.e. subject) into 1-D space is visualized in Figure 6 and can be computed as:

$$z_i = \mathbf{w}^T \mathbf{y}_i \quad (3)$$

The variance in the group of patients (s_D^2) is a squared distance of projections of all patients into the 1-D space from the projection of the centroid of patients and can be expressed as:

$$\begin{aligned} s_D^2 &= \sum_{i=1}^{n_D} (z_i - \bar{z}_D)^2 \\ &= \sum_{i=1}^{n_D} (\mathbf{w}^T \mathbf{y}_i - \mathbf{w}^T \bar{y}_D)^2 \\ &= \sum_{i=1}^{n_D} (\mathbf{w}^T (\mathbf{y}_i - \bar{y}_D))^2 = \mathbf{w}^T \left(\sum_{i=1}^{n_D} (\mathbf{y}_i - \bar{y}_D)(\mathbf{y}_i - \bar{y}_D)^T \right) \mathbf{w} = \mathbf{w}^T \mathbf{S}_D \mathbf{w}, \end{aligned}$$

where \mathbf{S}_D is a covariance matrix of patients.

Accordingly, the variance in the group of controls is expressed as:

$$s_H^2 = \sum_{i=1}^{n_H} (z_i - \bar{z}_H)^2 = \sum_{i=1}^{n_H} (\mathbf{w}^T \mathbf{y}_i - \mathbf{w}^T \bar{\mathbf{y}}_H)^2 = \mathbf{w}^T \left(\sum_{i=1}^{n_H} (\mathbf{y}_i - \bar{\mathbf{y}}_H)(\mathbf{y}_i - \bar{\mathbf{y}}_H)^T \right) \mathbf{w} = \mathbf{w}^T \mathbf{S}_H \mathbf{w},$$

where \mathbf{S}_H is a covariance matrix of controls.

In the denominator of the Fisher's linear discriminant, there is a sum of the variances s_D^2 and s_H^2 which can be re-written as:

$$\begin{aligned} s_D^2 + s_H^2 &= \mathbf{w}^T \mathbf{S}_D \mathbf{w} + \mathbf{w}^T \mathbf{S}_H \mathbf{w} \\ &= \mathbf{w}^T \left(\sum_{i=1}^{n_D} (\mathbf{y}_i - \bar{\mathbf{y}}_D)(\mathbf{y}_i - \bar{\mathbf{y}}_D)^T \right) \mathbf{w} + \mathbf{w}^T \left(\sum_{i=1}^{n_H} (\mathbf{y}_i - \bar{\mathbf{y}}_H)(\mathbf{y}_i - \bar{\mathbf{y}}_H)^T \right) \mathbf{w} \\ &= \mathbf{w}^T \left(\sum_{i=1}^{n_D} (\mathbf{y}_i - \bar{\mathbf{y}}_D)(\mathbf{y}_i - \bar{\mathbf{y}}_D)^T + \sum_{i=1}^{n_H} (\mathbf{y}_i - \bar{\mathbf{y}}_H)(\mathbf{y}_i - \bar{\mathbf{y}}_H)^T \right) \mathbf{w} \\ &= \mathbf{w}^T \mathbf{S}_W \mathbf{w}, \end{aligned}$$

where \mathbf{S}_W is the within-class scatter matrix and is calculated as $\mathbf{S}_W = \mathbf{S}_D + \mathbf{S}_H = \sum_{i=1}^{n_D} (\mathbf{y}_i - \bar{\mathbf{y}}_D)(\mathbf{y}_i - \bar{\mathbf{y}}_D)^T + \sum_{i=1}^{n_H} (\mathbf{y}_i - \bar{\mathbf{y}}_H)(\mathbf{y}_i - \bar{\mathbf{y}}_H)^T$. If there is not the same number of subjects in the groups, \mathbf{S}_W is computed as $\mathbf{S}_W = \frac{(n_D-1)\mathbf{S}_D + (n_H-1)\mathbf{S}_H}{(n_D+n_H-2)}$.

The numerator of the Fisher's linear discriminant can be re-written as:

$$\begin{aligned} (\bar{z}_D - \bar{z}_H)^2 &= (\mathbf{w}^T \bar{\mathbf{y}}_D - \mathbf{w}^T \bar{\mathbf{y}}_H)^2 = (\mathbf{w}^T (\bar{\mathbf{y}}_D - \bar{\mathbf{x}}_H))^2 = \mathbf{w}^T (\bar{\mathbf{y}}_D - \bar{\mathbf{y}}_H)(\bar{\mathbf{y}}_D - \bar{\mathbf{y}}_H)^T \mathbf{w} \\ &= \mathbf{w}^T \mathbf{S}_B \mathbf{w}, \end{aligned}$$

where \mathbf{S}_B is the between-class scatter matrix.

Thus, Fisher's linear discriminant can be expressed as: $J(\mathbf{w}) = \frac{(\bar{z}_D - \bar{z}_H)^2}{s_D^2 + s_H^2} = \frac{\mathbf{w}^T \mathbf{S}_B \mathbf{w}}{\mathbf{w}^T \mathbf{S}_W \mathbf{w}}$.

The goal is to maximize $J(\mathbf{w})$. Therefore, the derivative of $J(\mathbf{w})$ is calculated and set to 0:

$$\begin{aligned} \frac{\partial}{\partial \mathbf{w}} J(\mathbf{w}) &= 0 \\ \frac{\left(\frac{\partial}{\partial \mathbf{w}} \mathbf{w}^T \mathbf{S}_B \mathbf{w} \right) \mathbf{w}^T \mathbf{S}_W \mathbf{w} - \mathbf{w}^T \mathbf{S}_B \mathbf{w} \left(\frac{\partial}{\partial \mathbf{w}} \mathbf{w}^T \mathbf{S}_W \mathbf{w} \right)}{(\mathbf{w}^T \mathbf{S}_W \mathbf{w})^2} &= 0 \\ \frac{(2\mathbf{S}_B \mathbf{w}) \mathbf{w}^T \mathbf{S}_W \mathbf{w} - \mathbf{w}^T \mathbf{S}_B \mathbf{w} (2\mathbf{S}_W \mathbf{w})}{(\mathbf{w}^T \mathbf{S}_W \mathbf{w})^2} &= 0 \\ (\mathbf{w}^T \mathbf{S}_B \mathbf{w}) \mathbf{S}_W \mathbf{w} &= (\mathbf{w}^T \mathbf{S}_W \mathbf{w}) \mathbf{S}_B \mathbf{w} \end{aligned}$$

$\mathbf{S}_B \mathbf{w}$ is in the direction of $(\bar{\mathbf{y}}_D - \bar{\mathbf{y}}_H)$, because $\mathbf{S}_B \mathbf{w} = (\bar{\mathbf{y}}_D - \bar{\mathbf{y}}_H)(\bar{\mathbf{y}}_D - \bar{\mathbf{y}}_H)^T \mathbf{w} = (\bar{\mathbf{y}}_D - \bar{\mathbf{y}}_H) \cdot \alpha$, where α is a scalar. The scale factor of \mathbf{w} is immaterial, so it is possible to ignore $\mathbf{w}^T \mathbf{S}_B \mathbf{w}$ and $\mathbf{w}^T \mathbf{S}_W \mathbf{w}$ and we get:

$$\begin{aligned} \mathbf{S}_W \mathbf{w} &\sim \mathbf{S}_B \mathbf{w} \\ \mathbf{S}_W \mathbf{w} &\sim (\bar{\mathbf{y}}_D - \bar{\mathbf{y}}_H) \end{aligned}$$

The direction of the discriminant hyperplane can be then calculated as:

$$\mathbf{w} \sim S_W^{-1}(\bar{\mathbf{y}}_D - \bar{\mathbf{y}}_H). \quad (4)$$

When the direction of the discriminant hyperplane is known, the subjects are classified into the group of patients or controls according to if they are place on the left or right side of the discriminant hyperplane.

4. Evaluation of classification performance

Evaluation of classification performance is a very important step in the image data reduction and classification. The evaluation requires a testing data set, i.e. data not used during classifier training. Ideally, independent data sample (e.g. image data from different clinical centre) is used for testing. However, such independent sample is usually not available, so splitting of the data set into a training set and a testing set is performed (Kuncheva, 2004). There are several ways of the data set splitting:

- Resubstitution method – Classifier is trained and tested on the same data set (i.e. all image data are used for training and testing). It leads to overtraining of the classifier and the classification performance is optimistically biased. So, resubstitution is not recommended.
- Bootstrap – A training set is selected randomly from the data set, with replacement. The testing set comprises data which were not used for training.
- Hold-out method – The data set is randomly split into two parts and one part is used for training and the other one for testing. Usually, the training set contains one half of the data and testing set the other half or the training set comprises two-thirds of the data and the testing set one-third of the data. If the data sets are split into halves, it is possible to swap the two subsets and average the classifier performances. Another modification is to perform the hold-out several times, i.e. to do several random splits of the data set into the training and testing sets (as shown in Figure 7), and average the results.
- k -fold cross-validation – this method randomly splits the image data into k roughly equal-sized parts (the folds). The $k - 1$ parts are used for training and k th fold is a testing image set. The training and testing steps are repeated k times; it means every fold is used for testing exactly once (see Figure 7). The k classification results are then combined (usually averaged) to estimate the classification efficiency. Commonly, 10-fold cross-validation is used (Hastie et al., 2009; Kohavi, 1995). If k is equal to the number of images, the N -fold cross-validation is called leave-one-out cross-validation (LOOCV). In this case one image is chosen as a testing image and the remaining images constitute the training dataset. This is repeated for each image (Fan et al., 2008; Hastie et al., 2009).

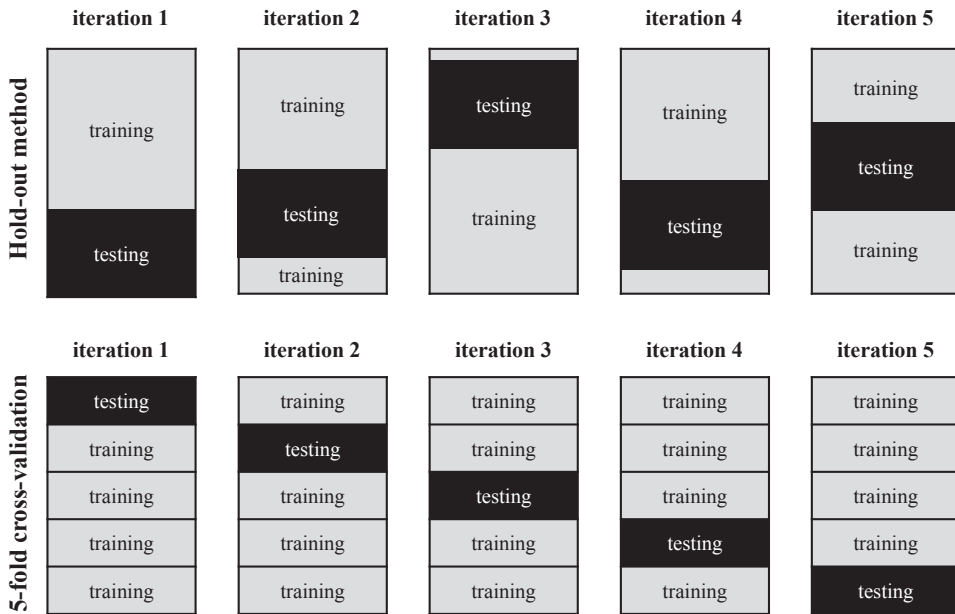


Figure 7. Example of splitting a data set into training and testing subsets using hold-out method which is repeated 5-times and using 5-fold cross-validation.

Demirci et al. (2008b) recommend using splitting into the training and testing data set in all steps of data recognition. Otherwise, biased results could be obtained. The correct image data reduction and classification scheme is visualized in Figure 8 and can be briefly described in following steps:

1. Reduce training images, for example with the use of the projection matrix of PCA. It is important to notice that training images without the testing image are the input into the reduction methods.
2. Reduce the testing image using the computed projection matrix from the previous step.
3. Classify the testing image into the group of patients or controls with the use of a classification algorithm trained on reduced training image data.

As the correct class label of the image is known, the classification efficiency is easy to calculate. The efficiency can be derived from the confusion matrix (Altman, 1999) that is visualized in Tab. 1. The confusion matrix shows:

- how many recognition results were true positive (TP); it means how many patient images were correctly classified as patient ones;
- how many recognition results were false negative (FN); it means how many patient images were incorrectly classified as control ones;
- how many recognition results were true negative (TN); it means how many control images were correctly classified as control ones;
- how many recognition results were false positive (FP); it means how many control images were incorrectly classified as patient ones.

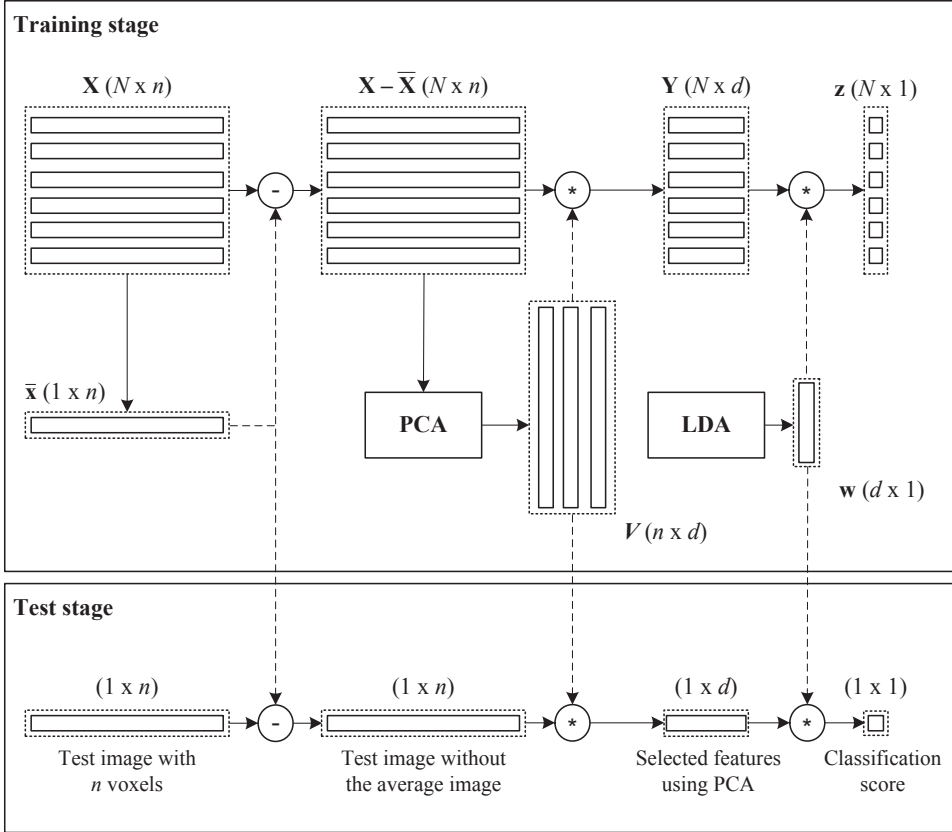


Figure 8. Scheme of image data reduction and classification with correctly performed leave-one-out cross-validation. The scheme was created on the basis of figure in (Thomaz et al., 2007). \mathbf{X} is the image data matrix where rows are 3-D images transformed into 1-D vectors; $\bar{\mathbf{x}}$ is the mean image; $\mathbf{X} - \bar{\mathbf{X}}$ is the matrix with all rows equal to the mean image; \mathbf{Y} is the reduced matrix computed using PCA, \mathbf{z} is the vector with classification scores, \mathbf{V} is the projection matrix of PCA and \mathbf{w} is the projection vector in LDA.

Table 1. Confusion matrix. TP stands for true positive recognition results, FP stands for false positive results, TN stands for true negative results and FN stands for false negative results.

Correct class	Recognition result	
	Patients (+)	Controls (-)
Patients (+)	TP	FN
Controls (-)	FP	TN

The values in the confusion matrix allow for evaluation of classification efficiency using following measures:

$$\text{accuracy} = \frac{TP + TN}{TP + TN + FP + FN}, \quad (5)$$

$$\text{sensitivity} = \frac{TP}{TP + FN}, \quad (6)$$

$$\text{specificity} = \frac{TN}{TN + FP}. \quad (7)$$

The accuracy is thus the percentage of all correctly classified subjects among all subjects, the sensitivity is the proportion of patients who are correctly identified as patients by the classification method, and specificity is the percentage of correctly classified healthy controls. Even though accuracy is the only measure reported in many scientific papers, Demirci et al. (2008b) urge to report sensitivity and specificity as well.

References

- Altman DG. 1999. *Practical Statistics for Medical Research*. London: Chapman and Hall/CRC.
- Bishop C. 2006. *Pattern Recognition and Machine Learning*. New York: Springer.
- Delac K, Grgic M, Grgic S. 2005. Independent comparative study of PCA, ICA, and LDA on the FERET data set. *International Journal of Imaging Systems and Technology* 15: 252-260.
- Demirci O, Clark V, Calhoun VD. 2008a. A projection pursuit algorithm to classify individuals using fMRI data: Application to schizophrenia. *NeuroImage* 39: 1774-1782.
- Demirci O, Clark VP, Magnotta VA, Andreasen NC, Lauriello J, Kiehl KA, Pearlson GD, Calhoun VD. 2008b. A Review of challenges in the use of fMRI for disease classification / characterization and a projection pursuit application from multi-site fMRI schizophrenia study. *Brain Imaging and Behavior* 2: 147-226.
- Fan Y, Shen DG, Davatzikos C. 2005. Classification of structural images via high-dimensional image warping, robust feature extraction, and SVM. *Lecture Notes in Computer Science* 3749: 1-8.
- Fan Y, Shen D, Gur RC, Gur RE, Davatzikos C. 2007. COMPARE: Classification of morphological patterns using adaptive regional elements. *IEEE Transactions on Medical Imaging* 26: 93-105.
- Fan Y, Gur RE, Gur RC, Wu X, Shen D, Calkins ME, Davatzikos C. 2008. Unaffected family members and schizophrenia patients share brain structure patterns: A high-dimensional pattern classification study. *Biological Psychiatry* 63: 118-124.
- Friston K, Phillips J, Chawla D, Buchel C. 2000. Nonlinear PCA: characterizing interactions between modes of brain activity. *Philosophical Transactions of The Royal Society of London Series B-Biological Sciences* 355: 135-146.
- Guyon I, Elisseeff A. 2003. An introduction to variable and feature selection. *Journal of Machine Learning Research* 3: 1157-1182.
- Hastie T, Tibshirani R, Friedman J. 2009. *The Elements of Statistical Learning: Data Mining, Inference, and Prediction*. New York: Springer.
- Jolliffe IT. 2002. *Principal Component Analysis*. New York: Springer.
- Kawasaki Y, Suzuki M, Kherif F, Takahashi T, Zhou SY, Nakamura K, Matsui M, Sumiyoshi T, Seto H., Kurachi M. 2007. Multivariate voxel-based morphometry successfully differentiates schizophrenia patients from healthy controls. *NeuroImage* 34: 235-242.
- Kim YG, Song YJ, Chang UD, Kim DW, Yun TS, Ahn JH. 2008. Face recognition using a fusion method based on bidirectional 2DPCA. *Applied Mathematics and Computation* 205: 601-607.
- Klöppel S, Stonnington CM, Chu C, Draganski B, Scahill RI, Rohrer JD, Fox NC, Jack CR, Ashburner J, Frackowiak RS. 2008. Automatic classification of MR scans in Alzheimer's disease. *Brain* 131: 681-689.

- Kohavi R. 1995. A study of cross-validation and bootstrap for accuracy estimation and model selection. *Proceedings of the Fourteenth International Joint Conference on Artificial Intelligence*, 1137-1145.
- Kuncheva LI. 2004. *Combining classifiers: ideas and methods*. New Jersey: John Wiley & Sons.
- Legendre P, Legendre L. 1998. *Numerical ecology*. Amsterdam: Elsevier Science.
- Lemm S, Blankertz B, Dickhaus T, Mueller KR. 2011. Introduction to machine learning for brain imaging. *Neuroimage* 56: 387-399.
- Leonard CM, Kuldau JM, Breier JI, Zuffante PA, Gautier ER, Heron DC, Lavery EM, Packing J, Williams SA, DeBose CA. 1999. Cumulative effect of anatomical risk factors for schizophrenia: an MRI study. *Biological Psychiatry* 46: 374-382.
- Meyer-Lindenberg A, Poline JB, Kohn PD, Holt JL, Egan MF, Weinberger DR, Berman KF. 2001. Evidence for abnormal cortical functional connectivity during working memory in schizophrenia. *American Journal of Psychiatry* 158: 1809-1817.
- Nakamura K, Kawasaki Y, Suzuki M, Hagino H, Kurokawa K, Takahashi T, Niu L, Matsui M, Seto H, Kurachi M. 2004. Multiple structural brain measures obtained by three-dimensional magnetic resonance imaging to distinguish between schizophrenia patients and normal subjects. *Schizophrenia Bulletin* 30: 393-404.
- Orlov NV, Chen WW, Eckley DM, Macura TJ, Shamir L, Jaffe ES, Goldberg IG. 2010. Automatic classification of lymphoma images with transform-based global features. *IEEE Transactions on Information Technology in Biomedicine* 14: 1003-1013.
- Perkins DO, Gu HB, Boteva K, Lieberman JA. 2005. Relationship between duration of untreated psychosis and outcome in first-episode schizophrenia: A critical review and meta-analysis. *American Journal of Psychiatry* 162: 1785-1804.
- Pohl KM, Sabuncu MR. 2009. A unified framework for MR based disease classification. *Lecture Notes in Computer Science* 5636: 300-313.
- Shawe-Taylor J, Cristianini N. 2006. *Kernel Methods for Pattern Analysis*. Cambridge: Cambridge University Press.
- Shi F, Liu Y, Jiang TZ, Zhou Y, Zhu WL, Jiang JF, Liu HH, Liu ZN. 2007. Regional homogeneity and anatomical parcellation for fMRI image classification: Application to schizophrenia and normal controls. *Lecture Notes in Computer Science* 4792: 136-143.
- Sun DQ, van Erp TGM, Thompson PM, Bearden CE, Daley M, Kushan L, Hardt ME, Nuechterlein KH, Toga AW, Cannon TD. 2009. Elucidating a magnetic resonance imaging-based neuroanatomic biomarker for psychosis: classification analysis using probabilistic brain atlas and machine learning algorithms. *Biological Psychiatry* 66: 1055-1060.
- Thomaz CE, Boardman JP, Counsell S, Hill DLG, Hajnal JV, Edwards AD, Rutherford MA, Gillies DF, Rueckert D. 2007. A multivariate statistical analysis of the developing human brain in preterm infants. *Image and Vision Computing* 25: 981-994.
- Viviani R, Gron G, Spitzer M. 2005. Functional principal component analysis of fMRI data. *Human Brain Mapping* 24: 109-129.
- Wallisch P, Lusignan M, Benayoun M, Baker TI, Dickey AS, Hatsopoulos NG. 2009. *Matlab for Neuroscientists: An Introduction to Scientific Computing in Matlab*. San Diego: Academic Press.
- Wang Z, Wang J, Calhoun V, Rao H, Detre JA, Childress AR. 2006. Strategies for reducing large fMRI data sets for independent component analysis. *Magnetic Resonance Imaging* 24: 591-596.
- Wang P, Verma R. 2008. On classifying disease-induced patterns in the brain using diffusion tensor images. *Lecture Notes in Computer Science* 5241: 908-916.
- Xu Y, Zhang D, Yang J, Yang JY. 2008. An approach for directly extracting features from matrix data and its application in face recognition. *Neurocomputing* 71: 1857-1865.

- Yang J, Zhang D, Frangi AF, Yang JY. 2004. Two-dimensional PCA: a new approach to appearance-based face representation and recognition. *IEEE Transactions on Pattern Analysis and Machine Intelligence* 26: 131-137.
- Ye J, Janardan R, Li Q. 2004. GPCA: an efficient dimension reduction scheme for image compression and retrieval. *ACM International Conference on Knowledge Discovery and Data Mining (SIGKDD04)*, 354-363.
- Zhang D, Zhou ZH. 2005. $(2D)^2$ PCA: two-directional two-dimensional PCA for efficient face representation and recognition. *Neurocomputing* 69: 224-231.

Machine learning algorithms

Jan Kybic

*Department of Cybernetics, Czech Technical University, Prague;
e-mail: kybic@fel.cvut.cz*

Abstract

The aim of the lecture is to introduce image segmentation based on features. The feature vector containing information about colour or texture is acquired in every image element (pixel, voxel or superpixel). The image elements are then classified into classes, such as background or object elements, based on the feature vectors. If data labelled by an expert are available, classification into the classes is performed using supervised methods, such as linear classifier, support vector machines (SVM), Adaboost and random decision trees. If data labels are not accessible, unsupervised methods are used, e.g. k-means method or expectation-maximization (EM) algorithm. Image segmentation can be further improved using information about spatial distribution of the classes.

Key words

Image segmentation, supervised, unsupervised, support vector machines, Adaboost, random decision trees, k-means, expectation-maximization algorithm.

Déjà-vu phenomenon from the perspective of computational neuroanatomy

Milan Brázdil¹, Radek Mareček²

¹ *Behavioral and Social Neuroscience Research Group, CEITEC-Central European Institute of Technology, Masaryk University, Brno;*

e-mail: mbrazd@med.muni.cz

² *Multi-modal and Functional Neuroimaging Research Group, CEITEC-Central European Institute of Technology, Masaryk University, Brno;*

e-mail: rmarec@med.muni.cz

Abstract

More than two thirds of healthy population has an experience with the déjà-vu phenomenon. It is a feeling of re-experiencing distinct situation along with the realization that the feeling is inappropriate. There is no known widely agreed mechanism of non-pathological déjà-vu, though electrophysiological studies with intracerebral electrodes indicate, that déjà-vu in patients with temporal epilepsy is a consequence of subtle disruptions in communication among brain regions involved in memory networks. Using two statistical technics, we investigated the relationship between gray matter morphology and frequency of déjà-vu experience in the cohort of healthy subjects. We acquired whole head magnetic resonance images with high spatial resolution. The images were processed by commonly used Voxel Based Morphometry method – an univariate linear model – and by complementary Source Based Morphometry method (SBM). SBM employs Independent Component Analysis which blindly separates independent spatial sources of inter-subject variability in local gray matter volume (GMV). We found statistically significant effect of déjà-vu frequency for one of the sources – the more frequent experience, the less local GMV. The source was localized in subcortical and mesiotemporal cortical regions which are known to play important role in memory networks. The results support hypothesis of neurophysiological origin of déjà-vu and its relationship to morphological and functional changes in the memory networks.

Key words

Déjà-vu, brain, morphology, ICA.

1. Introduction

Déjà-vu (DV) is an experience of two concurrent feelings, a familiarity of distinct situation along with an awareness that this familiarity is inappropriate (Brown, 2003). The DV is reported by 60–80% of healthy population (Adachi et al., 2003). Although, there is no known widely agreed mechanism of its origin, recent review suggests that it might be caused by disruptions in attention and memory processes (Adachi et al., 2003). Moreover, DV appears as an aura in patients with temporal epilepsy disease. This fact motivated several electrophysiological studies which together indicate DV related network comprising mesiotemporal regions, which are known to be parts of memory networks (Guedj et al., 2010; Kovacs et al., 2009; Vignal et al., 2007).

The goal of our study was to investigate if there is a similar network in healthy people involved in DV generation. We searched for possible morphological alterations in memory networks by comparing subjects with and without self-reported DV experiences.

We used two commonly used statistical technics to search for brain regions with hypothesized alteration in local gray matter volume (GMV): (a) an univariate statistical approach – Voxel Based Morphometry (VBM) (Mechelli et al., 2005) which uses general linear model to test the hypothesized effect independently in each voxel and (b) multivariate statistical method – Source Based Morphology (SBM) (Xu et al., 2009) which employs Independent Component Analysis to find spatial sources of inter-subject variability in local GMV. Both methods provide complementary results. While VBM can reveal spatially very distinct but sufficiently sized effects and lacks when the effect size is low, SBM was shown to be more sensitive to subtle but still vastly spatially distributed effects in image data (Kasperek et al., 2010).

2. Methods

2.1. Subjects

The study cohort consisted of 113 subjects (Table 1), all right-handed healthy volunteers who participated in various functional MRI studies in our laboratory, and have fulfilled the Czech version of the Inventory for Déjà Vu Experiences Assessment (IDEA) (Sno et al., 1994). At first, the subjects were divided into two groups according to the answer to the first question of the IDEA – “Have you ever had the feeling of having experienced a sensation or situation before in exactly the same way when in fact you are experiencing it for the first time?” Subjects who answered “yes” formed déjà-vu group (DVG) and subjects who answered “never” formed non déjà-vu group (nonDVG). Secondly, the subjects were categorized into 5 groups according to the reported frequency of DV occurrences (Table 1).

Table 1. Demographic data. Groups “often” and “very often” merged together due to small sample size. No significant effect of group factor neither for age nor for gender.

Group (déjà-vu frequency)	N	Age median (range)	Gender males/females
never	26	24 (20 ÷ 50)	13/13
very infrequent	24	24 (20 ÷ 38)	10/14
sometimes	52	24 (19 ÷ 46)	27/25
often	9	24 (21 ÷ 27)	6/3
very often	2	26 (24 ÷ 28)	2/0

2.2. MR imaging and preprocessing

All images were acquired on 1.5T Siemens Symphony scanner using 3D acquisition technic with IR/GR sequence, TR 1700 ms, TE 3.93 ms, TI 1100 ms, flip angle 15°, 160 sagittal slices, voxel size 1.17 x 0.48 x 0.48 mm, FOV = 246 x 246 mm, plane matrix size 512x512 voxels. The raw data were visually inspected to avoid inclusion images with huge image artifacts. No images were excluded.

Images were preprocessed using SPM5 software (<http://www.fil.ion.ucl.ac.uk/spm>), running on Matlab platform. Data were segmented into gray and white matter segments using

Bayesian framework algorithm (Ashburner and Friston, 2005). The voxels values in resulting images had a character of posterior probability of belonging to either tissue classes. The images were registered by high-dimensional non-linear transformation (DARTEL - diffeomorphic anatomical registration through exponentiated lie algebra) to a study specific template (Ashburner, 2007). The resulting gray matter volume images were smoothed with 8mm FWHM Gaussian Kernel to improve signal-to-noise ratio and intensity normalized using individual estimates of total intracranial volume to filter out the effect of head size variability. Finally, the individual 3D image data were reshaped to form 2D matrix $D \in \mathfrak{R}^{nV, nS}$, where nS is number of subjects and nV is number of voxels.

2.3. Statistical Analysis

2.3.1. Voxel Based Morphometry

The general linear model used for VBM has the form of:

$$D = X \cdot \beta + \varepsilon$$

where X is a design matrix of ANCOVA model with factor “group” and additional regressors of age and gender which model nuisance variability in data; β stands for estimated effects of regressors and ε for model residuals. The effect of factor “group” was then tested by two sample T-test to reveal voxels with significant difference in local GMV between DVG and nDVG. The resulting statistical parametric map of T-values was thresholded at the level of $p < 0.05$, corrected for multiple testing by Random Field theory approach (Nichols and Hayasaka, 2003) which controls Family Wise Error.

2.3.2. Source Based Morphometry

The resulting 2D matrix D was subjected to SBM. At first, the dimensionality of the data was reduced using Principal Component Analysis (PCA) by retaining optimal number nC of spatial principal components:

$$\text{PCA reduction step: } D \approx R \cdot dwM$$

where $R \in \mathfrak{R}^{nV, nC}$ is a matrix of principal components and $dwM \in \mathfrak{R}^{nC, nS}$ is a de-whitening matrix. The optimal number nC was estimated using Minimum Description Length Criterion (MDL) (Li et al., 2007). Then, spatial ICA was performed using Infomax algorithm (Hyvarinen and Oja, 2000):

$$\text{ICA step: } S = R \cdot W$$

where $S \in \mathfrak{R}^{nV, nC}$ is a source matrix, which contained spatial distributions of maximally independent sources and $W \in \mathfrak{R}^{nC, nC}$ is de-mixing matrix. By merging both former equations together we see that:

$$D \approx S \cdot W^{-1} \cdot dwM = S \cdot A$$

where $A \in \mathfrak{R}^{nC, nS}$ is mixing matrix, which held the information of how much does each source explain variability in each subject, i.e. subject’s loadings, with the interpretation of the higher subject’s loading, the more local gray matter in the corresponding source. The loadings were filtered using linear regression model to discard effects of age and gender and subsequently used to statistically test each source for relationship to DV. We used non-parametric statistical testing because the data did not meet Gaussian distribution and due to

unbalanced numbers of subjects in groups. Mann-Whitney test was used to detect sources which show difference in local GMV between DVG and nonDVG and Kruskal-Wallis test to assess the relationship between local GMV and DV frequency. The level of statistical significance was set to $p < 0.05$, Bonferoni corrected for multiple tests. The columns of source matrix were reshaped back to the original 3D representation, normalized to have unit standard deviation and thresholded with $|Z| > 2.5$ to depict brain regions with the strong DV effect.

3. Results

3.1. Voxel Based Morphometry

The VBM method did not find any voxels with significant effect of factor “group”.

3.2. Source Based Morphometry

After data preprocessing and forming the matrix D , the optimal number of PCA components was set to eight as estimated using MDL criterion. The matrix of principal components R was then subjected to ICA algorithm which resulted in eight independent spatial components described by matrices S (spatial sources) and A (subjects loadings). The row vectors of A , adjusted for age and gender, were tested for difference between DVG and nonDVG. One component showed significant effect (Mann-Whitney U test, $Z=2.81$) of less local gray matter volume in the DVG when compared to nonDVG. The spatial source comprised bilateral mesiotemporal cortices, bilateral insula, superior temporal sulci and subcortical regions (Table 2, Fig. 1).

Table 2. Regions with greater local gray matter volume in subjects without déjà-vu experience when compared to subjects with déjà-vu experience.

Resulting regions	MNI coordinates [mm]	Number of voxels	Z-score in maximum
L Putamen / Caudatum	-20, 10, -6	331	3.89
L Superior Temporal Sulcus	-52, -46, 8	217	3.80
L Parahippocampal Gyrus / Hippocampus / Fusiform Gyrus / Amygdala	-30 -34 -14	487	3.67
L / R Thalamus	0 , -16, 6	242	3.65
R Putamen / Caudatum	22, 10, -6	264	3.47
R Inferior Parietal Lobule / Superior Temporal Sulcus	50, -44, 20	69	3.28
R Parahippocampal Gyrus / Hippocampus / Amygdala	22, -6, -22	238	3.11
L Insula	-36, -4, -2	94	2.89
R Insula	38, 14, -6	104	2.88

L, left; R, right; MNI coordinates, coordinates in MNI stereotactic space (x,y,z); voxel size, 1.5 x 1.5 x 1.5 mm

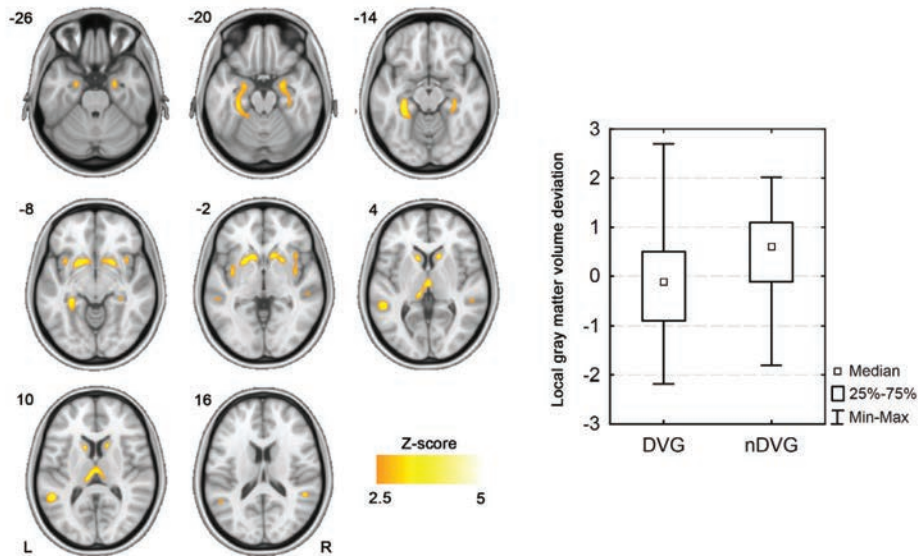


Figure 1. Regions with greater local gray matter volume in subjects without déjà-vu experience (nDVG) when compared to subjects with déjà-vu experience (DVG) as revealed by Source Based Morphometry method. The left panel shows the spatial distribution of the source thresholded with $|Z| > 2.5$. The right panel shows bar graph of subjects loadings (Mann-Whitney U test, $p < 0.05$, Bonferroni corrected for eight tests).

The loadings of significant component were then tested for the effect of DV frequency. For this analysis the groups “often” and “very often” were merged together due to small sample sizes (Table 1) yielding 4 final groups. The Kruskal-Wallis ANOVA test revealed significant relationship between DV frequency and local GMV at the respective brain regions ($H = 8.48$, $p < 0.05$, Fig. 2).

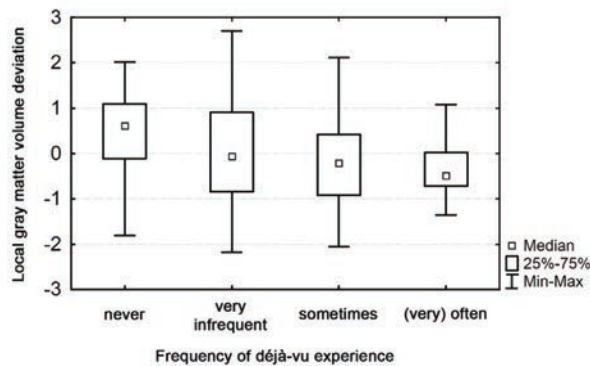


Figure 2. Statistically significant relationship between frequency of déjà-vu experience and local gray matter volume in brain regions depicted in Figure 1 (Kruskal-Wallis ANOVA, $H = 8.48$, $p < 0.05$).

4. Discussion

While VBM did not reveal any differences in local GMV between DVG and nDVG, SBM showed a vastly spatially distributed pattern of brain regions which shares a subtle effect of local GMV decrease in DVG when compared to nDVG and moreover, showed that the decrease is proportional to the frequency of DV experiences. This pattern is similar to the recently identified reduction of local GMV in patients with mesial temporal lobe epilepsy (Pail et al., 2010) which indicates that there might be common process underlying the generation of non-pathological DV and DV occurring as an aura in epilepsy patients.

The reason, why VBM lacked, might be an insufficient effect size in data resulting in false negative outcomes. Other reason could be the usage of parametric testing, a common practice in VBM studies, while the assumptions about normality of data might not be fulfilled.

5. Conclusion

Our study showed a pattern of mesiotemporal, subcortical and several cortical brain regions with reduction of local gray matter volume related to the increasing frequency of DV experiences and supports the hypothesis of neurophysiological origin of déjà-vu and its relationship to morphological and functional changes in the memory networks. Further, in accordance with the Kasperek et al. study (Kasperek et al., 2010) we concluded that Source Based Morphometry is more sensitive to subtle alterations in gray matter volume than Voxel Based Morphometry.

References

- Adachi N, Adachi T, Kimura M, Akanuma N, Takekawa Y, Kato M. 2003. Demographic and psychological features of déjà vu experiences in a nonclinical Japanese population. *Journal of Nervous And Mental Disease* 191: 242-247.
- Ashburner J. 2007. A fast diffeomorphic image registration algorithm. *Neuroimage* 38: 95-113.
- Ashburner J, Friston KJ. 2005. Unified segmentation. *Neuroimage* 26: 839-851.
- Brown AS. 2003. A review of the déjà vu experience. *Psychological Bulletin* 129: 394-413.
- Guedj E, Aubert S, McGonigal A, Mundler O, Bartolomei F. 2010. Déjà-vu in temporal lobe epilepsy: Metabolic pattern of cortical involvement in patients with normal brain MRI. *Neuropsychologia* 48: 2174-2181.
- Hyvarinen A, Oja E. 2000. Independent component analysis: algorithms and applications. *Neural Networks* 13: 411-430.
- Kasperek T, Marecek R, Schwarz D, Prikryl R, Vanicek J, Mikl M, Ceskova E. 2010. Source-Based Morphometry of Gray Matter Volume in Men With First-Episode Schizophrenia. *Human Brain Mapping* 31: 300-310.
- Kovacs N, Auer T, Balas I, Karadi K, Zambo K, Schwarcz A, Klivenyi P, Jokeit H, Horvath K, Nagy F, Janszky J. 2009. Neuroimaging and cognitive changes during déjà vu. *Epilepsy & Behavior* 14: 190-196.
- Li Y-O, Adali T, Calhoun VD. 2007. Estimating the number of independent components for functional magnetic resonance imaging data. *Human Brain Mapping* 28: 1251-1266.
- Mechelli A, Price CJ, Friston KJ, Ashburner J. 2005. Voxel-based morphometry of the human brain: Methods and applications. *Current Medical Imaging Reviews* 1: 105-113.

- Nichols T, Hayasaka S. 2003. Controlling the familywise error rate in functional neuroimaging: a comparative review. *Statistical Methods in Medical Research* 12: 419-446.
- Pail M, Brazdil M, Marecek R, Mikl M. 2010. An optimized voxel-based morphometric study of gray matter changes in patients with left-sided and right-sided mesial temporal lobe epilepsy and hippocampal sclerosis (MTLE/HS). *Epilepsia* 51: 511-518.
- Sno HN, Schalken HFA, Dejonghe F, Koeter MWJ. 1994. The Inventory For Deja-Vu Experiences Assessment – Development, Utility, Reliability, And Validity. *Journal of Nervous and Mental Disease* 182: 27-33.
- Vignal JP, Maillard L, McGonigal A, Chauvel P. 2007. The dreamy state: hallucinations of autobiographic memory evoked by temporal lobe stimulations and seizures. *Brain* 130: 88-99.
- Xu L, Groth KM, Pearlson G, Schretlen DJ, Calhoun VD. 2009. Source-Based Morphometry: The Use of Independent Component Analysis to Identify Gray Matter Differences With Application to Schizophrenia. *Human Brain Mapping* 30: 711-724.

Imaging genetics – a way of studying the link between genes and brain structure and function

Giovanni Montana¹

¹ *Biomedical Engineering Department, King's College London, GB;
e-mail: giovanni.montana@kcl.ac.uk*

Abstract

The aim of the talk is to introduce imaging genetics and its techniques and methods used in searching for associations between genes and brain structure or function. The imaging genetics enables to study how genes influence psychopathology of mental disorders and to investigate genes which are expressed in the brain. In the Alzheimer's disease research, for example, combining the genetics and brain imaging data has led to increased rates of predicting Alzheimer's disease.

Key words

Imaging genetics, association, genes, brain structure, brain function.

Image Data Analysis and Processing in Neuroscience

Students' Abstracts



Multiresolution analysis of brain images for schizophrenia recognition

Petr Dluhoš^{1,2}, Daniel Schwarz³, Tomáš Kašpárek^{1,2}

¹ *Behavioural and Social Neuroscience Group, CEITEC – Central European Institute of Technology, Masaryk University, Brno, Czech Republic*

² *Department of Psychiatry, University Hospital Brno and Masaryk University, Brno, Czech Republic*

³ *Institute of Biostatistics and Analyses, Masaryk University, Brno, Czech Republic*

Abstract

This paper deals with utilization of discrete wavelet transform (DWT) for feature extraction in medical image classification. It presents exhaustive analysis of influence of various parameters of DWT on the resulting accuracy of classification. The experiments are performed and validated on a dataset of 104 patients with first episode schizophrenia and healthy volunteers. The best combination of parameters achieves accuracy of 84% with balanced values of sensitivity and specificity.

Key words

Wavelet transform, feature extraction, classification, schizophrenia, MRI.

1. Introduction

Machine learning methods are increasingly utilized for automated classification and diagnosis in various areas of medicine. In schizophrenia, however, the straightforward approaches fail to achieve accuracy and robustness sufficient for clinical application (Nieuwenhuis et al., 2012). Perhaps due to heterogeneity of the disorder and its manifestations or due to a complex pattern of relatively discrete local brain changes that might be difficult to capture by classification algorithms. There is, therefore, continuing search for optimal set of feature encoding strategies and robust classification approaches that would render the image-based classification useful in the clinical setting.

A promising tool to deal with problems specific for medical image-based classification (high feature space dimensionality, redundancy of features and their complex spatial relations) is discrete wavelet transform (Misiti et al., 2007). This method enables extracting key features on multiple spatial scales by transferring the image into a new domain in which the frequency and space information is represented by functions of special form – wavelets. High potential of this approach has been demonstrated in several studies (Dluhoš et al., 2014; Hackmack et al., 2012; El-Dahshan et al., 2014), however, the exact influence of various parameters of DWT and following classification on final accuracy is unclear and has to be examined.

The aim of the presented study was to perform a systematic analysis of influence of parameters of wavelet transform on classification of patients with first episode of schizophrenia (FES) and healthy controls (HC) and to find a combination of parameters which creates a classifier with the highest accuracy.

2. Methods

52 first episode schizophrenia patients and 52 healthy controls were scanned by 1.5T MR device. The resulting T1-weighted images were spatially normalized and segmented into tissue types. DWT was applied to the grey matter and white matter tissue segments and to Jacobians of deformations used for spatial normalization. From all the DWT coefficients only those surpassing chosen threshold were retained and from those only several coefficients with the most discriminative power were selected. These coefficients were used as an input for a linear support vector machines (SVM) classifier. The classification accuracy was estimated by leave-one-out cross-validation.

The whole classification procedure from DWT transform onwards was performed multiple times with all combinations of following parameters: data modality, wavelet family, level of DWT decomposition, percentage of DWT coefficients retained, number of coefficients selected and SVM regularization parameter C. The computations were performed in software Matlab using Wavelet toolbox (<http://www.mathworks.com/products/wavelet/>) and Statistics toolbox (<http://www.mathworks.com/help/stats/support-vector-machines.html>) and realised in the CERIT-SC computing and storage facilities (<https://www.cerit.cz>).

3. Results

Analysis of classification accuracy of all combinations of the six examined parameters revealed complex nonlinear relations among them. The best combination of parameters achieved accuracy over 84% (with balanced values of sensitivity and specificity). These values were robustly estimated by 100 repetitions of stratified 52-fold cross-validation runs.

4. Conclusion

The achieved results (accuracy 84%) are comparable with the recent studies aimed at automated classification of patients with FES (accuracy 54% to 81%) (Mourao-Miranda et al., 2012; Zanetti et al., 2013; Kaspárek et al., 2011; Takayanagi et al., 2011) while being distinguished by robust estimates of sensitivity and specificity in combination with correctly performed cross-validation and relatively large dataset. These facts show that wavelet transform provides a useful tool for extracting important information from medical images.

Next step should be verification of the results and their transferability on an independent dataset and examination of other transforms similar to DWT potentially suitable for feature extraction in medical image classification.

References

- Dluhoš P, Schwarz D, Kašpárek T. 2014. Wavelet Features for Recognition of First Episode of Schizophrenia from MRI Brain Images. *Radioengineering* 23(1): 275-281.
- El-Dahshan ESA, Mohsen HM, Revett K, Salem ABM. 2014. Computer-aided diagnosis of human brain tumor through MRI: A survey and a new algorithm. *Expert Systems with Applications* 41 (11): 5526-5545.
- Hackmack K, Paul F, Weygandt M, Allefeld C, Haynes JD. 2012. Multi-Scale Classification of Disease Using Structural MRI and Wavelet Transform. *NeuroImage* 62(1): 48-58.

- Kasperek T, Thomaz CE, Sato JR, Schwarz D, Janousova E, Marecek R, Prikryl R, Vanicek J, Fujita A, Ceskova E. 2011. Maximum-uncertainty linear discrimination analysis of first-episode schizophrenia subjects. *Psychiatry research* 191(3): 174-81.
- Misiti M, Misiti Y, Oppenheim G, Poggi JM (eds.) *Wavelets and their Applications*. Wiley-ISTE, 2007. 330 p. ISBN 978-1-905209-31-6.
- Mourao-Miranda J, Reinders AATS, Rocha-Rego V, Lappin J, Rondina J, Morgan C, Morgan KD, Fearon P, Jones PB, Doody GA, Murray RM, Kapur S, Dazzan P. 2012. Individualized prediction of illness course at the first psychotic episode: a support vector machine MRI study. *Psychological Medicine* 42(5): 1037-47.
- Nieuwenhuis M, van Haren NEM, Hulshoff Pol HE, Cahn W, Kahn RS, Schnack HG. 2012. Classification of schizophrenia patients and healthy controls from structural MRI scans in two large independent samples. *NeuroImage* 61(3): 606-12.
- Takayanagi Y, Takahashi T, Orikabe L, Mozue Y, Kawasaki Y, Nakamura K, Sato Y, Itokawa M, Yamasue H, Kasai K, Kurachi M, Okazaki Y, Suzuki M. 2011. Classification of first-episode schizophrenia patients and healthy subjects by automated MRI measures of regional brain volume and cortical thickness. *PLoS One* 6(6): e21047.
- Zanetti MV, Schaufelberger MS, Doshi J, Ou Y, Ferreira LK, Menezes PR, Scazufca M, Davatzikos C, Busatto GF. 2013. Neuroanatomical Pattern Classification in a Population-Based Sample of First-Episode Schizophrenia. *Progress in Neuro-Psychopharmacology and Biological Psychiatry* 43: 116-25.

Study of spinal cord in multiple sclerosis by MRI

Marek Dostál¹, Miloš Keřkovský²

¹ *Faculty of Medicine, Masaryk University, Brno
e-mail: 424327@mail.muni.cz*

² *Radiological Clinic, University Hospital Brno
e-mail: mkerkovsky@fnbrno.cz*

Abstract

The use of magnetic resonance imaging (MRI) of brain for diagnosis of neurological diseases like schizophrenia or multiple sclerosis (MS) is well known. However, neurological diseases affect the whole central nervous system (CNS). Therefore, it is logical to observe not only brain but also spinal cord. We used algorithms which were based on FSL software and automatically segmented white and grey matter of cervical spinal cord in T2-weighted images and separated spinal cord in diffusion-weighted images (DWI). These segmentations were only partially successful. Thus the algorithms should be improved; however, we confirmed that the approach is correct. We had data from only 2 volunteers at our disposal, which was enough for obtaining preliminary results.

Key words

Segmentation, Magnetic resonance imaging (MRI), Multiple sclerosis (MS), Spinal cord.

1. Introduction

Multiple sclerosis (MS) is a neurological disease which affects brain and spinal cord tissue. The clinical course of MS is very variable and the cause of it is not exactly known. In general women suffer from MS more often than men just as younger people (Birnbaum, 2009). Although we can sort MS into several categories, they are not stringent and often overlap. McDonald's criteria are commonly used for diagnostic of MS (Perkin and Wolinsky, 2006). They involve criteria for MS from the findings of T1 and T2-weighted magnetic resonance imaging (MRI) scans of the brain. However, we are interested in MRI of the spinal cord which represents not only a great technical challenge but also quite large unexplored area. The goal of this article is to show the first steps of segmentation of human spinal cord MR images.

2. Methods

The MR imaging protocol comprised conventional T1, T2 and STIR (shot-tau inversion recovery) images in sagittal plane and axial T2-weighted gradient-echo sequence, which was used for segmentations. For the DTI sequence, we used a single-shot echo planar technique with 4 mm slice thickness in the axial plane, applying 15 directions of diffusion sensitizing gradient with 900 s/mm^2 as the b value setting. The geometry settings for the DTI acquisition were exactly the same as for the T2-weighted gradient-echo scans.

We have used FSL (the FMRIB software library) for reconstructions and analysis of MRI imaging data. FSL is a comprehensive library of analysis tools like brain extraction tool

(BET) (Smith, 2002), linear and non-linear registration tool (FLIRT and FNIRT) (Jenkinson and Smith, 2001), diffusion toolbox (FDT) (Behrens et al., 2003) and so on (Jenkinson et al., 2012). Although DICOM format seems to be a native format of MRI data, the FSL does not support it. DICOM data is converted by dmc2nii in Mricron software to NIFTI format which is more suitable for further analysis.

The study is now in the beginning; therefore, we have available data from 2 volunteers only. Nonetheless, we are planning to examine around 40 patients with MS and the same number of volunteers who will be matched to pairs. Changes in patient s' DTI spinal cord imaging will be observed for 2 years using automatic segmentation algorithms for our measurements.

3. Results

The first step is use of an automated method for segmentation of the white and grey matter in cervical part of spinal cord in T2-weighted images (T2-w). We are quite successful in the middle part (Figure 1), but not in the top and bottom part of cervical spinal cord (Figure 2 and 3)



Figure 1. Successful segmentation of grey matter in the middle part of cervical spinal cord (T2-w)

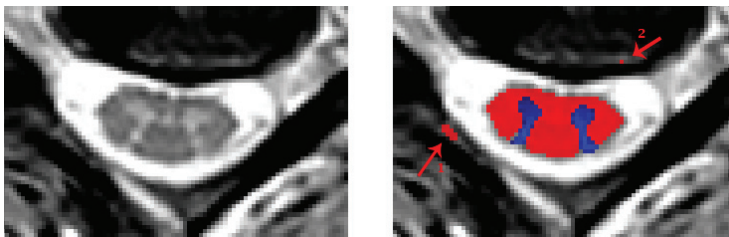


Figure 2. Segmentation of grey and white matter in the middle part of cervical spinal cord with 2 small errors (T2-w)



Figure 3. Segmentation of grey and white matter in the bottom part of cervical spinal cord with identification error in grey matter (T2-w)

The first attempt to segment the spinal cord in diffusion-weighted images (DWI) was done in the B0 images (Figure 4.) and it seems to be usable in further analysis.

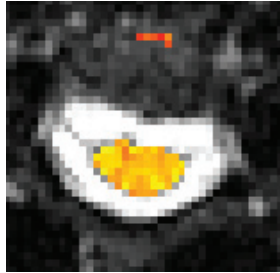


Figure 4. Segmentation of spinal cord in the middle part of cervical spinal cord (B0)

4. Conclusion

On the basis of the preliminary results of our study it is possible to automatically separate spinal cord from the surrounding structures in T2-weighted and B0 images; moreover, it seems to be technically feasible to segment white and grey matter in T2-weighted images. However, this segmentation does not work perfectly in the full length of cervical cord yet.

References

- Behrens TEJ, Woolrich MW, Jenkinson M, Johansen-Berg H, Nunes RG, Clare S, Matthews PM, Brady JM, Smith SM. 2003. Characterization and propagation of uncertainty in diffusion-weighted MR imaging. *Magnetic Resonance in Medicine* 50: 1077-1088.
- Birnbaum G. Multiple sclerosis: clinician's guide to diagnosis and treatment. Cary, NC, USA: Oxford University Press, USA, 2009. 157 p. ISBN 978-0-19-537316-5.
- Jenkinson M, Beckmann CF, Behrens TEJ, Woolrich MW, Smith SM. 2012. FSL. *NeuroImage* 62: 782-790.
- Jenkinson M, Smith SM. 2001. A global optimisation method for robust affine registration of brain images. *Medical Image Analysis* 5: 143-156.
- Smith SM. 2002. Fast robust automated brain extraction. *Human Brain Mapping* 17: 143-155.
- Perkin GD, Wolinsky JS. Fast facts : multiple sclerosis. Abingdon, UK: Health Press Limited, 2006. 98 p. ISBN 1-903734-70-3.

Pattern recognition methods for image data analysis

Tereza Dufková¹, Eva Janoušová¹, Tomáš Kašpárek^{2,3}

¹ *Institute of Biostatistics and Analyses, Masaryk University, Brno;*

² *Behavioural and Social Neuroscience Group, CEITEC - Central European Institute of Technology, Masaryk University, Brno, Czech Republic*

³ *Department of Psychiatry, University Hospital Brno and Masaryk University, Brno, Czech Republic*

e-mail: dufkova@iba.muni.cz

Abstract

The study is focussed on the pattern recognition, mainly on the use of the pattern recognition of the magnetic resonance imaging in diagnosis of schizophrenia. The data are preprocessed by the voxel-based morphometry and the inputs of the algorithms are smoothed gray matter images. There were two methods applied to the classification, linear discriminant analysis and support vector machine, whose accuracy is compared by the McNemar test. Particular steps of the pattern recognition are applied on two datasets. At first it is used on the simulated data of geometric shapes and subsequently analyzed on the real image dataset of the first episode schizophrenic patients and healthy controls from the University Hospital Brno.

Key words

Pattern recognition, MRI, schizophrenia, linear discriminant analysis, support vector machine.

1. Introduction

Schizophrenia is one of the gravest illnesses limiting quality of life of the patients and their families. Particular causes of this disease have not been described yet. Schizophrenia is diagnosed by the clinical interview with a psychiatrist. There is no objective method for proving the presence of this disease (Češková, 2005). Latest studies show small changes in morphology of schizophrenic's brain tissue. However, these changes are not noticeable by unaided eye. If we discovered sufficient image analysis methods for proving schizophrenia, patients could be treated by earlier and more precise therapy hence they could earlier achieve the remission. The aim of the study is to compare two classification methods usable in diagnosing schizophrenia.

2. Datasets

There were two datasets analysed in the study. The first one was a dataset of simulated geometric shapes containing 20 images of triangles and circles (each about 50 184 pixels). The second dataset contained 104 smoothed MRI brain images (each about 748 931 voxels). Fifty-two subjects were patients with schizophrenia and other 52 subjects were healthy controls.

3. Methods

The pattern recognition process consists of three basic steps: data pre-processing, data reduction, and classification. The simulated geometric shapes were neither pre-processed nor reduced. MRI brain data were reduced by using selection of voxels which values were statistically significantly different between patients and controls (based on t-test with FDR correction for multiple testing). Both datasets were classified by linear discriminant analysis (LDA) and support vector machine (SVM) from the Statistics toolbox in MATLAB software. Objects were divided into testing and training subsets by validation technique leave-one-out. The classifiers were subsequently compared by the McNemar test (Kuncheva, 2004).

4. Results

In the classification of geometric shapes by LDA all of the images were classified correctly. Using the SVM in the same dataset one of the images was classified incorrectly. The results are shown in Table 1. The classifiers were compared by McNemar test with p-value 1, hence there is no statistically significant difference.

Table 1. Results of the geometric shapes classification

Classification method	Accuracy (%)	Sensitivity (%)	Specificity (%)
LDA	100	100	100
SVM	95	100	90

In the classification of MRI data, better results were achieved by LDA than SVM for age-adjusted and also not age-adjusted patients. As a result of comparing the results (shown in Table 2) by McNemar test p-value 0.814 for not age-adjusted data and 0.453 for age-adjusted data were achieved. There is no statistically significant difference in both cases.

Table 2. The results of the MRI data classification

Classification method		Accuracy (%)	Sensitivity (%)	Specificity (%)
LDA	age not adjusted data	65.4	59.6	71.2
SVM	age not adjusted data	60.6	55.8	65.4
LDA	age adjusted data	72.1	69.2	75.0
SVM	age adjusted data	62.5	61.5	63.5

5. Conclusion

Although better results were achieved in the classification by LDA, there is no statistically significant difference between linear discriminant analysis and support vector machine on the given datasets. The best accuracy 72.1% is comparable with results of international studies

(Davatzikos et al., 2005; Karageorgiou et al., 2011; Zanetti et al., 2013); however, it is necessary to try other methods for clinical use.

References

- Češková E. Schizofrenie a její léčba: průvodce ošetřujícího lékaře. Farmakoterapie pro praxi; sv. 2. Praha: Maxdorf, 2005. 101 p. ISBN 8073450569.
- Davatzikos Ch, Shen D, Gur RC, Wu X, Liu D, Fan Y, Hughett P, Turetsky B, Gur RE. 2005. Whole-brain morphometric study of schizophrenia revealing a spatially complex set of focal abnormalities. *Archives of general psychiatry* [online] 62: 1218–1227.
- Karageorgiou E, Schulz Ch, Gollub RL, Andreasen NC, Ho B, Lauriello J, Calhoun VD, Bockholt HJ, Sponheim SR, Georgopoulos AP. 2011. Neuropsychological Testing and Structural Magnetic Resonance Imaging as Diagnostic Biomarkers Early in the Course of Schizophrenia and Related Psychoses. *Neuroinformatics* [online] 1.12: 321–333.
- Kuncheva L. I. Combining Pattern Classifiers: Methods and Algorithms. Hoboken (New Jersey): John Wiley & Sons Inc., 2004. 376 p. ISBN 0-471-21078-1
- Zanetti MV, Schaufelberger MS, Doshi J, Ou Y, Ferreira LK, Menezes PR, Sczufca M, Davatzikos Ch, Busatto GF. 2013. Neuroanatomical pattern classification in a population-based sample of first-episode schizophrenia. *Progress in neuro-psychopharmacology & biological psychiatry* [online] 43: 116–125.

Mask_explorer – tool for group fMRI data validation and its application on study of Levodopa effect in patients with Parkinson’s disease

Martin Gajdoš¹, Michal Mikl¹, Radek Mareček¹

¹ *Central European Institute of Technology - CEITEC, Masaryk University, Brno; e-mail: martin.gajdos@ceitec.muni.cz*

Abstract

In this work the software tool mask_explorer is described and its practical use is demonstrated. It is designed for group fMRI analysis. The aim of the mask_explorer is to enable exploration of fMRI dataset and to prevent unwanted data loss, caused by automatic discarding of voxels with missing information even in one or few subjects. The user interface and application of the mask_explorer are shown and described. Subsequently we demonstrate usefulness of mask_explorer on two examples in study of Levodopa effect in patients with Parkinson’s disease.

Key words

fMRI, group analysis, dataset explorer, validity, statistical parametric mapping

1. Introduction

Functional magnetic resonance imaging (fMRI) is a commonly used method in neuroscience research. The group fMRI analysis enables testing hypotheses related to the target population or even on the whole population (Huettel et al., 2009). The tool mask_explorer is created for group dataset exploration. Because every brain has different shape and every subject contains intersubject differences in the scanned region of interest, some voxels intended for group fMRI analysis can miss information from some subjects involved in analysis. These voxels do not enter the group fMRI analysis and are automatically discarded. This could remain hidden from attention of the user. Currently, there are several reliable software tools available for fMRI data analysis, as e.g. SPM (Guillaume, 2014), FSL, and BrainVoyager (Goebel, 2014). However, these tools do not offer dataset exploration based on superposition of data masks of individual subjects with respect to region of users’ interest (region intended to infer group results). This is the reason for development of the tool mask_explorer. To show practical benefits of this designed tool, we demonstrate the use of mask_explorer in analysis of BOLD data in study of Levodopa effects in patients with Parkinson’s disease (PD).

2. Methods

2.1. Designed tool

Mask_explorer provides user friendly graphical interface. The tool runs in the MATLAB environment and is compatible with SPM8 and SPM12b toolbox. The screenshot of graphical interface is shown in Figure 1. The left triad of views is used to display a variant of group mask where intensities represent number of subjects containing valid data at the

specific coordinate. This mask is estimated from loaded masks, cons or other standard 1-st level statistic SPM8 files. As individual mask we consider binary image with ones on positions containing information from measurement and zeros elsewhere. The mask_explorer counts and saves group binary mask (created as a conjunction of individual binary masks) and subject count file (created as a count of individual binary masks). The right triad of views is used to display one overlay file, especially con file, spmT file, beta file or raw-data file (e.g. echoplanar image). Overlay and background images are displayed in normalized MNI space. User can define coordinates of interest and mask_explorer displays unsuitable subjects for analysis on this coordinates. More details about mask_explorer are in this contribution (Gajdoš et al., 2012). In this work we introduce new version of mask_explorer with extended functions, e.g., batch mode for creating masks from BOLD data of whole dataset, import and export of lists of coordinates and suitable subjects.

2.2. Data used

In used Levodopa study we measured in 16 PD patients (disease duration 29 ± 6 months, age 63.9 ± 6.9 years) on 1.5T MR scanner two sessions of task free data, each 150 scans. Repetition time was 3 s. Every patient was scanned in the OFF and ON medication condition. We performed standard preprocessing steps (unwarp, spatial normalization, spatial smoothing) in SPM8. On this data we performed ICA analysis to identify spatial components of resting state networks, e.g. default mode network (DMN). Details are presented in Elfmarkova et al. (2014).

4. Results

4.1. Identification of failure in spatial normalization

We used mask_explorer to create masks of preprocessed images. Then we identified failure in spatial normalization in data of several subjects as shown in Figure 1. Therefore we repeated spatial normalization step. This time we were successful with normalization of BOLD images to normalized MNI EPI template (offered in SPM8) instead of normalization to anatomical images of subjects.

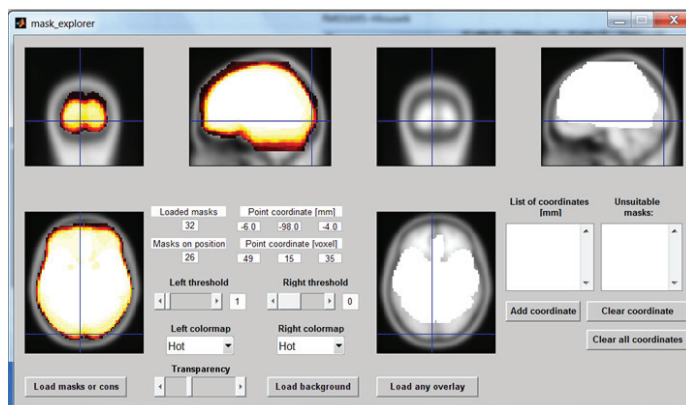


Figure 1. Interface of mask_explorer. On the left triad is shown revealed failure of spatial normalization, on the right triad is mask of one of subjects affected by this failure. Data in normalized MNI space are out of brain template.

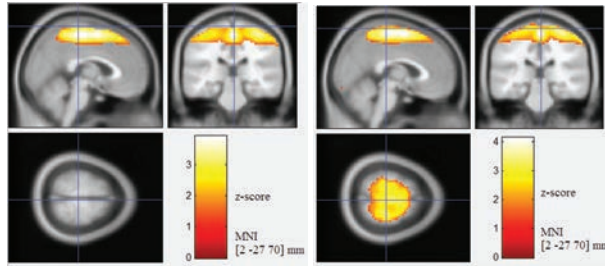


Figure 2. ICA spatial component of DMN. Left part shows inactivation (16 PD subjects); in the right part was removed outlying subject (15 PD subjects). The same position is active.

4.2. Identification of spatial abnormalities

With fixed preprocessing step we again created masks and identified one outlying subject with abnormally scanned field of view. This subject was removed from analysis. Comparison of affected ICA component of default mode network is in Figure 2, greatest difference is on axial slice. After removing outlying subject we improved spatial information about parietal activation of the ICA component. False displayed inactivity was caused due to one outlier, not due to inactive state of part of parietal cortex.

5. Conclusion

We have shown the practical use of `mask_explorer` as the tool for group fMRI dataset exploration. We have described basic principles of this tool and mentioned new utilities implemented in actualized version of `mask_explorer`. We have demonstrated identification of problems in fMRI analysis using this tool. Its purpose is to enable searching for inconsistent data. The loss of useful information can occur in some cases, when the dataset is not attentively explored, e.g. false inactivation could be caused due to one outlier. To prevent these problems and false decisions about hypotheses we recommend using `mask_explorer`. The tool runs in the MATLAB environment. It is freeware under GNU license, accessible on web site of group fMRI Brno.

References

- Elfmarková N, Gajdoš M, Mráčková M, Mikl M, Rektorová I. Effect of L-Dopa on Functional Magnetic Resonance Imaging Connectivity in Parkinson's Disease. 20th Annual Meeting of the Organization for Human Brain Mapping, Hamburg, Germany, 8-12 June 2014.
- Gajdoš M, Mikl M, Mareček, R. Dataset exploration tool for fMRI group analysis. 19th International Conference on Systems, Signals and Image Processing, IWSSIP 2012, Vienna, Austria, 11-13 April 2012, p. 492-495. ISBN: 978-320002328-4
- Goebel R. 2014. Brain Innovation [online]. [cit. 2014-07-12]. Available at WWW: <http://www.brainvoyager.com/>
- Guillaume F, 2014. SPM - Statistical Parametric Mapping [online]. [cit. 2014-06-26]. Available at WWW: <http://www.fil.ion.ucl.ac.uk/spm/>
- Huettel S. A., Song A. W., and McCarthy G. Functional Magnetic Resonance Imaging, Second Edition. Sunderland: Sinauer Associates, 2009. ISBN 978-0-87893-286-3

SigHunt: The new way of thinking about horizontal gene transfer

Kamil S. Jaroň¹, Jiří C. Moravec², Natália Matínková^{1,3}

¹ *Institute of Biostatistics and Analyses, Masaryk University, Brno, Czech Republic;*
e-mail: 376090@mail.muni.cz;

² *Institute of Fundamental Sciences, Massey University, Palmerston North, New Zealand;*

³ *Institute of Vertebrate Biology, Academy of Sciences of the Czech Republic, Brno, Czech Republic;*

Abstract

The importance of horizontal gene transfer (HT) for prokaryotes has been discovered in the past few decades, but only recent studies reveal the impact of this evolutionary mechanism to eukaryotes. However, the methods for detection of HT candidates based on structural consistency of prokaryotic genome are failing in detection of HT candidates in eukaryotes because of genome size and its heterogeneity. We present a new method optimized for eukaryotic genomes.

Key words

Horizontal transfer, genomic islands, surrogate method, high-throughput, genomics

1. Introduction

For a long time it has been assumed that the genetic information is inherited in the parent-offspring direction. The discovery of exchange of bacterial plasmids (Lederberg and Tatum, 1946) showed that an exchange of genes between more distant species is possible. Similar breakthrough lead to HT in the eukaryotic domain and between domains (Schmidt and Hensel, 2004). This event is called horizontal or lateral gene transfer (HT). Most of the mechanisms of HT are not yet understood. Products of HT, genomic islands (GIs), encode genes associated with pathogenicity or specific adaptations to extreme conditions (Schmidt and Hensel, 2004, Schönknecht et al., 2013).

The most direct way of GI detection is phylogenetic reconstruction of a particular gene with its orthologs and comparing them to a neutral phylogeny. This approach is effective on small scale, but it could be very problematic in case of whole genome examination. The extent of the process can be reduced by finding GI candidates using surrogate methods, which are based on observation of structural divergence between the host genome sequence and sequences of GIs (Karlin and Burge, 1995). The structure is represented by a genomic signature, a vector of k-mer frequencies. The surrogate methods of GI detections are well studied in prokaryotes, but HT detection in eukaryotic genomes provides a range of research opportunities.

2. Algorithm

SigHunt computes frequencies of tetramers (genomic signatures) of the input genomic sequence using a sliding window approach. Then, for every window a Discrete Interval Accumulative Score (DIAS) is calculated using a following process: 1) compute tetramer

density and its credibility intervals for $\alpha \in (0.05, 0.025, 0.01)$ for the surrounding region of the examined window; 2) compare the window frequency with credibility intervals and add 0, 1, 2 or 3 to DIAS respectively (Jaron et al., 2014).

Windows with high DIAS are putative genomic islands and should be further examined using the phylogenetic approach (Figure 1).

3. Results

SigHunt was tested on 500 sequences with GIs simulated by introducing random sequences into a tested chromosomal sequence originating from various species (*Aspergillus*, *Encephalitozoon*, *Saccharomyces*, *Cyanidioschyzon*, *Drosophila*, *Cryptosporidium*, *Plasmodium*, *Thalassiosira*, *Buchnera*, *Escherichia*). Sensitivity and specificity of detection of the introduced sequences was measured using area under receiver operating characteristic curve (AUC). SigHunt showed AUC values in range from 0.7 to 0.86 and average 0.77. Genomic islands were assigned only where they had been artificially introduced, the sequence could still contain its natural GIs, what lowers the AUC value.

Additional testing dataset contained genomic sequences of five organisms with previously described GIs. SigHunt was compared with other surrogate methods where it performed similarly or better than Indegenius and Alien_Hunter (Table 1).

4. Discussion

SigHunt is capable to find most of the artificially introduced GIs and also real GIs. SigHunt enables effective detection of GIs, but it is limited mainly by an assumption that there are differences in genomic signatures between organisms (Karlin and Burge, 1995). Further investigation of this property could help to generalize SigHunt and possibly reveal types of GIs, which are undetectable by phylogenetic methods due to impossibility of searching for orthologs.

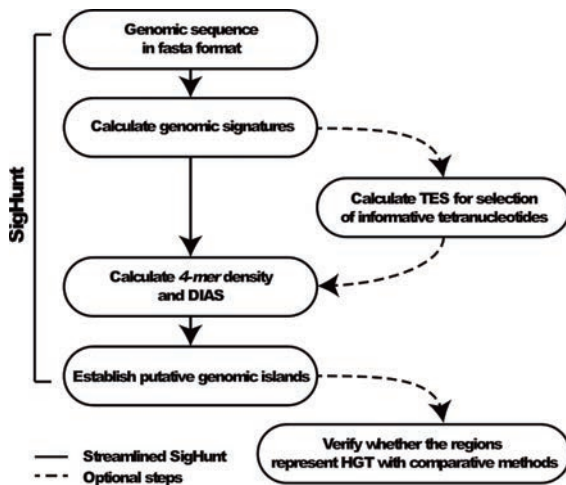


Figure 1. Flowchart of the SigHunt method (Jaron et al., 2014).

Table 1. Number of found known GIs using different surrogate methods (Jaron et al., 2014; edited).

Sp	islands	SigHunt	Indegenius	Alien Hunter
Aspergillus	189	150	189	54
Pyrenophora	17	6	11	0
Saccharomyces	10	5	2	5
Galdieria	79	48	15	33
Cryptosporidium	30	9	12	11

5. References

- Jaron KS, Moravec JC, Martínková N. 2014. SigHunt: horizontal gene transfer finder optimized for eukaryotic genomes. *Bioinformatics*, 30.8: 1081-1086.
- Karlin S, Burge C. 1995. Dinucleotide relative abundance extremes: a genomic signature. *Trends in genetics*, 11.7: 283-290.
- Lederberg J, Tatum EL. 1946. Gene recombination in *Escherichia coli*. *Nature*, 158.4016: 558-558.
- Schmidt H, Hensel M. 2004. Pathogenicity islands in bacterial pathogenesis. *Clinical microbiology reviews*, 17.1: 14-56.
- Schönknecht G, Chen WH, Ternes CM, Barbier GG, Shrestha RP, Stanke M, Weber AP. 2013. Gene transfer from bacteria and archaea facilitated evolution of an extremophilic eukaryote. *Science*, 339.6124: 1207-1210.

**Proceedings of the 10th Summer School on Computational Biology
Image Data Analysis and Processing in Neuroscience**

Editors: Eva Janoušová, Daniel Schwarz
Cover: Radim Šustr

Published by Masaryk University
www.muni.cz

Printed by Tiskárna KNOPP, s.r.o., Nádražní 219, 549 01 Nové Město nad Metují
1st edition, 2014
100 copies

ISBN 978-80-210-7011-0